

Massive star formation in Wolf-Rayet galaxies

V. Star-formation rates, masses and the importance of galaxy interactions

Á. R. López-Sánchez^{1,2}

¹ CSIRO Astronomy and Space Science / Australia Telescope National Facility, PO Box 76, Epping, NSW 1710, Australia
e-mail: Angel.Lopez-Sanchez@csiro.au

² Instituto de Astrofísica de Canarias, C/ Vía Láctea S/N, 38200 La Laguna, Tenerife, Spain

Received 20 February 2010 / Accepted 3 May 2010

ABSTRACT

Aims. We performed a comprehensive analysis of a sample of 20 starburst galaxies that show a substantial population of very young massive stars, most of them classified as Wolf-Rayet galaxies.

Methods. In this paper, the last in the series, we analyze the global properties of our galaxy sample using multiwavelength data extracted from our own observations ($H\alpha$ fluxes, B and H -band magnitudes) and from the literature, which include X-ray, FUV, FIR, and radio (both HI spectral line and 1.4 GHz radio-continuum) measurements.

Results. The agreement between our $H\alpha$ -based star-formation rates (SFR) and those provided by indicators at other wavelengths is remarkable, but we consider that the new $H\alpha$ -based calibration provided by Calzetti et al. (2007, ApJ, 666, 870) should be preferred to older calibrations. The FUV-based SFR provides a powerful tool for analyzing the star-formation activity on both global and local scales independently to the $H\alpha$ emission. We provide empirical relationships between the ionized gas mass, neutral gas mass, dust mass, stellar mass, and dynamical mass with the B -luminosity. Although all mass estimations increase with increasing luminosity, we find important deviations to the general trend in some objects, which seem to be the consequence of their particular evolutionary histories. The analysis of the mass-to-light ratios give similar results. We investigate the mass-metallicity relations and conclude that both the nature and the star-formation history are needed to understand the relationships between both properties. The majority of the galaxies follow a Schmidt-Kennicutt scaling law of star-formation that agrees with that reported in individual star-forming regions within M 51 but not with that found in normal spiral galaxies. Dwarf galaxies seem to be forming stars more efficiently than the outskirts of spiral galaxies. We find a relation between the reddening coefficient and the warm dust mass indicating that the extinction is mainly internal to the galaxies. The comparison with the closed-box model also indicates that the environment has strongly affected their evolution.

Conclusions. Considering all multiwavelength data, we found that 17 up to 20 galaxies are clearly interacting or merging with low-luminosity dwarf objects or HI clouds. The remaining three galaxies (Mkn 5, SBS 1054+364, and SBS 1415+437) show considerable divergences of some properties when comparing with similar objects. Many of the interacting/merging features are only detected when deep optical spectroscopy and a detailed multiwavelength analysis, including HI observations, are obtained. We conclude that interactions do play a fundamental role in the triggering mechanism of the strong star-formation activity observed in dwarf starburst galaxies.

Key words. galaxies: starburst – galaxies: interactions – galaxies: dwarf – galaxies: abundances – stars: Wolf-Rayet – galaxies: kinematics and dynamics

1. Introduction

Since the discovery of the starburst galaxies (Sargent & Searle 1970), many studies have tried to understand the processes that trigger the strong star-formation activity in these objects. The hypothesis that the gravitational interaction (not necessarily merging) of galaxies enhances star-formation or leads to starburst activity was made soon after the recognition of the starburst phenomenon. Larson & Tinsley (1978) did a study of normal and peculiar (Arp 1966) samples of galaxies and demonstrated that recent ($\leq 10^8$ yr) star-formation is more likely to occur in interacting than in noninteracting galaxies. Since then, numerous studies of individual galaxies have revealed the fossil remnants of interaction/merger activity, increasing the evidence that interactions and mergers trigger star-formation phenomena in spiral galaxies (Koribalski 1996; Kennicutt 1998; Nikolic et al. 2004). Infrared observations confirmed the very intense starbursts in

major disk-disk mergers (e.g., Joseph & Wright 1985; Solomon & Sage 1988; Sanders & Mirabel 1996; Genzel et al. 1998; Arribas et al. 2004). Actually, almost 100% of galaxies with far-infrared (FIR) luminosities of about $10^{12} L_{\odot}$ are in interacting/merging systems (Sanders 1997). Furthermore, analysis of large-galaxy surveys (e.g., CfA2: Barton et al. 2000; 2dF: Lambas et al. 2003; SDSS: Nikolic et al. 2004) has provided new evidence of interaction-induced starburst activity.

According to hierarchical clustering models of galaxy formation, larger galactic structures build up and grow through the accretion of dwarf galaxies (White & Frenk 1991; Kauffman & White 1993; Springer et al. 2005). Observations of local and distant luminous blue galaxies (LBG) and Lyman break galaxies seem to confirm that galaxy interactions are more common at high redshifts (e.g., Guzman et al. 1997; Hopkins et al. 2002; Erb et al. 2003; Werk et al. 2004; Colina et al. 2005; Overzier et al. 2009; Cardamone et al. 2009), but many details are still

unclear (i.e., Basu-Zych et al. 2009). Indeed, detailed studies of local interacting/merging galaxies provide vital clues to galaxy formation and evolution, as they constrain the properties of the hierarchical formation models.

Recent observations also suggest that interactions and mergers between dwarf galaxies also trigger the star-formation activity and play a fundamental role in the evolution of dwarf galaxies (i.e., Méndez & Esteban 2000; Östlin et al. 2001, 2004; Bergvall & Östlin 2002; Johnson et al. 2004; Bravo-Alfaro et al. 2004, 2006; Cumming et al. 2008; García-Lorenzo et al. 2008; López-Sánchez & Esteban 2008, 2009; James et al. 2010). Many of these studies have been done on blue compact dwarf galaxies (BCDGs), which are low-luminosity, low-metallicity ($\sim 10\%$ solar) galaxies showing compact and irregular morphologies and undergoing an intense and short-lived episode of star-formation (i.e., Izotov & Thuan 1999; Cairós et al. 2001a,b; Papaderos et al. 2006), on top of an old underlying population with ages of several Gyrs (Noeske et al. 2003, 2005; Amorín et al. 2007, 2009). Recent numerical simulations (Bekki 2008) satisfactorily explain the physical properties of BCDGs as a consequence of the merging of two dwarf galaxies with a higher fraction of gas and extended gas disks.

Actually, much of our knowledge of interacting galaxies has been provided by HI observations. Neutral hydrogen gas is the best tracer of galaxy-galaxy interactions because the HI distribution is usually several times larger than the optical extent, hence more easily disrupted by external forces (tidal interactions, gas infall, ram pressure stripping) than the stellar disk (Broeils & van Woerden 1994; Salpeter & Hoffman 1996). The distribution and kinematics of atomic gas within galaxies is usually more or less regular, but in many cases they revealed complex entities between galaxies such as tails, ripples, bridges, arcs, or independent HI clumps that, in many cases, show little disturbance in their corresponding optical images (e.g., Schneider et al. 1989; Yun et al. 1994; Hibbard & van Gorkom 1996; Verdes-Montenegro et al. 2001, 2002, 2005; Putman et al. 2003; Koribalski et al. 2003, 2004, 2005; Temporin et al. 2003, 2005; Emonts et al. 2006; Ekta et al. 2008; Koribalski & López-Sánchez 2009; English et al. 2010; see also *The HI Rogues Gallery*, Hibbard et al. 2001). Several interferometric HI surveys, such as *The HI Nearby Galaxy Survey* (THINGS, Walter et al. 2008); the *Local Volume HI Survey* (LVHIS, Koribalski 2008) or the *Faint Irregular Galaxies GMRT Survey* (FIGGS, Begum et al. 2008), are providing accurate HI and dynamical masses in hundreds of nearby galaxies, many of them dwarf objects, as they account for $\sim 85\%$ of the known galaxies in the Local Volume (Karachentsev et al. 2004).

To understand interaction processes in dwarf galaxies we first have to know how stars and gas interact in low-mass environments. Indeed, feedback from massive stars is the dominant process that affects the interstellar medium (ISM) of these galaxies. Violent star-formation phenomena may disrupt the galaxy's gas and even expel it to the intergalactic medium, as some theoretical models predict (Mac Low & Ferrara 1999). But alternative models (e.g., Silich & Tenorio-Tagle 1998) and the available observations (Bomans 2005) suggest that dwarf galaxies keep their processed material. Furthermore, the links between the observational characteristics (fluxes, colors, morphologies, or sizes) and the underlying physical properties of the galaxies (stellar, dust, gas, baryonic, and dark matter content, chemical abundances, star-formation rate, and star-formation history) are still not well known.

For example, there are still many caveats in the understanding of the interplay between the star-formation rate (SFR) and the

properties of the ISM. A very important step was taken with the Schmidt-Kennicutt power-law relation (Schmidt 1959, 1963; Kennicutt 1998) that correlates the average SFR per unit area and the mean surface density of the cold gas (atomic plus molecular). But tracers of star-formation, including optical colors and $H\alpha$ flux (e.g., Larson & Tinsley 1978; Kennicutt 1998; Calzetti et al. 2007), FIR flux (Kennicutt 1998; Heckman 1999), radio-continuum flux (Condon 1992), and far-ultraviolet (FUV) flux (Kennicutt 1998; Salim et al. 2007), often yield to very different values of the SFR. Although the density of atomic gas is known in some cases, not many direct measurements of the molecular gas are available, and are especially rare in dwarf galaxies (i.e., Taylor et al. 1998; Barone et al. 2000; Braine et al. 2000, 2001, 2004).

On the other hand, the physics underlying the relationship between stellar mass (or luminosity) and metallicity is still far from clear, despite the important observational (e.g., Tremonti et al. 2004; van Zee & Haynes 2006; Kewley & Ellison 2008) and theoretical (e.g., De Lucia et al. 2004; Tissera et al. 2005; De Rossi et al. 2006; Davé & Oppenheimer 2007) efforts that aimed to explain it. Indeed, one of the main problems is to derive the real metallicity of the ionized gas, because empirical calibrations based on direct estimates of the electron temperature (T_e) of the ionized gas and theoretical methods based on photoionization models provide very different oxygen abundances (e.g., Yin et al. 2007; Kewley & Ellison 2008; Esteban et al. 2009; López-Sánchez & Esteban 2010). Finally, the present understanding of correlations between the HI content, stellar populations, and star-formation in dwarf starburst galaxies is still at a preliminary stage because of the lack of detailed optical/*NIR* images and spectra and/or interferometric HI maps of these systems.

In our series of papers, we have presented a detailed photometric and spectroscopic study of a sample of strong star-forming galaxies, many of them previously classified as dwarf galaxies. The majority of these objects are Wolf-Rayet (WR) galaxies, which are a very inhomogeneous class of star-forming objects that share an ongoing or very recent star-formation event that has produced stars massive enough to evolve to the WR stage (Schaerer et al. 1999). The WR features in the spectra of a galaxy constrains the properties of the star-formation processes. Because the first WR stars typically appear around 2–3 Myr after the starburst is initiated and disappear within some 5 Myr (Meynet & Maeder 2005), their detection informs about both the youth and strength of the burst, offering the opportunity to study an approximately coeval sample of very young starbursts (Schaerer & Vacca 1998).

Our main aim is to study the formation of massive stars in starburst galaxies and the role that interaction with or between dwarf galaxies and/or low surface brightness objects plays in its triggering mechanism. In Paper I (López-Sánchez & Esteban 2008) we introduced the motivation of this work, compiled the list of the analyzed WR galaxies (Table 1 of Paper I), and presented the results of optical/*NIR* broad-band and $H\alpha$ photometry. In Paper II (López-Sánchez & Esteban 2009) we presented the results of our analysis of intermediate-resolution long-slit spectroscopy of 16 objects in our sample of WR galaxies – the results for the other 4 objects were published separately. In Paper II, we also specified the oxygen abundances of the ionized gas (computed following the direct T_e method in the majority of the cases) and analyzed the kinematics of the ionized gas. In Paper III (López-Sánchez & Esteban 2010a), we studied the O and WR stellar populations within these galaxies, and compared them with theoretical evolutionary synthesis models. In

Paper IV (López-Sánchez & Esteban 2010b), we analyzed the optical/*NIR* properties of the galaxies overall, concluding that such detailed analyses are fundamental in understanding the star-formation histories of the galaxies. For this paper, the last in the series, we performed a comprehensive multiwavelength analysis that considers all the optical and *NIR* data but also includes radio, FIR, FUV, and X-ray data available in the literature.

The selection criteria of the galaxy sample were the following. We used the most recent catalog of WR galaxies (Schaerer et al. 1999), which contains a very inhomogeneous group of starbursting objects, to make a list of dwarf objects that could be observed from the Northern Hemisphere. As a result, we considered neither spirals galaxies nor giant H II regions within them, and considered only dwarf objects, such as apparently isolated BCDGs and dwarf irregular galaxies that had peculiar morphologies in previous, shallower imaging. We also chose two galaxies belonging to the Schaerer et al. (1999) catalog that were classified as *suspected* WR galaxies (Mkn 1087 and Tol 9), to confirm the presence of massive stars within them (see Papers II and III). The galaxy IRAS 08339+6517 was also included because previous multiwavelength results suggested that the WR stars could still be present in its youngest star-forming bursts (see López-Sánchez et al. 2006). With this, we got a list of ~40 systems to observe and analyze using the telescopes available at Roque de los Muchachos (La Palma, Spain) and Calar Alto (Almería, Spain) observatories. We added the southern galaxy NGC 5253, for which we obtained deep echelle spectrophotometry using 8.2 m VLT, because of the very intriguing properties it possesses (see López-Sánchez et al. 2007, 2010). The final sample of 20 galaxies was created by considering those galaxies for which we obtained optical/*NIR* broad-band and H α images, plus the deep optical spectroscopy during our observation runs. We already have all these data for other ~15 galaxies, the analysis of these systems will be presented in the future elsewhere, but its preliminary results seem to agree with the main results reported in this paper. Our galaxy sample is therefore not complete, but we consider that it represents dwarf galaxies experiencing a very strong star-formation burst quite well. Indeed, this was the main bias introduced when choosing the galaxy sample, such as we focused only in galaxies on which WR stars are detected. It would be very interesting to extend this analysis to similar star-forming galaxies that do not show WR features, such as the sample of BCDGs analyzed by Gil de Paz et al. (2003).

The structure of this paper is the following. In Sect. 2 we describe the details of the radio, FIR, FUV, and X-ray data extracted from the literature and provide some very useful relations. Section 3 analyzes the star-formation activity in our sample galaxies when considering all multiwavelength calibrators to the SFR. We check that our sample galaxies follow the radio/FIR correlation in Sect. 4. Next, Sect. 5 compiles, analyzes and compares all mass estimations derived in this work. Several mass-metallicity relations are investigated in Sect. 6. We study whether our galaxies satisfy the Schmidt-Kennicutt relation in Sect. 7. Section 8 analyzes and compares several mass-to-light ratios. The dust properties within our starburst galaxies are investigated in Sect. 9. We compare the predictions of the closed-box model with our observational data in Sect. 10. Finally, Sect 11 compiles a quantitative analysis of the interaction features considering all available multiwavelength data. The conclusions reached in our analysis are compiled in Sect. 12. The Appendix describes the main results found in each of the analyzed WR galaxies.

2. Multiwavelength data completeness

We made an exhaustive literature search to complete the optical/*NIR* observations of our WR galaxy sample with data from other wavelengths (radio, far-infrared, far-ultraviolet, and X-ray). Here we describe all these data and the useful properties we have derived from them.

2.1. Radio data

2.1.1. HI data at 21 cm

Observations in the hyperfine transition of the neutral hydrogen, HI, with a rest frequency of 1420.405 MHz, have been key in understanding the distribution and kinematics of the atomic gas within galaxies, including the Milky Way. Neutral gas observations are very important because they are used to determine both the neutral gas mass (HI gas) and the dynamical mass (M_{dyn}) of the systems. Single-dish HI surveys (e.g. Mathewson et al. 1992, the HI *Parkes Sky Survey*, HIPASS, Barnes et al. 2001; Koribalski et al. 2004; Meyer et al. 2004; and the *Arecibo Legacy Fast ALFA* survey, ALFALFA, Giovanelli et al. 2005), give spectra with detected HI emission of thousands of galaxies. However, the best tool for analyzing the neutral gas content in galaxies is via radio interferometer observations (e.g., THINGS; LVHIS; FIGGS; *The HI Rogues Gallery*). Knowing the amount of available neutral gas, the timescale of the starbursts (i.e., the time when the HI cloud will be exhausted if the star-formation activity continues at the current SFR) can be calculated.

Table 1 compiles all HI 21 cm data found for our galaxy sample. The majority of the HI data is provided by single-dish HI observations, but interferometric HI maps are available for a few cases (HGC 31 and IRAS 08339+6517). Table 1 lists the HI flux density, f_{HI} (in units of Jy km s^{-1}), and the HI equivalent width, W_{HI} (in km s^{-1}). For 3 galaxies (POX 4, Tol 9 and NGC 5253) we are using the data provided by our new interferometric maps obtained using the *Australia Telescope Compact Array*. For these objects, we compiled the integrated HI flux and width; their detailed analysis will soon be presented elsewhere (López-Sánchez et al. 2010a,b). SBS 0926+606 was recently observed by Huchtmeier et al. (2007), who gave a combined HI flux for both A and B galaxies, but only interferometric studies can disentangle the amount of neutral gas in each galaxy. Tol 1457-262 and Arp 252 were observed in HI by Casasola et al. (2004) using a single-dish antenna, but they were not detected. Arp 252 was not detected in HI in HIPASS either (Koribalski 2006, priv. comm.). The total HI mass is computed by applying

$$M_{\text{HI}} = 2.356 \times 10^5 d^2 f_{\text{HI}} \quad (1)$$

(Roberts 1975; Roberts & Haynes 1994) where the distance to the galaxy, d , is expressed in Mpc, and the result for the neutral gas mass is given in solar units. The dynamical mass of the system, M_{dyn} , can be estimated from HI radio observations if we consider the inclination-corrected maximum rotation velocity, v_{max}^i , which is obtained at radius R_{max} and assuming a virial equilibrium,

$$M_{\text{dyn}} = 2.31 \times 10^5 R_{\text{max}} (v_{\text{max}}^i)^2, \quad (2)$$

which is the result in solar masses when $v_{\text{max}}^i = \frac{W_{\text{HI}}}{2 \sin i}$ is expressed in km s^{-1} and R_{max} has units of kpc. The inclination angle, i , is defined as what is found between the plane of the sky and the plane of the galaxy (hence, $i = 90^\circ$ in an edge-on

Table 1. Radio data compiled from the literature for our WR galaxy sample.

| Galaxy | F_{HI} [Jy km s ⁻¹] | W_{HI} [km s ⁻¹] | Ref. | $S_{1.4\text{GHz}}$ [mJy] | Ref. |
|-----------------|---------------------------------------------|------------------------------------------|-------|------------------------------|----------|
| HCG 31 AC | 5.15 | 169.2A+190.6C | VM05 | 22 ± 3 | VM05 |
| HCG 31 B | 2.74 | 85.8 | VM05 | 2.1 ± 0.3 | VM05 |
| HCG 31 F | 0.866 | 74.6 | VM05 | ... | ... |
| HCG 31 G | 2.74 | 84.9 | VM05 | 3.3 ± 0.5 | VM05 |
| Mkn 1087 | 5.38 | 270 | GG81 | 12.1 ± 0.6 | Co98 |
| Haro 15 | 3.11 ± 1.01 | 220 | GG81 | 17.8 ± 1.0 | Co98 |
| Mkn 1199 | 1.78 ± 0.67 | 170 | DC04 | 36.2 ± 1.2 | Co98 |
| Mkn 5 | 2.12 ± 0.27 | 22.4 ± 4.9 | Pa03 | <2.8 | HSLD02 |
| IRAS 08208+2816 | ... | ... | ... | 15.2 ± 0.6 | Co98 |
| IRAS 08339+6517 | 3.68 ± 0.46 | ~300 | Ca04 | 33.56 | Co90 |
| POX 4 | 4.31 | 130 | LS10b | 4.2 ± 0.5 | Co98 |
| UM 420 | ... | ... | ... | 1.1 ± 0.3 | HSLD02 |
| SBS 0926+606A | 1.30 ± 0.49 | 120 ± 37 | P02 | 2.7 ± 0.6 | HSLD02 |
| SBS 0926+606B | 1.10 ± 0.49 | 120 ± 37 | P02 | ... | ... |
| SBS 0948+532 | ... | ... | ... | <0.9 | HSLD02 |
| SBS 1054+365 | 4.03 ± 0.39 | 117 ± 11 | Z00 | 1.28 ± 0.14 | BWH95 |
| SBS 1211+540 | 0.71 ± 0.12 | 47 | H05 | <0.9 | HSLD02 |
| SBS 1319+579 | 8.4 | 134 | H07 | <2.9 | HSLD02 |
| SBS 1415+437 | 4.73 ± 0.32 | 66 | H05 | <0.5 | H05 |
| III Zw 107 | 4.48 ± 0.79 | 200 ± 25 | P03 | 8.0 ± 0.5 | Co98+Y01 |
| Tol 9 | 5.02 ± 0.40 | 185 | LS10b | 19.2 ± 0.7 | Co98 |
| Tol 1457-262 | 4.3 | 176 | Kor06 | 38.9 ± 1.8 | Co98+Y01 |
| Arp 252 | ... | ... | Kor06 | 97.6 ± 3.0 | Co98+Y01 |
| NGC 5253 | 42.1 ± 2.3 | 95 ± 3 | LS10a | 78 ± 3 | LS10a |

References. Ca04: Cannon et al. (2004); CBG04: Casasola et al. (2004) Co90: Condon et al. (1990); Co98: Condon et al. (1998); DC04: Davoust & Contini (2004); GG81: Gordon & Gottesman (1981); HSLD02: Hopkins et al. (2002); H05: Huchtmeier et al. (2005); H07: Huchtmeier et al. (2007); Kor06: Koribalski (2006), priv. comm.; LS10a: López-Sánchez et al. (2010a); LS10b: López-Sánchez et al. (2010b); Pa03: Paturel et al. (2003); HyperLEDA; P02: Pustilnik et al. (2002); VM05: Verdes-Montenegro et al. (2005); Y01: Yun et al. (2001); Z00: Zasov et al. (2000).

galaxy and $i = 0^\circ$ in a face-on galaxy). We usually estimated this angle by assuming that the elliptical shape of the galaxy is just a consequence of its orientation. The usual problem deriving virial masses is not knowing the of the inclination angle, and sometimes also R_{max} , especially in galaxies showing disturbed morphologies. We adopted the maximum radius observed in our deep optical images. Therefore, because the extension of the neutral gas is usually more than the extension of the stellar component, our values of M_{dyn} may be underestimated. The gas depletion timescale defined by Skillman et al. (2003) was computed using M_{HI} and the assumed SFR derived for each galaxy (see below).

2.1.2. Radio-continuum data

For an individual star-forming galaxy, the SFR is directly proportional to its radio luminosity (i.e., Condon 1992). Hence, the radio continuum flux is widely used as a dust-free indicator of the star-formation rate. Nearly all of the radio-continuum luminosity from galaxies without a significant active galactic nucleus (AGN) can be traced to recently formed massive ($M \geq 8 M_\odot$) stars (Condon et al. 1992). The 10% of the continuum emission at 1.4 GHz comes from free-free emission from extremely massive main-sequence stars (thermal emission) and almost 90% is synchrotron radiation from relativistic electrons accelerated in the remnants of core-collapse supernovae (nonthermal emission). Because the stars that contribute significantly to the radio emission have lifetimes $\tau \leq 3 \times 10^7$ yr and the relativistic electrons have lifetimes $\tau \leq 10^8$ yr, the current radio luminosity is nearly proportional to the rate of massive star-formation during

the past $\tau \leq 10^8$ yr (Condon et al. 2002):

$$SFR_{1.4\text{GHz}} (M > 5 M_\odot) \sim 2.5 \times 10^{-22} L_{1.4\text{GHz}}, \quad (3)$$

where $L_{1.4\text{GHz}}$ has units of W Hz^{-1} .

Table 1 compiles also all the 1.4 GHz radio-continuum flux data available for our WR galaxy sample in the literature. The 1.4 GHz luminosity, $S_{1.4\text{GHz}}$, can be computed using the expression given by Yun et al. (2001):

$$\log L_{1.4\text{GHz}} = 20.07 + 2 \log d + \log S_{1.4\text{GHz}}, \quad (4)$$

where the result is given in units of W Hz^{-1} , the distance d is expressed in Mpc and $S_{1.4\text{GHz}}$ is expressed in Jy. In the case of IRAS 08339+6517, the $S_{1.4\text{GHz}}$ was computed from the $S_{1.49\text{GHz}}$ value given by (Condon et al. 1990) using the (Condon et al. 2002) relation between both quantities, as it was explained in López-Sánchez et al. (2006).

Radio-continuum observations at several cm wavelengths are used to quantify the thermal and nonthermal contributions, and thereby distinguish older and supernova-rich regions from younger and mostly thermal areas (i.e., Deeg et al. 1993; Beck et al. 2000; Cannon et al. 2004, 2005). These observations also permit detecting of extremely young, dense, heavily embedded star clusters (Kobulnicky & Johnson 1999; Johnson & Kobulnicky 2003). Although radio data at frequencies different from 1.4 GHz are not usually available for this kind of galaxy, we applied the equation provided by Dopita et al. (2002),

$$F_{1.4\text{GHz thermal}} = 1.21 \times 10^{12} F_{\text{H}\alpha}, \quad (5)$$

to obtain an estimation of the thermal emission at 1.4 GHz, $F_{1.4\text{GHz thermal}}$, using the $\text{H}\alpha$ flux derived from our images (see Paper I). In this equation, $F_{\text{H}\alpha}$ is in units of $\text{erg cm}^{-2} \text{s}^{-1}$, and

the result is given in mJy. The comparison between $F_{1.4\text{GHz}}^{\text{thermal}}$ and $F_{1.4\text{GHz}}$ allows estimation of the nonthermal flux. Condon (1992) and Niklas et al. (1997) indicated that the nonthermal component is more than 90% of the total at this frequency. It is common to consider the nonthermal to thermal ratio, R ; Dopita et al. (2002) report that the average value in starburst galaxies is $\log R = 1.3 \pm 0.4$. Radio continuum and FIR data help to discern the normal or active (that is, a galaxy hosting an AGN) nature.

2.2. FIR data

Many of the problems found to derive the SFR from optical data can be avoided by measuring the far-infrared (FIR) and sub-millimeter spectral energy distributions (SEDs). These are determined by the re-radiation as thermal continuum by the dust grains of stellar photospheric radiation absorbed in the visible and UV regions of the spectrum. Assuming that the dust completely surrounds the star-forming regions, it acts as a bolometer reprocessing the luminosity produced by the stars. Therefore, the SFR can be also computed using theoretical stellar flux distributions and evolutionary models. Kennicutt (1998) provides the following correlation between the SFR (in units of $M_{\odot} \text{ yr}^{-1}$) and the far-infrared flux:

$$SFR_{\text{FIR}} = 4.5 \times 10^{-44} L_{\text{FIR}}, \quad (6)$$

where L_{FIR} (given in units of erg s^{-1}) is obtained using the FIR flux between 42.5 and 122.5 μm (Sanders & Mirabel 1996),

$$F_{\text{FIR}} = 1.26 \times 10^{-11} (2.58 f_{60} + f_{100}), \quad (7)$$

with f_{60} and f_{100} the flux densities (in Jy) for 60 μm and 100 μm and the conventional expression between flux and luminosity, $L = 4\pi d^2 F$. This relation can only be applied in starbursts with ages less than 10^8 yr, where the approximations assumed by Kennicutt (1998) are valid. If the SFR value derived from L_{FIR} agrees with that estimated from the $H\alpha$ luminosity, we may consider that the correction by extinction done to derive the $H\alpha$ flux is correct.

Assuming that all the UV and blue radiation from massive stars is absorbed by grains and is re-emitted as thermal radiation in the 40–120 μm band, Condon (1992) derives the following relation between SFR and $L_{60\mu\text{m}}$ (in units of W Hz^{-1}):

$$SFR_{60\mu\text{m}} \sim 1.96 \times 10^{-24} L_{60\mu\text{m}}, \quad (8)$$

i.e.,

$$SFR_{60\mu\text{m}} \sim 2.346 \times 10^{-4} f_{60\mu\text{m}} d^2, \quad (9)$$

with $f_{60\mu\text{m}}$ expressed in Jy and d in Mpc. Although some authors (Lonsdale et al. 1984) have argued that radiation from stars less massive than $5 M_{\odot}$ will contribute significantly to FIR emission from galactic disks, this relation seems to give acceptable values for the SFR.

Roussel et al. (2001) provide an alternative SFR calibration using the 15 μm luminosity:

$$SFR_{15\mu\text{m}} \sim 3.66 \times 10^{-3} d^2 f_{15\mu\text{m}}, \quad (10)$$

where $f_{15\mu\text{m}}$ is the monochromatic flux at 15 μm , and d the distance in Mpc. This formula is only applicable when the mid-infrared emission is dominated by unidentified infrared bands (UIBs) with a negligible, very small-grain (VSG) continuum, which is the case in disk galaxies, but is not always verified at 15 μm in galactic central regions. It may be assumed that $L_{15\mu\text{m}} \sim L_{12\mu\text{m}}$.

The warm dust mass can be estimated using the 60 and 100 μm fluxes and applying the relation given by Huchtmeier et al. (1995),

$$M_{\text{dust}} = 4.78 d^2 f_{100\mu\text{m}} \left(\exp \left[2.94 \left(\frac{f_{100\mu\text{m}}}{f_{60\mu\text{m}}} \right)^{0.4} \right] - 1 \right), \quad (11)$$

where the distance is expressed in Mpc, the flux densities are in Jy, and the result is given in M_{\odot} .

We used the far-infrared (FIR) data provided by the *Infrared Astronomical Satellite* (IRAS) to obtain the monochromatic fluxes at 12, 25, 60, and 100 μm . These data were used to independently estimate the SFR and to derive the warm dust mass within each galaxy. We also checked if the galaxies follow the FIR-radio relationship. Table 2 compiles all the FIR data found for our sample of WR galaxies, and three of them have no useful measurements at these frequencies.

2.3. FUV data

In the past few years, the *GALaxy Evolution Explorer* (GALEX) satellite has been providing astonishing ultraviolet (UV) images of galaxies and revealing recent star-formation activity in their external regions (i.e., Gil de Paz 2005, 2007; Thilker et al. 2005; Koribalski & López-Sánchez 2009). The GALEX point spread function in the central 0.5° has a full width at half-maximum of ~ 5 arcsec, matching the spatial resolution of our optical/NIR images quite nicely. We searched for GALEX observations of the galaxies that compose our sample in the far-UV-band (FUV, 1350–1750 \AA), all of them have useful FUV data except four objects (Mkn 1087, Mkn 1199, SBS 0948+532 and III Zw 107).

In general, the FUV emission of our sample galaxies matches their optical emission fairly closely. In many cases, FUV emission is much more extended than the $H\alpha$ emission. Figure 1 shows the examples of the GALEX FUV images of HCG 31, Haro 15, and SBS 0926+606. As we can see when comparing with our optical images (see Paper I), the star-forming regions are clearly observed in FUV. Brief comments about three galaxies follow.

- The eastern tail of SBS 0926+606 B is quite bright in the FUV image, suggesting an extended distribution of massive OB stars that we do not detect in our deep $H\alpha$ image (see Fig. 15 and Sect. 3.10.1 in Paper I);
- the star-forming galaxy #15 in Tol 1457-262 is clearly detected in the FUV emission, but the faint galaxy #16 is not seen (Fig. 31 and Sect. 3.18.1 in Paper I); and
- in Arp 252, FUV emission is detected not only at the center of the galaxies (ESO 566-8 and ESO 566-7) but also throughout the tails and in tidal dwarf candidates *c*, *e*, and *d* (see Fig. 34 and Sect. 3.19.1 in Paper I).

The FUV data can be used to get an independent estimation of the SFR of the galaxies. UV-emission probes star-formation on timescales of ~ 100 Myr, the lifetime of the massive OB stars. We integrated the counts per second (CPS) within each galaxy or region and then applied $m_{\text{FUV}} = -2.5 \log(\text{CPS}) + 18.82$ (Morrissey et al. 2005) to derive the magnitude in the FUV-band. We compiled the m_{FUV} found for each galaxy in Table 2. We then corrected by extinction using $A_{\text{FUV}} = 7.9E(B - V)$. The value of $E(B - V)$ adopted for every region was derived from our optical spectroscopy and is compiled in Table 5 of Paper I. We then applied

$$f_{\text{FUV}} = 1.40 \times 10^{-15} \times 10^{0.4(18.82 - m_{\text{FUV}}^0)}, \quad (12)$$

Table 2. FIR and FUV data for the WR galaxy sample analyzed in this work.

| Galaxy | $f_{12\mu\text{m}}$ [Jy] | $f_{25\mu\text{m}}$ [Jy] | $f_{60\mu\text{m}}$ [Jy] | $f_{100\mu\text{m}}$ [Jy] | F_{FIR} ^a | Reg. ^b | m_{FUV} [mag] | f_{FUV} ^c |
|-----------------|-----------------------------|-----------------------------|-----------------------------|------------------------------|----------------------------------|----------------------|---------------------------|----------------------------------|
| HCG 31 | 0.110 ± 0.020 | 0.580 ± 0.040 | 3.92 ± 0.31 | 5.84 ± 0.47 | 2.01 ± 0.16 | AC | 14.97 ± 0.06 | 7.54 ± 0.44 |
| | | | | | | B | 16.80 ± 0.09 | 3.32 ± 0.26 |
| | | | | | | E | 18.01 ± 0.08 | 0.456 ± 0.035 |
| | | | | | | F | 18.24 ± 0.11 | 0.460 ± 0.047 |
| | | | | | | G | 15.93 ± 0.06 | 3.11 ± 0.18 |
| | | | | | | H | 20.63 ± 0.40 | 0.0041 ± 0.0014 |
| Mkn 1087 | 0.103 ± 0.029 | 0.414 ± 0.058 | 3.03 ± 0.33 | 4.44 ± 0.40 | 1.54 ± 0.16 | ... | ... | ... |
| Haro 15 | 0.118 ± 0.034 | 0.297 ± 0.089 | 1.36 ± 0.12 | 1.97 ± 0.20 | 0.690 ± 0.064 | ... | 15.12 ± 0.07 | 9.41 ± 0.57 |
| Mkn 1199 | 0.282 ± 0.031 | 1.28 ± 0.09 | 6.82 ± 0.34 | 8.85 ± 0.53 | 3.33 ± 0.18 | ... | ... | ... |
| Mkn 5 | <0.0503 | <0.0533 | 0.21 ± 0.04 | <0.8473 | <1.75 | ... | 17.76 ± 0.07 | 1.59 ± 0.10 |
| IRAS 08208+2816 | 0.126 ± 0.029 | 0.278 ± 0.067 | 1.15 ± 0.09 | 1.70 ± 0.17 | 0.588 ± 0.051 | ... | 16.59 ± 0.07 | 3.75 ± 0.23 |
| IRAS 08339+6517 | 0.250 ± 0.025 | 1.13 ± 0.02 | 5.81 ± 0.04 | 6.48 ± 0.09 | 2.71 ± 0.02 | ... | 15.37 ± 0.06 | 10.7 ± 0.6 |
| | | | | | | c | 19.70 ± 0.10 | 0.160 ± 0.014 |
| POX 4 | <0.987 | 0.153 ± 0.040 | 0.629 ± 0.057 | <0.5798 | <0.278 | POX 4 | 16.03 ± 0.06 | 2.82 ± 0.16 |
| | | | | | | Comp. | 19.06 ± 0.12 | 0.269 ± 0.030 |
| UM 420 | ... | <0.275 | 0.411: | 0.613: | 0.211: | ... | 18.22 ± 0.06 | 0.377 ± 0.021 |
| SBS 0926+606 | <0.07553 | <0.08818 | 0.269 ± 0.046 | <0.5296 | <0.154 | A | 16.71 ± 0.06 | 1.75 ± 0.09 |
| | | | | | | B | 17.84 ± 0.10 | 0.829 ± 0.073 |
| SBS 0948+532 | ... | ... | ... | ... | ... | ... | ... | ... |
| SBS 1054+365 | <0.055 | <0.100 | 0.536 ± 0.048 | 0.97 ± 0.15 | 0.296 ± 0.035 | ... | 16.67 ± 0.07 | 1.18 ± 0.08 |
| SBS 1211+540 | ... | ... | ... | ... | ... | ... | 18.40 ± 0.07 | 0.370 ± 0.022 |
| SBS 1319+579 | ... | ... | 0.209: | 0.685: | 0.154: | ... | 17.00 ± 0.06 | 0.864 ± 0.048 |
| | | | | | | A | 18.60 ± 0.06 | 0.199 ± 0.010 |
| SBS 1415+437 | ... | ... | ... | ... | ... | ... | 16.22 ± 0.06 | 3.95 ± 0.22 |
| III Zw 107 | <0.0968 | 0.336 ± 0.050 | 1.37 ± 0.20 | 1.72 ± 0.31 | 0.662 ± 0.104 | ... | ... | ... |
| Tol 9 | 0.111 ± 0.030 | 0.465 ± 0.051 | 2.71 ± 0.22 | <5.516 | <1.58 | ... | 17.57 ± 0.07 | 4.22 ± 0.22 |
| Tol 1457-262 | <0.117 | 0.611 ± 0.067 | 3.09 ± 0.19 | 3.68 ± 0.40 | 1.47 ± 0.11 | ... | 15.84 ± 0.07 | 6.95 ± 0.47 |
| | | | | | | Obj 1 | 16.15 ± 0.06 | 5.26 ± 0.29 |
| | | | | | | Obj 2 | 17.41 ± 0.13 | 1.64 ± 0.18 |
| | | | | | | #15 | 19.71 ± 0.21 | 0.199 ± 0.037 |
| Arp 252 | 0.188 ± 0.023 | 0.994 ± 0.050 | 3.91 ± 0.20 | 4.11 ± 0.25 | 1.79 ± 0.10 | A | 18.67 ± 0.08 | 1.91 ± 0.13 |
| | | | | | | B | 18.84 ± 0.07 | 0.441 ± 0.027 |
| NGC 5253 | 2.50 ± 0.02 | 12.07 ± 0.05 | 29.84 ± 0.07 | 30.08 ± 0.21 | 13.49 ± 0.05 | ... | 12.81 ± 0.06 | 123.0 ± 6.5 |

Notes. ^(a) In units of 10^{-10} erg s^{-1} cm^{-2} .

^(b) Region within each system (HCG 31, IRAS 08339+6517, POX 4, SBS 0926+606, SBS 1319+579, Tol 1457-262, and Arp 252; see Paper I).

^(c) In units of 10^{-14} erg s^{-1} cm^{-2} \AA^{-1} .

where $m_{\text{FUV}}^0 = m_{\text{FUV}} - A_{\text{FUV}}$ and f_{FUV} is obtained in units of $\text{erg s}^{-1} \text{cm}^{-2} \text{\AA}^{-1}$. The value of f_{FUV} computed for each galaxy is also shown in Table 2. Once the FUV luminosity is computed ($L_{\text{FUV}} = 4\pi d^2 f_{\text{FUV}}$), the FUV-based SFR is derived applying the calibration provided by Salim et al. (2007),

$$SFR_{\text{FUV}} = 8.1 \times 10^{-41} L_{\text{FUV}}. \quad (13)$$

The seven column in Table 2 indicates the region within each system for which we derived the FUV flux. The FIR emission provided by IRAS does not allow distinguishing between these regions, but FUV data provided by GALEX does. In Arp 252, region A is galaxy ESO 566-8 and region B is galaxy ESO 566-7 (see Sect. 3.19 in Paper I).

2.4. X-ray data

Finally, we also looked for the X-ray data available for our WR galaxy sample. Only four objects (HCG 31 AC, IRAS 08339+6517, Tol 9 and NGC 5253) have been observed at these high frequencies; their X-ray luminosities are compiled in Table 3. In the case of Tol 9, the upper limit to the X-ray luminosity was derived from the upper limit to the X-ray flux reported by Fabbiano et al. (1982), $f_{0.5-3 \text{ keV}} < 1.2 \times 10^{-13}$ erg $\text{cm}^{-2} \text{s}^{-1}$,

Table 3. X-ray data available for our WR galaxy sample.

| Galaxy | $\log L_{\text{X}(0.2-2.0 \text{ keV})}$ [erg s^{-1}] | Ref. |
|-----------------|-----------------------------------------------------------------|--------------|
| HCG 31 | 40.88 ± 0.13 | ^a |
| IRAS 08339+6517 | 41.45 | ^a |
| Tol 9 | $<40.29^a$ | ^b |
| NGC 5253 | 38.60 ± 0.18 | ^a |

Notes. ^(a) Stevens & Strickland (1998b); ^(b) Fabbiano et al. (1982).

and assuming a distance of 86.6 Mpc (see Table 1, Paper I). We then multiplied the derived X-ray luminosity by 0.72 to correct for the X-ray range. Beside these data, we also use (see Sect. 3.3) the WR galaxy sample that Stevens & Strickland (1998a,b) observed in X-ray.

3. Analysis of the star-formation rates

The SFR, defined as the stellar mass formed per unit time, is the standard parameter used to quantify the star-formation activity in galaxies. Determination of the SFR is fundamental to a proper understanding of the formation and evolution of the galaxies. As

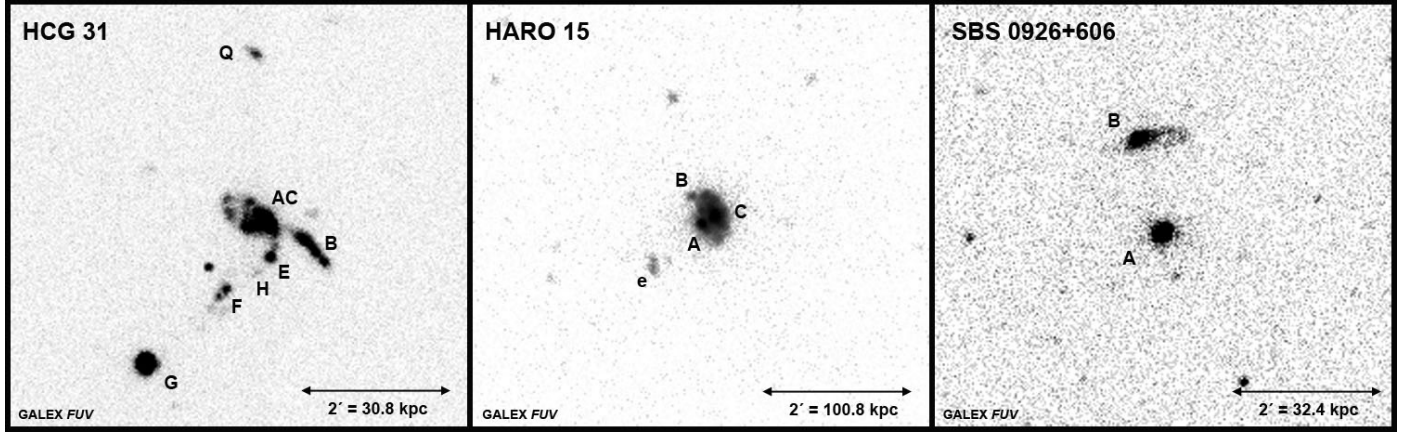


Fig. 1. Example of GALEX images, showing the FUV emission in HCG 31, Haro 15 and SBS 0926+606. Regions within each object have been labeled following the notation given in Paper I.

said in the introduction, different techniques involving different data sets from *UV* to radio often yield different SFR results. Part of the problem is related to the unknown amount of extinction within each particular galaxy (Calzetti 2001), such as the amount of dust obscuration depending on the galaxy mass, galaxy type, the chemical evolutionary state, gas content, or even if the galaxy is interacting or merging with another independent object. As explained in the previous section, FIR and radio data provide an extinction-free estimation of the SFR, while FUV emission nicely traces the very young stellar component. Here, we analyzed all the available multiwavelength data for our sample of WR galaxies, including our reddening-corrected $H\alpha$ estimations (see Paper I), to determine the SFR within these objects in a comprehensive way.

Table 4 compiles all FUV, *U*, *B*, $H\alpha$, *H*, FIR, 15 μm , 60 μm , and 1.4 GHz luminosities for the galaxies analyzed in this work. The *U*, *B*, and *H* luminosities were computed from the reddening-corrected absolute magnitudes in the *U*, *B*, and *H* bands (see Paper I) using the standard equation $\log L_x = 0.4 \times (M_{x,\odot} - M_x)$ and considering $M_{U,\odot} = 5.58$ and $M_{B,\odot} = 5.48$ (Bessell et al. 1998) and $M_{H,\odot} = 3.35$ (Colina et al. 1996). We note that the FIR and 60 μm luminosities in UM 420 are overestimated because of the contribution of the foreground galaxy UGC 01809 (see Fig. 13 and Sect. 3.9.1 in Paper I).

We used the values listed in Table 4 to estimate the SFR that each object experiences, following the different multiwavelength techniques explained in the previous section. Table 5 compiles all SFR values derived for each galaxy. The values of the $H\alpha$ -based SFR listed in this table were extracted from Paper I and consider the Kennicutt (1998) calibration. Recently, Calzetti et al. (2007) re-calibrated the relationship between the $H\alpha$ -luminosity and the SFR; the $H\alpha$ -based values of the SFR provided by Calzetti et al. (2007) are 0.67 times the values derived using the Kennicutt (1998) calibration.

From Table 5, it is evident that the agreement between values obtained with different methods is usually good, although sometimes we find clear discrepancies (i.e. POX 4, NGC 5253). For systems that involve two or more galaxies (HCG 31, SBS 0926+606, Tol 1457-262, and Arp 252), we list both the global and individual SFRs, because the FIR and the radio data do not have enough spatial resolution to distinguish the emission coming from different members, but FUV and $H\alpha$ data do. We also considered HCG 31 F1 and F2 as a single entity (HCG 31 F) because the available H I data include both TDG candidates.

Figure 2 compares our $H\alpha$ -based SFR (corrected for both extinction and [N II] contribution as explained in Appendix C of Paper I) with the SFR estimations derived from FIR, 15 μm , 60 μm , and 1.4 GHz luminosities. The diagram involving $L_{15\mu\text{m}}$ seems to show a higher scatter at higher SFR, but this calibration is more uncertain. As a particular case, Arp 252 always shows a disagreement between the SFR derived from $H\alpha$ and other parameters, noticeable with the 1.4 GHz luminosity. The main object within Arp 252 is the bright galaxy ESO 566-8. This behavior, together with the FIR-radio-continuum relation not being satisfied in this system (see below), strongly suggest that ESO 566-8 has some activity different to its starbursting nature (an AGN or a radio-galaxy), something we already commented on when we analyzed this system (see Sect. 3.19.2 of Paper I). The rest of the objects agree fairly well when comparing values obtained from different calibrations. As previous authors have pointed out (i.e. Dopita et al. 2002; James et al. 2005), the correction of the $H\alpha$ fluxes for both extinction and [N II] emission is vital to a reliable estimation of the SFR using $H\alpha$ -images.

Although the agreement between the $H\alpha$ -based SFR and the SFRs derived using FIR and radio luminosities is good, we observe that the values provided using the $H\alpha$ luminosity are slightly higher than those estimated using the other calibrations. The difference seems to be higher at lower $H\alpha$ -luminosities. A linear fit to the data (Fig. 2) confirms this trend. The zero-points of the fits (0.59, 0.52, 0.58, 0.68 for the $H\alpha$ -FIR, $H\alpha$ -1.4 GHz, $H\alpha$ -60 μm , and $H\alpha$ -15 μm relations, respectively) indicate that, for $\text{SFR} = 1 M_\odot \text{yr}^{-1}$, the value of the SFR provided by $H\alpha$ -luminosity is ~ 0.6 times the SFR values estimated using the other relations. Bell (2003) concludes that both radio and FIR luminosities underestimate the SFR for low-luminosity galaxies because the nonthermal emission seems to be suppressed by a factor of 2–3 in dwarf objects. However, the difference is not significant if we use the Calzetti et al. (2007) calibration instead of the Kennicutt (1998) calibration to derive the $H\alpha$ -based SFR.

The comparison of the FUV-based with the $H\alpha$ -based SFR (Fig. 3) also shows good agreement: except for some few objects (remarkably SBS 0926+606 B¹), both relations provide similar values. We also observe that the FUV-based SFRs seem to be slightly lower than the $H\alpha$ -based SFRs. A linear fit to the data

¹ As pointed out before, the FUV emission observed in SBS 0926+606 B is much more extended than the $H\alpha$ emission, so the derived SFR is more than one order of magnitude higher when using the FUV than with the $H\alpha$ emission.

Table 4. FUV, U , B , $H\alpha$, H , FIR, $15\ \mu\text{m}$, $60\ \mu\text{m}$, and $1.4\ \text{GHz}$ luminosities for all galaxies analyzed in this work.

| Galaxy | L_{FUV} [$10^{39}\ \text{erg s}^{-1}\ \text{\AA}^{-1}$] | L_U [$10^8 L_\odot$] | L_B [$10^8 L_\odot$] | $L_{H\alpha}$ [$10^{40}\ \text{erg s}^{-1}$] | L_H [$10^8 L_\odot$] | L_{FIR} [$10^{42}\ \text{erg s}^{-1}$] | $L_{15\mu\text{m}}$ [$10^{22}\ \text{W Hz}^{-1}$] | $L_{60\mu\text{m}}$ [$10^{23}\ \text{W Hz}^{-1}$] | $L_{1.4\text{GHz}}$ [$10^{20}\ \text{W Hz}^{-1}$] |
|---------------------------|-----------------------------------------------------------------------|-----------------------------|-----------------------------|---------------------------------------------------|-----------------------------|------------------------------------------------------|--------------------------------------------------------|--------------------------------------------------------|--------------------------------------------------------|
| HCG 31 | 49 ± 3 | 356 | 202 ± 7 | 52 ± 4 | 42.2 | 72 ± 6 ^a | 3.9 ± 0.7 ^a | 14.1 ± 1.1 ^a | 98 ± 14 |
| " AC | 24.9 ± 1.5 | 175 | 92 ± 4 | 36.3 ± 2.3 | 18.0 | ... | ... | ... | 79 ± 11 |
| " B | 11.0 ± 0.9 | 73.8 | 47.4 ± 1.8 | 3.1 ± 0.3 | 10.0 | ... | ... | ... | 7.5 ± 1.1 |
| " E | 1.51 ± 0.12 | 6.3 | 3.13 ± 0.17 | 1.49 ± 0.16 | 0.586 | ... | ... | ... | ... |
| " F ^b | 1.52 ± 0.15 | 10.9 | 4.0 ± 0.2 | 5.0 ± 0.3 | 0.486 | ... | ... | ... | ... |
| " H | 0.13 ± 0.05 | ... | ... | 0.045 ± 0.013 | ... | ... | ... | ... | ... |
| " G | 10.3 ± 0.6 | 90.4 | 55 ± 2 | 6.4 ± 0.4 | 13.1 | ... | ... | ... | 11.9 ± 1.8 |
| Mkn 1087 | ... | 1803 | 1127 ± 83 | 70 ± 5 | 360 | 228 ± 23 | 15 ± 4 | 45 ± 5 | 178 ± 9 |
| " N | ... | ... | 26.1 ± 0.9 | 2.27 ± 0.19 | 5.01 | ... | ... | ... | ... |
| Haro 15 | 84 ± 5 | 614 | 347 ± 13 | 42 ± 5 | 124 | 62 ± 6 | 11 ± 3 | 12.2 ± 1.1 | 160 ± 9 |
| Mkn 1199 | ... | 479 | 291 ± 11 | 49 ± 7 | 344 | 116 ± 6 | 9.8 ± 1.1 | 23.8 ± 1.2 | 126 ± 4 |
| " NE | ... | 21.1 | 16.6 ± 0.6 | 0.90 ± 0.23 | 21.7 | ... | ... | ... | ... |
| Mkn 5 | 0.274 ± 0.018 | 4.21 | 2.63 ± 0.10 | 0.582 ± 0.014 | 1.89 | <0.30 | <0.087 | 0.036 ± 0.007 | 3.9 ± 0.8 |
| IRAS 08208+2816 | 162 ± 10 | 879 | 511 ± 14 | 142 ± 12 | 373 | 254 ± 22 | <5.5 | 49.7 ± 4.0 | 657 ± 26 |
| IRAS 08339+6517 | 79 ± 4 | 1159 | 661 ± 23 | 120 ± 6 | 592 | 198.6 ± 1.8 | 18.3 ± 1.8 | 42.6 ± 0.3 | 249 ± 37 |
| " Comp. | 1.17 ± 0.10 | 38 | 29.9 ± 1.6 | 2.1 ± 0.4 | 23.3 | ... | ... | ... | ... |
| POX 4 | 7.0 ± 0.4 | 104.7 | 51.1 ± 0.5 | 23.3 ± 1.9 ^c | 17.9 | 6.9 ± 0.5 | <24 | 1.56 ± 0.14 | 10.4 ± 1.2 |
| " Comp. | 0.667 ± 0.075 | 2.42 | 2.17 ± 0.07 | 0.188 ± 0.018 ^c | 1.1: | ... | ... | ... | ... |
| UM 420 | 25.4 ± 1.4 | 236 | 103 ± 4 | 47 ± 3 | 57 | 142: | ... | 27.7 | 74 ± 34 |
| SBS 0926+606 ^b | 41.4 ± 3.4 | 52.3 | 26.6 ± 0.8 | 11.8 ± 0.7 | 9.49 | 5.8 ± 0.6 | 2.8 | 1.01 ± 0.17 | 10 ± 2 |
| " A | 6.4 ± 0.4 | 28.1 | 12.8 ± 0.4 | 9.4 ± 0.5 | 3.63 | ... | ... | ... | ... |
| " B | 35 ± 3 | 24.2 | 13.8 ± 0.4 | 2.4 ± 0.2 | 5.86 | ... | ... | ... | ... |
| SBS 0948+532 | ... | 121.3 | 36.7 ± 1.0 | 78 ± 3 | 15.8 | ... | ... | ... | <38 |
| SBS 1054+365 | 0.090 ± 0.006 | 0.982 | 0.655 ± 0.018 | 0.450 ± 0.017 | 0.413 | 0.23 ± 0.03 | <0.042 | 0.041 ± 0.005 | 0.098 ± 0.011 |
| SBS 1211+540 | 0.076 ± 0.005 | 0.608 | 0.316 ± 0.008 | 0.141 ± 0.005 | 0.127 | ... | ... | ... | <0.50 |
| SBS 1319+579 | 0.86 ± 0.05 | 63.1 | 40.2 ± 1.4 | 2.38 ± 0.15 | 28.6 | 5.3: | ... | 0.85 | <2.9 |
| SBS 1415+437 | 0.409 ± 0.023 | 1.69 | 1.00 ± 0.03 | 0.50 ± 0.02 | 0.581 | ... | ... | ... | <0.052 |
| III Zw 107 | ... | 286 | 177 ± 5 | 40.1 ± 1.8 | 77.3 | 50 ± 8 | <7.3 | 10.4 ± 1.5 | 62 ± 4 |
| Tol 9 | 9.5 ± 0.7 | 118 | 79 ± 2 | 22.9 ± 1.6 | 55.5 | 35.4 ± 1.6 | 2.5 ± 0.7 | 6.1 ± 0.5 | 87.3 ± 1.6 |
| Tol 1457-262 ^b | 38.6 ± 2.6 | 319 | 182 ± 5 | 63 ± 3 | 109 | 82 ± 6 | <6.5 | 17.2 ± 1.1 | 216 ± 10 |
| " Obj 1 | 29.2 ± 1.6 | 223 | 121 ± 3 | 46.2 ± 2.7 | 58.6 | ... | ... | ... | ... |
| " Obj 2 | 9.2 ± 1.1 | 97.3 | 60.3 ± 1.7 | 17.2 ± 0.8 | 45.3 | ... | ... | ... | ... |
| " #15 | 1.10 ± 0.21 | 8.39 | 6.08 ± 0.23 | 0.47 ± 0.04 | 5.5: | ... | ... | ... | ... |
| Arp 252 ^b | 47.4 ± 3.3 | 711 | 435 ± 13 | 90 ± 6 | 423 | 361 ± 19 | 38 ± 5 | 79 ± 4 | 1968 ± 60 |
| " ESO 566-8 | 38.5 ± 2.7 | 597 | 350 ± 10 | 84 ± 6 | 313 | ... | ... | ... | ... |
| " ESO 566-7 | 8.9 ± 0.6 | 114 | 85 ± 3 | 6.3 ± 0.4 | 110 | ... | ... | ... | ... |
| NGC 5253 | 2.35 ± 0.15 | 36.6 | 22.9 ± 0.2 | 4.4 ± 0.2 | 14.2 | 2.583 ± 0.009 | 0.479 ± 0.004 | 0.571 ± 0.001 | 1.47 ± 0.06 |

Notes. ^(a) As IRAS data do not allow to be distinguished regions within the HCG 31 group, this value considers the flux of all galaxy members. ^(b) We are considering the flux of two galaxies: members F1 and F2 for HCG 31 F; galaxies A and B for SBS 0926+606; *obj 1* and *obj 2* for Tol 1457-262; and ESO 566-8 (A) and ESO 566-7 (B) for Arp 252. ^(c) As we pointed out in Paper I, the $H\alpha$ flux for POX 4 provided by Méndez & Esteban (1999) seems to be overestimated, so we consider here the value provided by Gil de Paz et al. (2003), which is 0.61 times smaller. We also scale our $H\alpha$ flux of POX 4 Comp using this factor.

(shown in Fig. 3 with a continuous green line and with a correlation coefficient of $r = 0.927$) indicates that the FUV-based SFR is, on average, ~ 0.71 times the $H\alpha$ -based SFR. This value is similar to the factors found before when comparing the $H\alpha$ -based SFR with the FIR- and radio-based SFRs. Interestingly, all these numbers are coincident with the ratio between the Kennicutt (1998) and the Calzetti et al. (2007) calibrations to the SFR using the $H\alpha$ flux, $SFR_{\text{C07}}(H\alpha)/SFR_{\text{K98}}(H\alpha) = 0.67$. We therefore conclude that the new $H\alpha$ -based calibration provided by Calzetti et al. (2007) should be preferred over the widely-used Kennicutt (1998) calibration when computing the SFR from $H\alpha$ luminosities. The SFR estimated for each object by considering all available multiwavelength data and listed in last column of Table 5, was computed considering the Calzetti et al. (2007) value. Finally, we must say that there is increasing evidence that the $H\alpha$ luminosity underestimates the SFR relative to the FUV luminosity in dwarf galaxies with $SFR \leq 0.01 M_\odot \text{ yr}^{-1}$

(i.e., Lee et al. 2009; Pflamm-Altenburg et al. 2009), so the FUV-based SFR should be preferred over the $H\alpha$ -based SFR in those systems.

3.1. L_B -SFR and L_U -SFR relations for starburst galaxies

Just for comparison, we also estimated the SFR from the B -luminosity using the calibration provided by Gallagher et al. (1984). SFR_B represents the star-formation activity that occurred in the past few hundred Myr, while the rest of the calibrations trace the massive stars and the nebular emission of the gas that only last for some tens of Myr. For our galaxy sample, SFR_B is always lower than the SFR derived from the other calibrations, as we should expect because of the starbursting nature of the analyzed galaxies. The value of the SFR_B in Mkn 1087 using the Gallagher et al. (1984) equation is only half of what is estimated

Table 5. SFR values (in units of $M_{\odot} \text{ yr}^{-1}$) derived for each galaxy using different luminosities and calibrations.

| Galaxy | FUV | U | B | | $H\alpha$ | FIR | 15 μm | 60 μm | 1.4 GHz | Assumed |
|-----------------|---------------------|----------|--------|----------|-------------------|-----------------|------------------|-------------------|-------------------|---------|
| | S07 | Eq. (15) | G84 | Eq. (14) | K98 | K98 | R01 | C92 | C02 | SFR |
| HCG 31 | 4.0 ± 0.3 | 2.8 | 0.59 | 2.5 | 4.1 ± 0.4 | 3.3 ± 0.3 | 1.2 ± 0.2 | 2.8 ± 0.2 | 2.5 ± 0.2 | 3.1 |
| " AC (NGC 1741) | 2.02 ± 0.12 | 1.5 | 0.27 | 1.2 | 2.88 ± 0.18 | ... | ... | ... | 1.98 ± 0.03 | 2.0 |
| " B | 0.89 ± 0.07 | 0.68 | 0.14 | 0.67 | 0.24 ± 0.02 | ... | ... | ... | 0.19 ± 0.03 | 0.62 |
| " E | 0.122 ± 0.009 | 0.073 | 0.009 | 0.057 | 0.118 ± 0.013 | ... | ... | ... | ... | 0.10 |
| " F | 0.123 ± 0.013 | 0.12 | 0.012 | 0.071 | 0.40 ± 0.03 | ... | ... | ... | ... | 0.20 |
| " G (Mkn 1090) | 0.83 ± 0.05 | 0.81 | 0.16 | 0.77 | 0.51 ± 0.03 | ... | ... | ... | 0.30 ± 0.04 | 0.49 |
| " H | 0.011 ± 0.004 | ... | ... | ... | 0.004 ± 0.001 | ... | ... | ... | ... | 0.008 |
| Mkn 1087 | ... | 12.1 | 3.27 | 11.8 | 5.6 ± 0.4 | 10.3 ± 1.1 | 4.6 ± 1.3 | 8.8 ± 1.0 | 4.5 ± 0.2 | 6.3 |
| " N | ... | ... | 0.076 | 0.39 | 0.180 ± 0.015 | ... | ... | ... | ... | 0.12 |
| Haro 15 | 6.8 ± 0.4 | 4.6 | 1.00 | 4.1 | 3.3 ± 0.4 | 2.8 ± 0.3 | 3.2 ± 0.9 | 2.4 ± 0.2 | 4.0 ± 0.2 | 3.6 |
| Mkn 1199 | ... | 3.7 | 0.84 | 3.5 | 3.9 ± 0.6 | 5.2 ± 0.3 | 3.0 ± 0.3 | 4.7 ± 0.2 | 3.16 ± 0.10 | 3.7 |
| " NE | ... | 0.22 | 0.048 | 0.26 | 0.07 ± 0.02 | ... | ... | ... | ... | 0.05 |
| Mkn 5 | 0.0222 ± 0.0014 | 0.050 | 0.008 | 0.049 | 0.046 ± 0.011 | <0.014 | <0.03 | 0.067 ± 0.008 | <0.10 | 0.040 |
| IRAS 08208+2816 | 13.1 ± 0.8 | 6.4 | 1.48 | 5.8 | 11.3 ± 0.9 | 11.4 ± 1.0 | <1.68 | 9.7 ± 0.8 | 16.4 ± 0.7 | 11.6 |
| IRAS 08339+6517 | 6.4 ± 0.4 | 8.2 | 1.92 | 7.3 | 9.5 ± 0.5 | 8.93 ± 0.08 | 5.6 ± 0.6 | 8.36 ± 0.06 | 6.2 ± 0.9 | 7.0 |
| " Comp | 0.095 ± 0.008 | 0.37 | 0.087 | 0.44 | 0.17 ± 0.02 | ... | ... | ... | ... | 0.10 |
| POX 4 | 0.57 ± 0.03 | 0.93 | 0.15 | 0.72 | 1.85 ± 0.06 | 0.31 ± 0.02 | <7.48 | 0.31 ± 0.03 | 0.26 ± 0.03 | 0.54 |
| " Comp | 0.054 ± 0.006 | 0.030 | 0.0063 | 0.041 | 0.012 ± 0.004 | ... | ... | ... | ... | 0.031 |
| UM 420 | 2.01 ± 0.11 | 1.9 | 0.30 | 1.4 | 3.7 ± 0.2 | 6.4 | ... | 5.4 | 1.9 ± 0.8 | 2.1 |
| SBS 0926+606 | 3.4 ± 0.3 | 0.50 | 0.08 | 0.40 | 0.94 ± 0.06 | 0.26 ± 0.03 | <0.86 | 0.20 ± 0.03 | 0.25 ± 0.06 | 0.95 |
| " A | 0.53 ± 0.03 | 0.28 | 0.04 | 0.20 | 0.75 ± 0.04 | ... | ... | ... | ... | 0.52 |
| " B | 2.82 ± 0.25 | 0.25 | 0.04 | 0.22 | 0.19 ± 0.02 | ... | ... | ... | ... | 1.4? |
| SBS 0948+532 | ... | 1.1 | 0.11 | 0.53 | 6.2 ± 0.2 | ... | ... | ... | <0.95 | 4.2 |
| SBS 1054+365 | 0.0073 ± 0.0005 | 0.013 | 0.0014 | 0.019 | 0.036 ± 0.001 | 0.016 | <0.01 | 0.015 | 0.025 ± 0.004 | 0.018 |
| SBS 1211+540 | 0.0062 ± 0.0004 | 0.009 | 0.0007 | 0.009 | 0.011 ± 0.001 | ... | ... | ... | <0.01 | 0.007 |
| SBS 1319+579 | 0.069 ± 0.004 | 0.59 | 0.12 | 0.58 | 0.189 ± 0.012 | 0.24 | ... | 0.17 | <0.07 | 0.15 |
| SBS 1415+437 | 0.0331 ± 0.0018 | 0.022 | 0.0029 | 0.020 | 0.039 ± 0.002 | ... | ... | ... | <0.01 | 0.030 |
| III Zw 107 | ... | 2.3 | 0.51 | 2.2 | 3.19 ± 0.15 | 2.3 ± 0.4 | <2.24 | 2.0 ± 0.3 | 1.52 ± 0.09 | 2.0 |
| Tol 9 | 0.77 ± 0.06 | 1.0 | 0.23 | 1.1 | 1.82 ± 0.13 | 1.59 ± 0.07 | 0.8 ± 0.2 | 1.19 ± 0.08 | 2.18 ± 0.04 | 1.3 |
| Tol 1457-262 | 3.2 ± 0.2 | 2.6 | 0.53 | 2.3 | 5.0 ± 0.3 | 3.7 ± 0.3 | <1.99 | 3.4 ± 0.2 | 5.4 ± 0.3 | 3.8 |
| " Obj 1 | 2.37 ± 0.13 | 1.8 | 0.35 | 1.6 | 3.7 ± 0.2 | ... | ... | ... | ... | 2.4 |
| " Obj 2 | 0.74 ± 0.09 | 0.87 | 0.17 | 0.83 | 1.37 ± 0.06 | ... | ... | ... | ... | 0.83 |
| " #15 | 0.089 ± 0.017 | 0.09 | 0.018 | 0.10 | 0.038 ± 0.003 | ... | ... | ... | ... | 0.06 |
| Arp 252 | 3.84 ± 0.26 | 5.3 | 1.26 | 5.0 | 7.2 ± 0.5 | 16.2 ± 0.9 | 11.6 ± 1.4 | 15.4 ± 0.8 | 49.2 ± 1.5 | 10 |
| " ESO 566-8 | 3.12 ± 0.22 | 4.5 | 1.01 | 4.1 | 6.7 ± 0.5 | ... | ... | ... | ... | 3.8 |
| " ESO 566-7 | 0.72 ± 0.04 | 1.0 | 0.25 | 1.1 | 0.50 ± 0.04 | ... | ... | ... | ... | 0.53 |
| NGC 5253 | 0.190 ± 0.010 | 0.36 | 0.07 | 0.35 | 0.348 ± 0.017 | 0.12 | 0.15 | 0.11 | 0.037 ± 0.002 | 0.14 |

References. S07 = Salim et al. (2007); G84 = Gallagher et al. (1984); K98 = Kennicutt (1998); R01 = Roussel et al. (2001); C92 = Condon (1992); C02 = Condon et al. (2002) using the expression for $M > 5 M_{\odot}$.

from other calibrators, noting its luminous blue compact galaxy (LCBG) nature (López-Sánchez et al. 2004b).

We used our data to establish a new relation between the SFR and the B -luminosity, which should only be applied in starburst galaxies and just as a first estimation of the actual SFR. The left panel of Fig. 4 shows the relation between L_B (in solar units) and the assumed SFR for all our galaxies. Despite some clear discrepancies between some galaxies that show very different SFR for a similar B -luminosity (for example, just compare members G and F of HCG 31), we see a good agreement, having galaxies with higher B -luminosities higher star-formation activity. The discrepancies are a consequence of the different star-formation histories of the galaxies (relative contribution and age of the underlying stellar population, metallicity, age of the most recent star-formation event). A linear fit to our data provides the relation

$$SFR_{B, \text{starbursts}} = 1.148 \times 10^{-9} L_B^{0.906}, \quad (14)$$

where L_B is expressed in units of L_{\odot} . The correlation coefficient of this fit is $r = 0.932$. The third column in Table 5 compiles the SFR_B computed for each galaxy using this equation. The

relation obtained by Gallagher et al. (1984) gives values one order of magnitude lower than those we obtained with our new calibration.

We also computed a relation between the SFR and the U -luminosity for our sample galaxies. The right panel of Fig. 4 shows such a relation. A linear fit to the data yields

$$SFR_{U, \text{starbursts}} = 7.59 \times 10^{-10} L_U^{0.907}, \quad (15)$$

with L_U expressed in units of L_{\odot} . This fit has somewhat smaller scatter than our derived $SFR-L_B$ relation, resulting in a correlation coefficient $r = 0.965$. However, the slope for both calibrations (0.894 ± 0.070 and 0.900 ± 0.054 for $SFR-L_B$ and $SFR-L_U$, respectively) are similar. We notice that Eqs. (14) and (15) cannot be applied to galaxies with no strong star-formation activity, because the SFR value derived from them will be overestimated (as happens in Mkn 1199 NE or IRAS 08339+6517 comp).

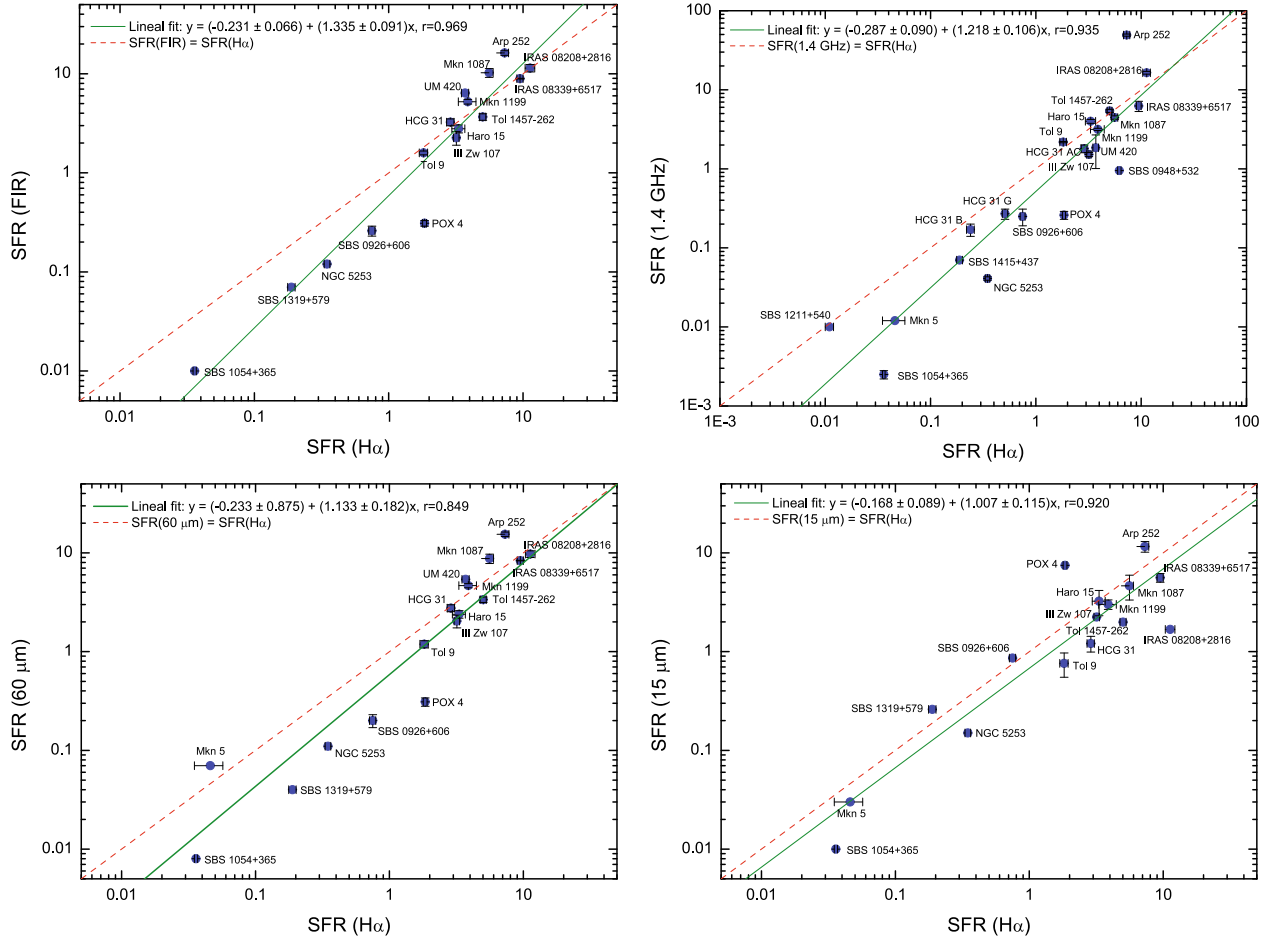


Fig. 2. Comparison between the $H\alpha$ -based SFR – corrected for both extinction and [N II] contribution and assuming Kennicutt (1998), x -axis – with the SFRs derived using the FIR, 15 μm , 60 μm , and 1.4 GHz luminosities. The dotted red lines indicate the position with equal SFR, the continuous green lines show a lineal fit to the data.

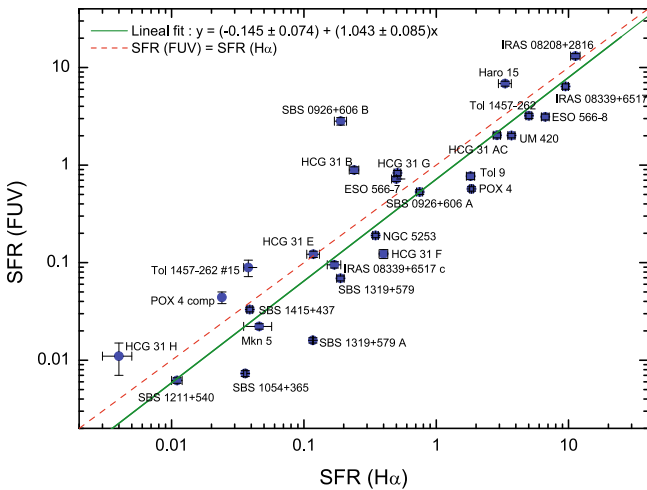


Fig. 3. Comparison between the $H\alpha$ -based SFR – corrected for both extinction and [N II] contribution and assuming Kennicutt (1998), x -axis – with the SFRs derived using the FUV luminosities. The dotted red line indicates the position with equal SFR, while the continuous green line shows a fit to the data.

3.2. Comparison of SFR and metallicity

The left panel of Fig. 5 compares the assumed SFR with the oxygen abundance computed for each galaxy. We estimated the

average SFR values in the low ($12 + \log(O/H) < 7.8$), intermediate ($7.8 < 12 + \log(O/H) < 8.3$), and high ($12 + \log(O/H) > 8.3$) metallicity regimes. As we see, the dispersion in the intermediate-metallicity range is quite high, but that is just the consequence of the star-formation history of each particular galaxy (see Paper IV), because both very dwarf objects (i.e., Mkn 5, SBS 1054+365) and large and bright star-forming galaxies (i.e., Tol 1456-262, III Zw 107) lie in this metallicity regime, and they share a relatively similar chemical history. Besides the large dispersion in the intermediate-metallicity regime, it is clear that galaxies with higher metallicity have higher global SFRs. That is a consequence of the building of the galaxies, because more massive objects are more metal-rich than less massive galaxies (see below), so that when the starburst is initiated, galaxies with higher mass (and with higher metallicities) will create stars at a higher rate than those found in smaller objects. The comparison of the SFR per B -luminosity, SFR/L_B with the metallicity (Fig. 5, right) also shows a tremendous dispersion for $12 + \log(O/H)$ between 8.0 and 8.2. However, we observe that SFR/L_B decreases with increasing oxygen abundance indicating that galaxies with lower metallicity (therefore, less massive objects) have stronger burst of star-formation than those found in higher metallicity (more massive) objects. SBS 0948+532 has the highest SFR/L_B in our sample, indicating the strength of the starburst, as we saw when we analyzed its photometric properties (see Sect. 3.11 in Paper I). On the other hand, SBS 1319+579 has low SFR/L_B than BCDGs with similar characteristics, indicating

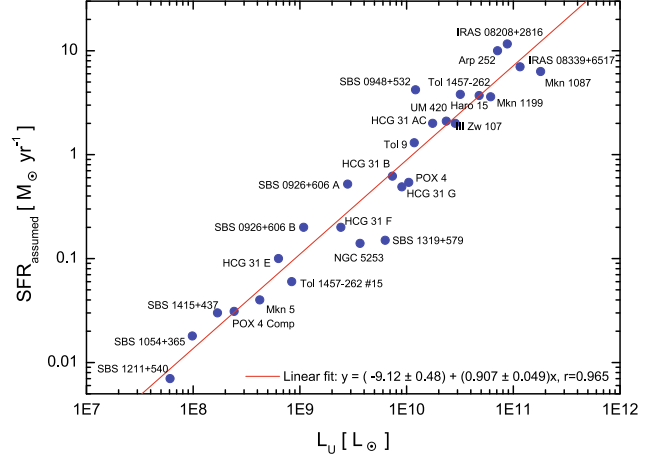
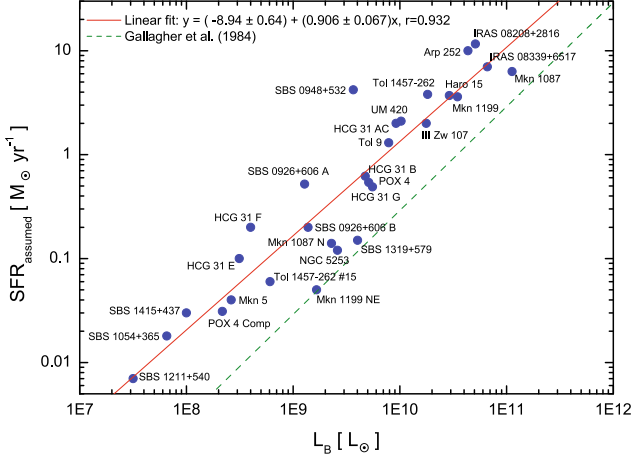


Fig. 4. Assumed SFR vs. B -luminosity (*left panel*) and U -luminosity (*right panel*) for the analyzed galaxies. Luminosities are plotted in solar units. The best fit (in logarithm scale) to our data is plotted with a continuous red line. The previous calibration given by Gallagher et al. (1984) between the SFR and the B -luminosity is shown by a discontinuous green line.

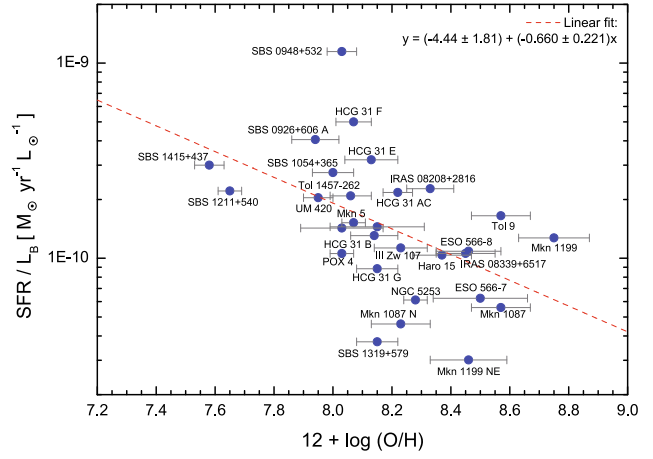
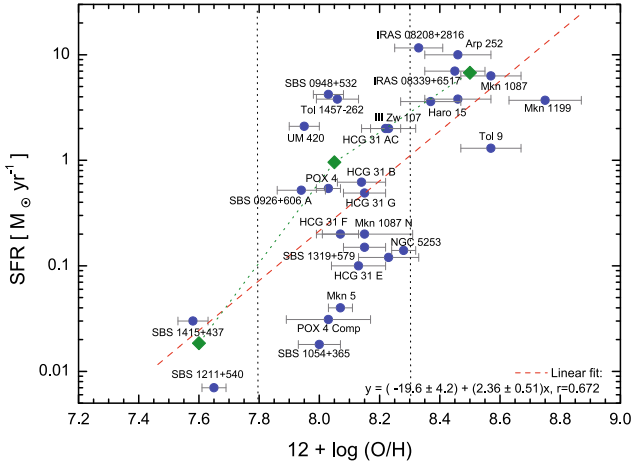


Fig. 5. SFR vs. $12 + \log(\text{O}/\text{H})$ (*left*) and SFR/L_B vs. $12 + \log(\text{O}/\text{H})$ (*right*) for our sample of WR galaxies. The red-dotted line indicates a fit to our data. Green diamonds in the *left panel* plot the average value obtained in the low, intermediate, and high-metallicity regimes.

the peculiarity of this galaxy. We see below that other properties of SBS 1319+579 show additional discrepancies with the average behavior in BCDGs, suggesting that the star-formation activity has been somewhat suppressed in this object. For example, the gas depletion timescale is extremely long for a starburst galaxy, ($\tau \sim 12.7$ Gyr, see Table 6).

3.3. An L_X -SFR relation for starburst galaxies

Although several relations between the X-ray luminosity and the SFR have been proposed (i.e., Ranalli et al. 2003; Lou & Bian 2005) they do not seem to be appropriate for young starbursting systems. For example, as we explained in the analysis of the LCBG IRAS 08339+6517 (López-Sánchez et al. 2006), the relation provided by Ranalli et al. (2003) gives a higher SFR value ($61.8 M_\odot \text{yr}^{-1}$) than the estimations obtained using other frequencies ($6\text{--}8 M_\odot \text{yr}^{-1}$). Stevens & Strickland (1998a) show that the X-ray luminosities in WR galaxies are substantially higher than those found in non-WR galaxies with similar B -luminosity. That is a consequence of the higher rate of superbubbles and supernova explosions in WR galaxies.

We used the sample of WR galaxies analyzed by Stevens & Strickland (1998a,b) to get a tentative calibration between SFR and L_X for this kind of object. These authors obtained X-ray data in the $0.2\text{--}2.0$ keV range using the satellite ROSAT. We checked which of these galaxies also possess FIR data from the IRAS satellite, and established a relation between L_{FIR} and L_X , as shown in Fig. 6. Only 18 galaxies have available data for both luminosities. NGC 5253 was included in the Stevens & Strickland (1998a,b) analysis, but they indicate that the X-ray emission in this object is very peculiar. The X-ray emission measured in NGC 5408 may be unrelated to the galaxy. Neglecting the contribution of these two galaxies, the linear fit to the data thus gives

$$L_{\text{FIR}} = 24 \times L_X^{1.04}, \quad (16)$$

where the correlation coefficient $r = 0.929$. Considering the calibration given by Kennicutt (1998) between L_{FIR} and SFR (Eq. (6)), we find the following calibration between soft X-rays ($0.2\text{--}2.0$ keV) and SFR:

$$\text{SFR}_X = 1.08 \times 10^{-42} L_X^{1.04}. \quad (17)$$

As seen in Fig. 6, our new $\text{SFR}\text{--}L_X$ calibration agrees better with the observational data than the relations explained before.

Table 6. Additional FIR and radio properties.

| Galaxy | q^a | $\log R^b$ | τ_g [Gyr] |
|-----------------|-------|------------|-------------------|
| HCG 31 AC | 2.39 | 1.19 | 1.92 |
| HCG 31 B | ... | 1.25 | 5.3 |
| HCG 31 F | ... | ... | 2.9 |
| HCG 31 G | ... | 1.11 | 2.3 |
| Mkn 1087 | 2.53 | 1.30 | 3.3 |
| Haro 15 | 2.01 | 1.48 | 1.9 |
| Mkn 1199 | 2.39 | 1.31 | 0.40 |
| Mkn 5 | ... | ... | 2.1 |
| IRAS 08208+2816 | 2.01 | 1.57 | ... |
| IRAS 08339+6517 | 2.33 | 1.21 | 0.89 |
| POX 4 | 2.25 | 0.93 | 4.2 |
| UM 420 | 2.71 | 1.08 | ... |
| SBS 0926+606 | 2.18 | 0.79 | 2.0 (A), 5.6 (B) |
| SBS 0948+532 | ... | ... | ... |
| SBS 1054+365 | 2.79 | -0.10 | 4.0 |
| SBS 1211+540 | ... | ... | 3.5 |
| SBS 1319+579 | 2.15 | ... | 12.7 |
| SBS 1415+437 | ... | ... | 3.5 |
| III Zw 107 | 2.34 | 1.06 | 3.5 |
| Tol 9 | 2.03 | 1.16 | 1.95 |
| Tol 1457-262 | 2.00 | 1.43 | 1.51 |
| Arp 252 | 1.69 | 2.28 | ... |
| NGC 5253 | 2.62 | 0.33 | 0.97 |

Notes. ^(a) The logarithmic ratio of FIR to radio flux density parameter, q , is defined in Eq. (20).

^(b) R is the nonthermal to thermal ratio, derived from the 1.4 GHz and $H\alpha$ fluxes.

^(c) The gas depletion timescale is defined as $\tau_g = 1.32M_{\text{HI}}/\text{SFR}$ (Skillman et al. 2003).

Indeed, the Lou & Bian (2005) relation gives values around one order of magnitude lower than those expected from the FIR luminosity, but Ranalli et al. (2003) calibration provides values almost one order of magnitude higher than the actual ones. Using our new relation and the available X-ray data for our WR galaxies (see Table 3), we derive an SFR_X of 3.5, 13.8, and $0.86 M_{\odot} \text{ yr}^{-1}$ for HCG 31, IRAS 08339+6517, and Tol 9, respectively. These values agree well with the actual SFR estimated for each object (see Table 5).

4. FIR/radio correlation

We used the luminosity data shown in Table 4 to check that our WR galaxies follow the FIR/radio correlation. As shown by Condon et al. (1992), the FIR/radio correlation is much tighter for starbursts than for active galaxies. Figure 7 (left) plots the 1.4 GHz luminosity vs. the $60 \mu\text{m}$ luminosity for our sample galaxies and the relation between both quantities found by Yun et al. (2001),

$$L_{1.4\text{GHz}} [\text{W Hz}^{-1}] = 10^{12} L_{60 \mu\text{m}} [L_{\odot}], \quad (18)$$

while Fig. 7 (right) shows $L_{1.4\text{GHz}}$ vs. the total FIR luminosity and the relation given by Condon et al. (1991),

$$\log L_{1.49\text{GHz}} [\text{W Hz}^{-1}] = 1.1 \log L_{\text{FIR}} [L_{\odot}] + 10.45. \quad (19)$$

Bell (2003) pointed out that the radio-FIR correlation is linear not because both radio and FIR emission track SFR, but rather because they fail to track SFR in independent, but coincidentally quite similar, ways. Further analysis (i.e., Hunt et al. 2005) also found that this relation does not hold for some low-metallicity

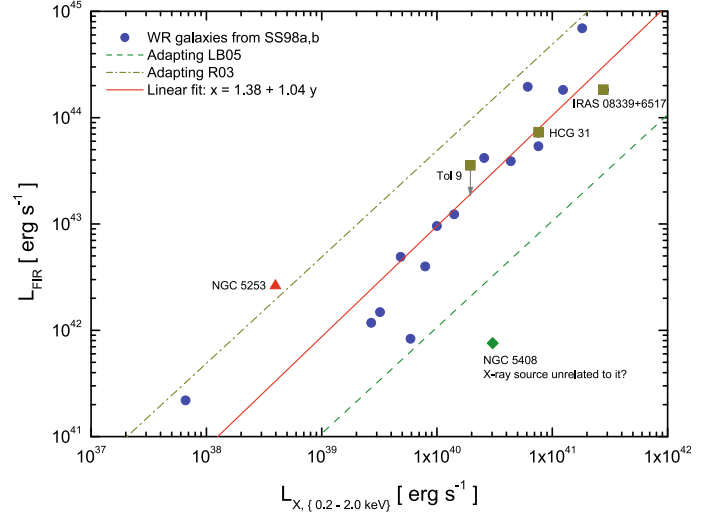


Fig. 6. X-ray luminosity in the 0.2–2.0 keV range vs. FIR luminosity for the sample of WR galaxies analyzed by Stevens & Strickland (1998a,b). The red continuous line is the best fit to the data, excluding the values for NGC 5253 and NGC 5408. The green discontinuous line is the relation obtained using the SFR- L_X calibration provided by Lou & Bian (2005), while the yellow dotted-dashed line is the relation obtained from the Ranalli et al. (2003) calibration. The three additional WR galaxies of our sample for which X-ray data are available (HCG 31, IRAS 08339+6517, and Tol 9) are indicated with dark yellow squares.

or young starbursts galaxies. However, as seen in Fig. 7, all analyzed objects except Mkn 5 (which has a very uncertain value for FIR) and Arp 252 (ESO 566-8 hosts some kind of nuclear activity) follow both relations. This indicates that the galaxies are starbursting systems and are not active galaxies (Seyfert or AGNs). We already reached this conclusion when we analyzed the diagnostic diagrams involving several emission-line ratios (see Paper III). Figure 7 includes a linear fit (in logarithmic scale) to our data (neglecting Mkn 5, for which the FIR values have high uncertainties). The relation given by Condon et al. (1991) seems to be slightly displaced with respect our observational data, although we also see some small discrepancies in the Yun et al. (2001) relation for the faintest objects.

The non-AGN nature of our sample of WR galaxies is also supported by the analysis of the q parameter and the FIR spectral index. The q parameter is defined as the logarithmic ratio of FIR to radio flux density,

$$q \equiv \log \frac{F_{\text{FIR}} (\text{W m}^{-2}) / 3.75 \times 10^{12} \text{ Hz}}{S_{1.4 \text{ GHz}} (\text{W m}^{-2} \text{ Hz}^{-1})}, \quad (20)$$

and it is very robust for most galaxy populations: $\langle q \rangle = 2.34 \pm 0.19$ (Condon et al. 1991; Yun et al. 2001). Galaxies with $q < 1.8$ are more than 3 times more radio loud than the mean for the star-forming galaxies, so they can be classified as AGN-powered. As seen in Table 6, all galaxies except Arp 252 have a q value similar to that expected for starburst galaxies.

Table 6 also compiles the nonthermal to thermal ratio R of the galaxies with available 1.4 GHz radio-continuum data. The thermal flux at 1.4 GHz was computed by applying Eq. (5). The majority of the galaxies show the typical value for star-forming galaxies, $\log R = 1.3 \pm 0.4$ Dopita et al. (2002). The low value in R found in POX 4 and NGC 5253 may be because the $H\alpha$ flux has been overestimated, although the situation of NGC 5253 is far from clear (López-Sánchez et al. 2010a). The value obtained for SBS 1054+365 is unreliable, we consider that it or the 1.4 GHz flux was underestimated (very probably) or

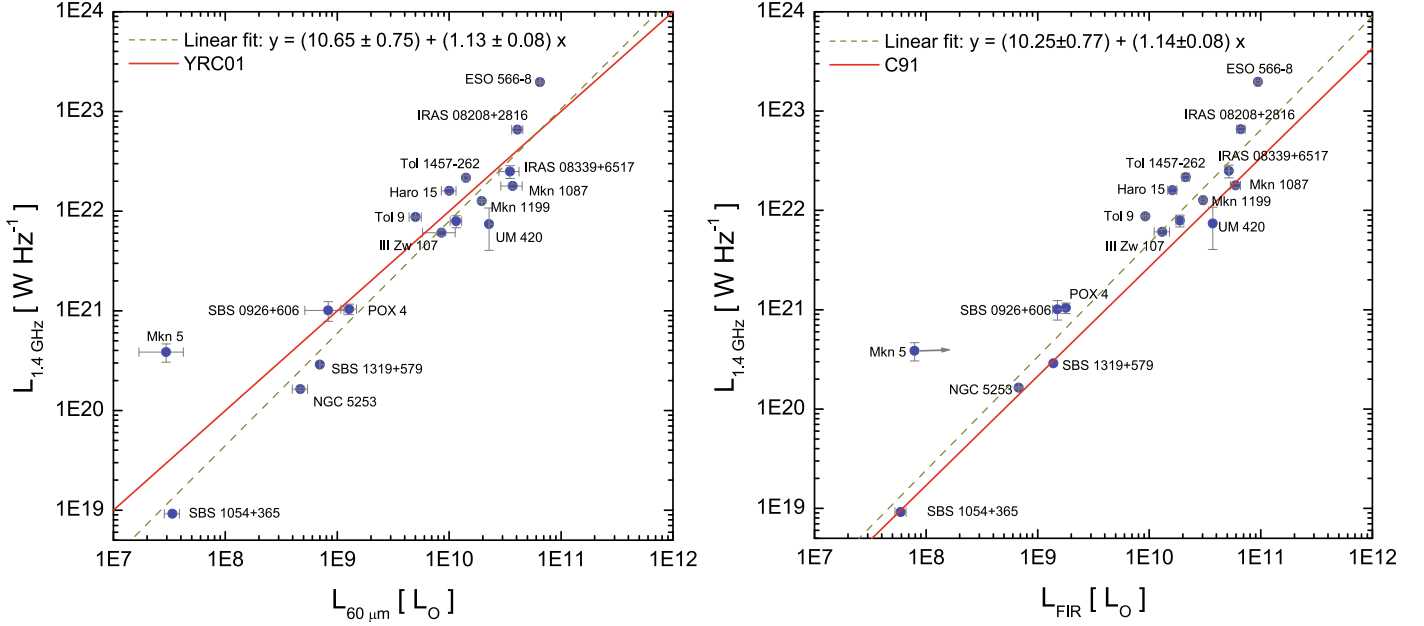


Fig. 7. 1.4 GHz radio-continuum luminosity vs. the 60 μm luminosity (*left*) and the FIR luminosity (*right*). The relations derived by Yun et al. (2001) (Eq. (18), left diagram) and Condon et al. (1991) (Eq. (19), right diagram) are plotted with a red continuous line. The best linear fits to our data (in logarithmic units) are shown with a yellow dashed line.

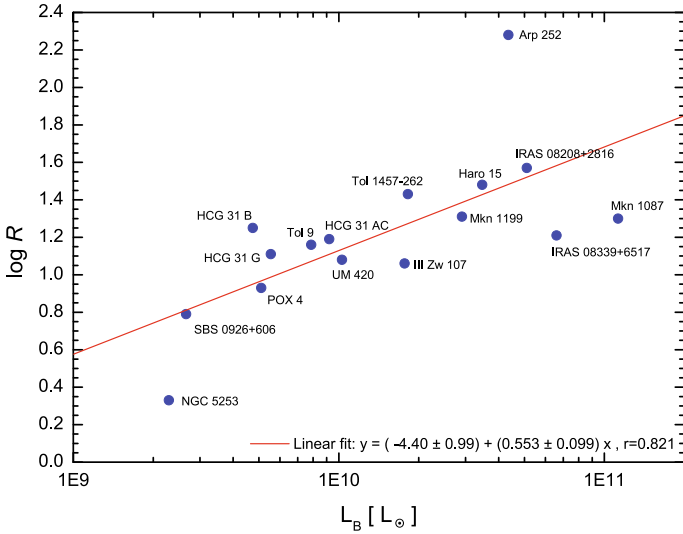


Fig. 8. Comparison of the B -luminosity (in solar units) and the logarithmic nonthermal to thermal ratio, $\log R$, for our sample galaxies. A linear fit is shown with a continuous red line.

that the $H\alpha$ flux was overestimated. However, the high value found in Arp 252 (the emission comes mainly from ESO 566-8), $\log R = 2.28$, is real and indicates that the thermal flux at 1.4 GHz is less than 0.5%. As reported by several authors (i.e., Klein et al. 1984, 1991; Bell 2003), dwarf galaxies seem to have a lower nonthermal-to-thermal emission ratio than normal spiral galaxies. The values obtained for the R parameter in our galaxy sample tend to be lower at lower B -luminosities, as shown in Fig. 8. The difference between dwarf and larger galaxies is often interpreted as the higher efficiency of cosmic-ray confinement in more massive galaxies (e.g., Klein et al. 1984; Price & Duric 1992; Niklas et al. 1997; Bell 2003).

5. Analysis of the masses

For this work, we estimated the ionized gas mass M_{HII} , using the $H\alpha$ images presented in Paper I; neutral gas mass M_{HI} , using HI data at 21 cm compiled from the literature; mass of the ionizing star cluster M_{\star} , using $H\alpha$ and $W(H\beta)$, see Paper I; warm dust mass M_{dust} , using the FIR fluxes; Keplerian mass M_{Kep} , via the kinematics of the ionized gas; and dynamical mass M_{dyn} , using the HI kinematics. All these data are compiled in Table 7. The value of M_{dust} compiled in this table is for the entire system: all galaxies in the HCG 31 group, members A and B in SBS 0926+606, all galaxies in Tol 1457-262, and ESO 566-8 and ESO 566-7 in Arp 252. We neglect the contribution of the FIR emission in dwarf objects associated to larger galaxies (companion objects surrounding Mkn 1087, Mkn 1199, IRAS 08339+6519, and POX 4). The estimation of M_{Kep} and M_{dyn} for each galaxy was explained in Paper II. We just remember that, as the extension of the neutral gas is usually larger than the stellar component, our estimations of M_{dyn} are very probably underestimated. Furthermore, nonrotational movements would yield an overestimation of the total mass. Only interferometric HI analysis can definitely provide a more precise determination of the dynamical mass for each system. However, we may use our M_{dyn} values as a rough estimation of the total mass of the galaxies. Their comparison with M_{Kep} , M_{HI} , M_{HII} , M_{dust} , and their associated mass-to-light ratios will give clues to the galaxy type, dynamics and the fate of the neutral gas.

We first compared all mass determinations with the optical luminosity of the galaxies. Figure 9 shows the relations between M_{HII} , M_{HI} , M_{dust} , and M_{\star} with the absolute B -magnitude. As we should expect, besides some scatter, all mass determinations clearly increase with increasing optical luminosity. We performed a linear fit to the data, and the results are

$$\log M_{\text{HII}} = (-0.21 \pm 0.56) - (0.342 \pm 0.030)M_B, \quad (21)$$

$$\log M_{\text{HI}} = (3.69 \pm 0.52) - (0.292 \pm 0.028)M_B, \quad (22)$$

$$\log M_{\text{dust}} = (-1.15 \pm 0.92) - (0.364 \pm 0.047)M_B, \quad (23)$$

$$\log M_{\star} = (-0.47 \pm 0.54) - (0.397 \pm 0.029)M_B, \quad (24)$$

Table 7. Keplerian mass (M_{Kep}), dynamical mass (M_{dyn}), neutral gas mass (M_{HI}), ionized gas mass (M_{HII}), warm dust mass (M_{dust}), mass of the ionizing star cluster (M_{\star}), total stellar mass (M_{stars}), and baryonic mass (M_{bar}) of the galaxies analyzed in this work.

| Galaxy | M_{Kep} [$10^8 M_{\odot}$] | M_{dyn} [$10^8 M_{\odot}$] | M_{HI} [$10^8 M_{\odot}$] | M_{HII} [$10^6 M_{\odot}$] | M_{dust} [$10^6 M_{\odot}$] | M_{\star} [$10^6 M_{\odot}$] | M_{stars} [$10^8 M_{\odot}$] | M_{bar} [$10^8 M_{\odot}$] |
|-----------------|------------------------------------------|------------------------------------------|-----------------------------------------|------------------------------------------|-------------------------------------------|-------------------------------------|--------------------------------------------|------------------------------------------|
| HCG 31 | ... | ... | 74.6 | 7.8 ± 0.5 | 2.56 | 37.8 ± 2.8 | 33.8 | 141 |
| " AC | 340 | 850 | 36.4 | 5.4 ± 0.3 | ... | 18.2 ± 1.2 | 14.4 | 62.5 |
| " B | 26 | 54 | 19.4 | 0.45 ± 0.04 | ... | 8.2 ± 0.7 | 8.0 | 33.6 |
| " E | ... | 13^a | ... | 0.22 ± 0.02 | ... | 2.6 ± 0.3 | 0.47 | ... |
| " F | 3.0 | 15 | 6.13 | 0.75 ± 0.04 | ... | 0.40 ± 0.03 | 0.39 | 8.5 |
| " G | 21 | 68 | 19.4 | 0.96 ± 0.05 | ... | 7.0 ± 0.4 | 10.5 | 36.1 |
| Mkn 1087 | 560 | 1800 | 156 | 10.4 ± 9.7 | 7.8 | 129 ± 9 | 288 | 494 |
| " N | 2.2 | 45^a | ... | 0.337 ± 0.028 | ... | 3.34 ± 0.28 | 4.0 | ... |
| Haro 15 | 121 | 365 | 55 ± 18 | 6.2 ± 0.7 | 2.1 | 77 ± 9 | 99.2 | 172 |
| Mkn 1199 | 82 | 1650 | 12.2 | 7.3 ± 1.1 | 3.1 | 140 ± 21 | 275 | 291 |
| " NE | 2.9 | 70^a | ... | 0.13 ± 0.03 | ... | 1.7 ± 0.4 | 17.4 | ... |
| Mkn 5 | 21 | 36 | 0.72 ± 0.09 | 0.081 ± 0.010 | 0.099 | 0.300 ± 0.012 | 1.5 | 2.5 |
| IRAS 08208+2816 | 39 | 600^a | ... | 21.1 ± 1.7 | 8.84 | 166 ± 14 | 298 | ... |
| IRAS 08339+6517 | 100 | 370 | 53 ± 6 | 14.5 ± 0.7 | 3.91 | 226 ± 10 | 476 | 546 |
| " Comp | 80 | 100 | 7.0 ± 0.9 | 0.26 ± 0.03 | ... | 4.1 ± 0.5 | 18.6 | 27.9 |
| POX 4 | 5.0 | 76 | 21 | 5.70 ± 0.18 | 0.093 | 9.8 ± 0.3 | 14.3 | 29.1 |
| " Comp | ... | ... | ... | 0.05 | ... | 0.79 ± 0.07 | 0.88 | ... |
| UM 420 | 21 | 200^a | ... | 6.9 ± 0.4 | 5.0^b | 13.8 ± 0.9 | 45.6 | ... |
| SBS 0926+606 | ... | ... | 17.7 ± 7.2 | 1.75 ± 0.10 | 0.37 | 8.4 ± 0.6 | 7.59 | 30.9 |
| " A | ... | 23 | 9.6 ± 3.6 | 1.40 ± 0.07 | ... | 3.59 ± 0.17 | 2.9 | 15.5 |
| " B | ... | 45 | 8.1 ± 3.6 | 0.35 ± 0.03 | ... | 4.8 ± 0.4 | 4.7 | 15.4 |
| SBS 0948+532 | 21 | 90^a | ... | 11.6 ± 0.4 | ... | 18.8 ± 0.7 | 12.6 | ... |
| SBS 1054+365 | 0.78 | 15 | 0.61 ± 0.06 | 0.067 ± 0.003 | 0.012 | 0.23 ± 0.01 | 0.33 | 1.13 |
| SBS 1211+540 | 1.13 | 1.14 | 0.24 ± 0.04 | 0.021 ± 0.001 | ... | 0.05 | 0.102 | 0.420 |
| SBS 1319+579 | 86 | 140 | 16.4 | 0.35 ± 0.02 | 0.30 | 0.78 ± 0.05 | 22.9 | 44.5 |
| SBS 1415+437 | 2.5 | 4.9 | 0.96 ± 0.07 | 0.074 ± 0.003 | ... | 0.14 ± 0.01 | 0.46 | 1.74 |
| III Zw 107 | 8.2 | 180 | 67 ± 12 | 6.0 ± 0.3 | 1.25 | 74 ± 3 | 61.8 | 150 |
| Tol 9 | 12 | 580 | 22 ± 2 | 3.4 ± 0.2 | 2.41 | 27.4 ± 1.9 | 44.4 | 106 |
| Tol 1457-262 | ... | 950 | 47 | 9.4 ± 0.5 | 1.83 | 41 ± 2 | 87.2 | 149 |
| " Obj 1 | 62 | 290^a | ... | 6.9 ± 0.4 | ... | 23.4 ± 1.5 | 46.9 | ... |
| " Obj 2 | ... | 150^a | ... | 2.56 ± 0.12 | ... | 14.4 ± 0.7 | 36.2 | ... |
| Arp 252 | ... | ... | ... | 13.4 ± 0.9 | 6.32 | 82.3 ± 4.9 | 338 | ... |
| " ESO 566-8 | 73 | 440^a | ... | 12.5 ± 0.8 | ... | 45 ± 3 | 250 | ... |
| " ESO 566-7 | 4 | 150^a | ... | 0.93 ± 0.07 | ... | 16.8 ± 1.2 | 88 | ... |
| NGC 5253 | ... | 83 | 1.59 ± 0.09 | 0.65 ± 0.03 | 0.042 | 2.22 ± 0.11 | 11.4 | 13.5 |

Notes. ^(a) Tentative value of M_{dyn} computed using Eqs. (25)–(28) and (29).

^(b) The warm dust mass is very probably overestimated because of the FIR contribution by the foreground galaxy UGC 01809.

with correlation coefficients of 0.899, 0.922, 0.912, and 0.928, respectively. Some deviations to the fits are found in Mkn 1199 (that possesses a relatively low M_{HI}), SBS 0948+532 (with a very high M_{HII}), POX 4 (it seems to be M_{dust} deficient, while its ionized gas mass may be overestimated), UM 420 (its high M_{dust} is very probably a consequence of the contamination of the FIR emission by the foreground galaxy UGC 01809, see Sect. 3.9 in Paper I and Sect. 3.9 in Paper II), SBS 1319+579 and IRAS 08339+6517 Comp (that have very low M_{\star} for their absolute B -magnitude) and NGC 5253 (that is both M_{HI} and M_{dust} deficient).

Figure 10 plots the dynamical mass (which represents the total mass of the galaxy) versus the absolute magnitude in several broad-band filters (B , V , R , and J). We find a clear correlation between these quantities, and a linear fit to the data yields

$$\log M_{\text{dyn}} = (4.37 \pm 0.58) - (0.304 \pm 0.032)M_B, \quad (25)$$

$$\log M_{\text{dyn}} = (4.28 \pm 0.55) - (0.306 \pm 0.030)M_V, \quad (26)$$

$$\log M_{\text{dyn}} = (3.86 \pm 0.57) - (0.324 \pm 0.030)M_R, \quad (27)$$

$$\log M_{\text{dyn}} = (4.60 \pm 0.65) - (0.281 \pm 0.034)M_J, \quad (28)$$

with correlation coefficients r of 0.922, 0.931, 0.940, and 0.907, respectively. Slopes in all fits are quite similar. The most

important deviations to these fits are found in clearly interacting systems (Mkn 1199 and HCG 31 AC) but also in Mkn 5 and SBS 1054+365.

We compared the Keplerian mass (derived from the kinematics of the ionized gas) with the dynamical mass (estimated from the kinematics of the neutral gas). Figure 11 plots both sets of values. As expected, M_{Kep} is lower than M_{dyn} for almost all cases ($M_{\text{Kep}} = M_{\text{dyn}}$ is shown in Fig. 11). Although the dispersion is high – and we remember that M_{Kep} and/or M_{dyn} may be overestimate because of interaction features – we performed a tentative fit to the data, which yields

$$M_{\text{dyn}} = 0.584 \times M_{\text{Kep}}^{1.114}, \quad (29)$$

with a correlation coefficient $r = 0.827$. This relation is included in Fig. 11. As explained in Sect. 3.13 of Paper II, M_{Kep} in SBS 1211+540 has been probably overestimated, so we did not consider this point in the analysis. The relation indicates that M_{Kep} is between 12% (for $M_{\text{dyn}} = 10^{11} M_{\odot}$) and 24% (for $M_{\text{dyn}} = 10^8 M_{\odot}$) of the total dynamical mass. As we should expect, more massive galaxies have a higher $M_{\text{dyn}}/M_{\text{Kep}}$ ratio, indicating that the kinematics of the ionized gas is not appropriate for deriving the total dynamical mass in those objects.

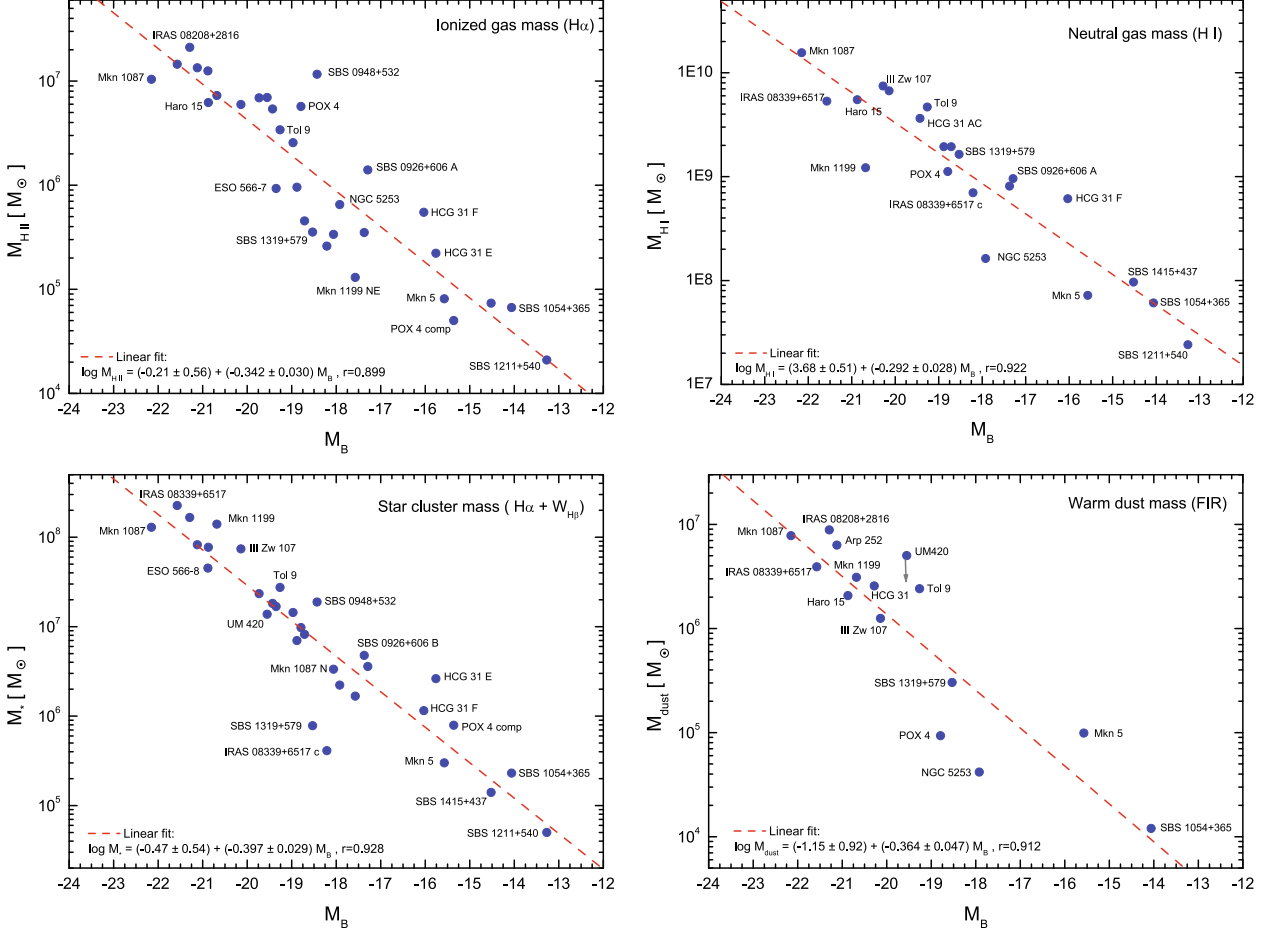


Fig. 9. Ionized gas mass (M_{HII}), neutral gas mass (M_{HI}), mass of the ionizing star cluster (M_*), and warm dust mass (M_{dust}) vs. the absolute B magnitude for the analyzed galaxies. Linear fits to the data are shown with a dashed red line.

Using Eqs. (25)–(28) and 29, we computed a tentative value for the dynamical mass in the galaxies because of lack of HI data. We included the results in Table 7, and plotted these points in Fig. 11. As we can see, they match the positions of the galaxies for which M_{dyn} was derived from HI data, but we will not consider these points in the subsequent analysis.

We prefer to use our *NIR* data to derive a proper value for the stellar mass of all the galaxies. Following the description provided by Kirby et al. (2008), we may assume an H -band mass-to-light ratio of $M_{\text{stars}}/L_H = 0.8$ to compute the stellar mass, M_{stars} , from the H -luminosity (compiled for all objects in Table 4). This assumption is supported by both observations (Bell 2003; Kirby et al. 2008) and theory (de Jong 1996), and it considers a 12 Gyr old solar metallicity stellar population with a constant SFR and Salpeter initial mass function. The H -band mass-to-light ratio may therefore be somewhat overestimated for our young galaxies. Combining the H -band derived stellar mass and the HI mass (we neglect the ionized gas, molecular gas, and dust contributions), the total baryonic mass, M_{bar} , can be computed via

$$M_{\text{bar}} = M_{\text{stars}} + 1.32M_{\text{HI}}, \quad (30)$$

where the factor 1.32 corrects the HI mass for the presence of helium. The derived values for both M_{bar} and M_{stars} are compiled in last columns in Table 7. For SBS 0948+532 and SBS 1211+540, which lack *NIR* colors, we assumed that $V - J \sim 0.8$ and $J - H \sim 0.3$ to derive the H -band luminosity.

As we should expect, the comparison between the dynamical and the baryonic masses (Fig. 12) indicates that M_{dyn} is

always higher than M_{bar} , except for IRAS 08339+6517, which has expelled a considerable fraction of its neutral gas to the intergalactic medium and shows disturbed HI kinematics (Cannon et al. 2004) with a long tidal stream that makes it impossible to get a good estimation of M_{dyn} (López-Sánchez et al. 2006). Besides the uncertainties in M_{dyn} , this indicates the presence of dark matter in all systems. The dark matter contribution would be even higher if, as we said, our values of M_{dyn} are underestimated because of the uncertainty in the extension of the HI disk. In all cases, except in those galaxies for which interferometric data were available, we used the maximum of the radius of the optical extent to compute M_{dyn} . Figure 12 indicates the position of $M_{\text{dyn}} = M_{\text{bar}}$ if M_{dyn} is computed assuming that the extension of the neutral gas is 2.5 times the size of the optical extent. Indeed, only interferometric HI maps and a detailed analysis of the rotation of the neutral gas (de Blok et al. 2008; Westmeier et al. 2010) can better estimate of the dynamical masses of galaxies. This issue is even more important if interactions are disturbing the rotation pattern of the HI gas. A clear example of this is Tol 9 within the Klemola 13 group. Our interferometric HI map (López-Sánchez et al. 2008b, 2010b) shows that the neutral gas cloud in which this BCG is embedded includes not only Tol 9 but also some nearby dwarf galaxies. Indeed, this HI cloud seems to rotate as a single entity, and shows a long tidal tail in the direction of other galaxies in the group. However, the maximum of the HI emission is located exactly at Tol 9.

The important aspect to emphasize here is that, besides the unknown amount of dark matter, strongly interacting systems,

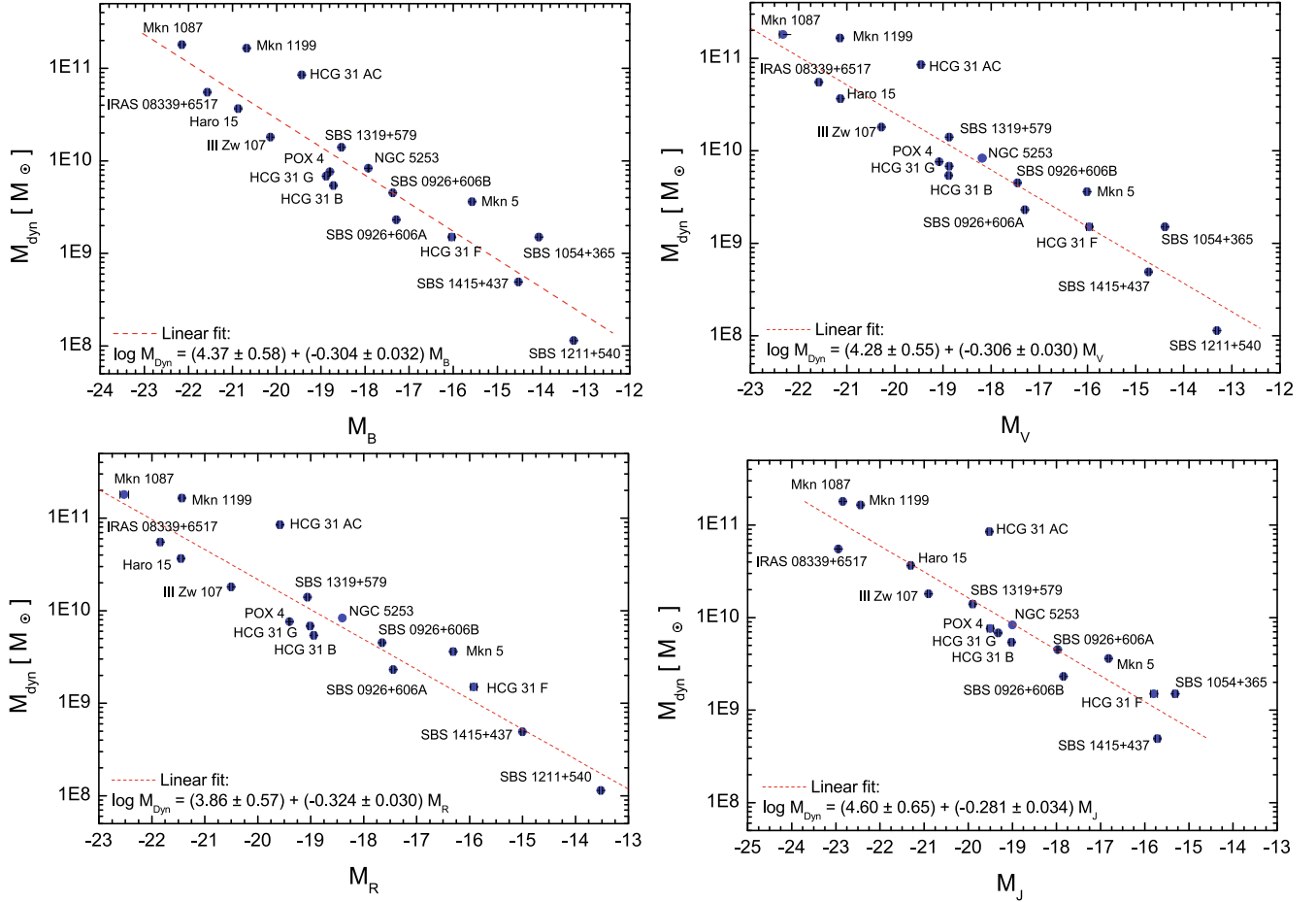


Fig. 10. Dynamical mass (M_{dyn}) vs. absolute B , V , R and J magnitudes for the galaxies analyzed in this work. A linear fit is shown with a dashed red line.

such as HCG 31 AC or Tol 1457-262, lie outside the observed main trend, because they have dynamical masses that are almost 14 and 7 times their baryonic masses. Mkn 1087, Mkn 1199, and Tol 9, which are in clear interaction with nearby objects, also have higher M_{dyn} than expected. Consequently, SBS 1054+365 and Mkn 5, which clearly have dynamical masses that are more than one order of magnitude higher than those expected for dwarf galaxies with $M_{\text{bar}} \sim 10^8 M_{\odot}$, may also have highly perturbed HI kinematics. The same situation may be happening in NGC 5253, which has a dynamical mass that is almost an order of magnitude higher than expected for a galaxy with $M_{\text{bar}} \sim 10^9 M_{\odot}$.

6. Mass-metallicity relations

Our data set allows investigating the mass-metallicity ($M-Z$) relation of star-forming galaxies. The relationship between metallicity and stellar mass provides important clues to galaxy formation and evolution; however, the luminosity is commonly used instead of the mass to analyze such correlations (i.e., Paper IV and references within). Observationally, the $M-Z$ relation arises because low-mass galaxies have higher gas fractions than higher mass galaxies (i.e., Boselli et al. 2001; Kewley & Ellison 2008). Theoretically, the mean stellar metallicity of the galaxies increases with age as a consequence of the chemical enrichment of the ISM, while the stellar mass increases with time as galaxies undergo merging processes (e.g., Somerville & Primack 1999; Calura et al. 2004). Once the NIR luminosities or the

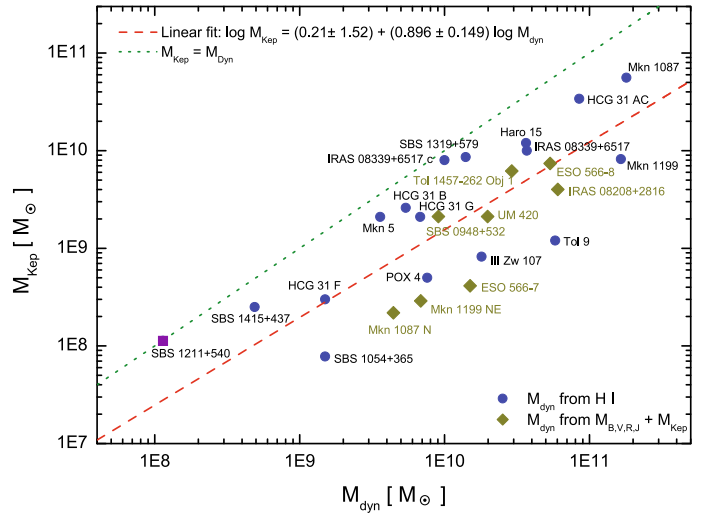


Fig. 11. Keplerian mass (M_{Kepl}) vs. dynamical mass (M_{dyn}) for the galaxies studied in this work. Blue circles plot galaxies with a direct estimation of M_{dyn} using the HI data, while the dark yellow diamonds indicate when M_{dyn} was derived using Eqs. (25)–(28) and (29). The dashed red line is a linear fit to the M_{dyn} derived from the HI data excluding SBS 1211+540. The dotted green line indicates $M_{\text{Kepl}} = M_{\text{dyn}}$.

optical- NIR SED are known, M_{stars} can be estimated relatively closely using stellar evolutionary synthesis models, as we explained in the previous section. The main problem with studying

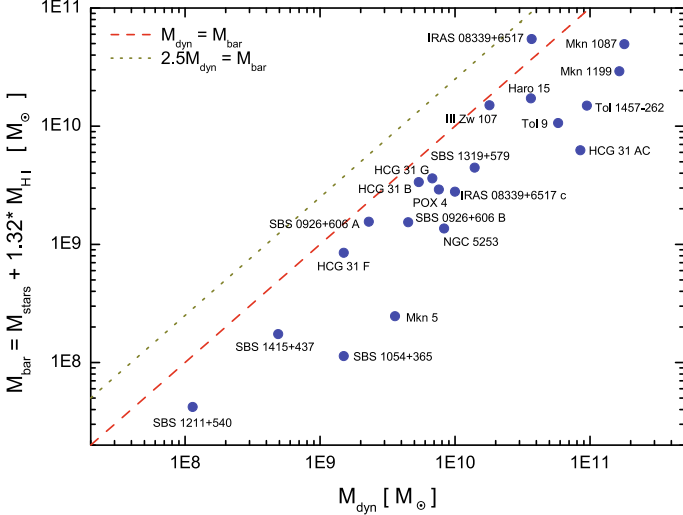


Fig. 12. Comparison between the baryonic mass (M_{bar}) and the dynamical mass (M_{dyn}) for our sample galaxies. The dashed red line indicates $M_{\text{bar}} = M_{\text{dyn}}$, and the dotted yellow line indicates the position of $M_{\text{bar}} = M_{\text{dyn}}$ if M_{dyn} is computed assuming that the HI size of the galaxies is 2.5 their optical extend. Note that strongly interacting systems (HCG 31 AC or Tol 1457-262) lie away from the observed main trend.

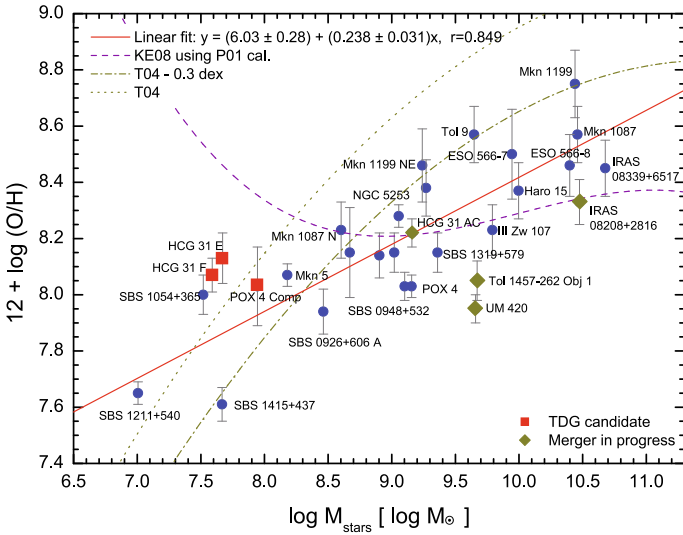


Fig. 13. Relation between M_{stars} and the oxygen abundance for our galaxy sample. A linear fit to the data is shown with a dashed red line. The TDG candidates are plotted with a red square, while galaxies in the process of merging are shown with a yellow diamond. A linear fit to the data without considering these two groups of objects is shown with a continuous red line. Some previous $M_{\text{stars}} - Z$ relations are also plotted: Tremonti et al. (2004) with a yellow dotted line, Tremonti et al. (2004) corrected by a factor of 0.3 dex in oxygen abundance – dotted-dashed yellow line – and the Kewley & Ellison (2008) relation considering the Pilyugin (2001b) empirical calibration to derive the metallicity – dashed pink line. These relations are only valid for $\log M_{\text{stars}} \geq 8.5$.

the $M - Z$ relation lies in all the uncertainties involving determining an accurate oxygen abundance, such as different methods yielding very different results (see Paper IV and Kewley & Ellison 2008). Here, the oxygen abundance of the majority of the galaxies was computed using the direct method, but Pilyugin (2001a) calibration has been applied to computing the metallicity of some few massive objects (Mkn 1087, Haro 15,

IRAS 08339+6517, ESO 566-7, ESO 566-8), as we explained in Paper IV.

Figure 13 shows the relations between the stellar mass and the oxygen abundance, and Fig. 14 shows the relations between the baryonic mass (left panel) and the dynamical mass (right panel) with the oxygen abundance. From Figs. 13 and 14 it is quite evident that a $M - Z$ relation is satisfied for our sample galaxies. Although there is still a considerable dispersion for some objects, the comparison with the luminosity-metallicity relation (see Fig. 17 and Sect. 5 of Paper IV) suggests a closer correlation when using the stellar, baryonic, or the dynamical masses than the absolute optical/NIR magnitudes.

The $M_{\text{stars}} - Z$ diagram (Fig. 13) shows a large dispersion for galaxies with $12 + \log(\text{O}/\text{H}) \sim 8$, as there are dwarf galaxies with $M_{\text{stars}} \sim 4 \times 10^7 M_{\odot}$ (HCG 31 F and E, SBS 1054+365) and large systems with $M_{\text{stars}} \sim 5 \times 10^9 M_{\odot}$ (UM 420, Tol 1457-262 Obj 1) within this metallicity range. The origin of this dispersion is that the low-mass systems are TDG candidates, which have higher oxygen abundance than expected for their mass (not the case of SBS 1054+365), while the high-mass objects are very probably a merger of two independent galaxies (so their oxygen abundance is much lower than expected for a single, more massive galaxy). Neglecting the TDG candidates and the galaxies in the processing of merging, a linear fit to the data yields

$$x = (6.03 \pm 0.28) + (0.238 \pm 0.031) \log M_{\text{stars}}, \quad (31)$$

where $x = 12 + \log(\text{O}/\text{H})$. This relation has a correlation coefficient of $r = 0.849$ (Fig. 13). Our $M_{\text{stars}} - Z$ relation is quite different from previous relations given in the literature. For comparison, the $M_{\text{stars}} - Z$ diagram includes the relations provided by Tremonti et al. (2004) and Kewley & Ellison (2008) using the Pilyugin (2001b) calibration to compute the oxygen abundance². Tremonti et al. (2004) derived the oxygen abundances using theoretical photoionization models, which overestimate the metallicity derived from the direct T_e method between 0.2 and 0.4 dex (see Paper IV). Hence, we also plot in Fig. 13 the Tremonti et al. (2004) relation corrected by a factor of 0.3 dex in oxygen abundance. As we see, Tremonti et al. (2004) relation is steeper than that derived here, and does not agree with our data. On the other hand, the Kewley & Ellison (2008) relation is quite flat in comparison with our observational data. These authors comment that, for masses between 3×10^8 and $10^{11} M_{\odot}$, the metallicity of their sample galaxies rises only ~ 0.2 dex on average, but we find a variation of ~ 0.7 dex in the same mass interval.

Interestingly, Kewley & Ellison (2008) did not derive any $M_{\text{stars}} - Z$ relation using oxygen abundances determined with the T_e method, since the SDSS catalog contains very few metal-poor and starbursting galaxies, and the scatter of the available data is huge. These authors finally conclude that the choice of the metallicity calibration has the strongest effect on the $M - Z$ relation, because a considerable variation in shapes and y -intercepts is found. Many of their fits suggest a flatter $M - Z$ relation at higher masses, something that was previously noticed by Tremonti et al. (2004). These authors explain this issue as a consequence of effective galactic winds that remove metals from the low-mass galaxies ($M \leq 10^{10.5} M_{\odot}$). Although our data do not allow exploration of this issue at high masses, we do not see any trend from this effect.

It is very interesting that Tol 9, in which we detect a clear example of galactic wind, has a relatively low stellar mass for

² As we concluded in Paper IV, this calibration provides the best results to the oxygen abundances derived for our galaxies, which were mainly computed following the direct T_e method.

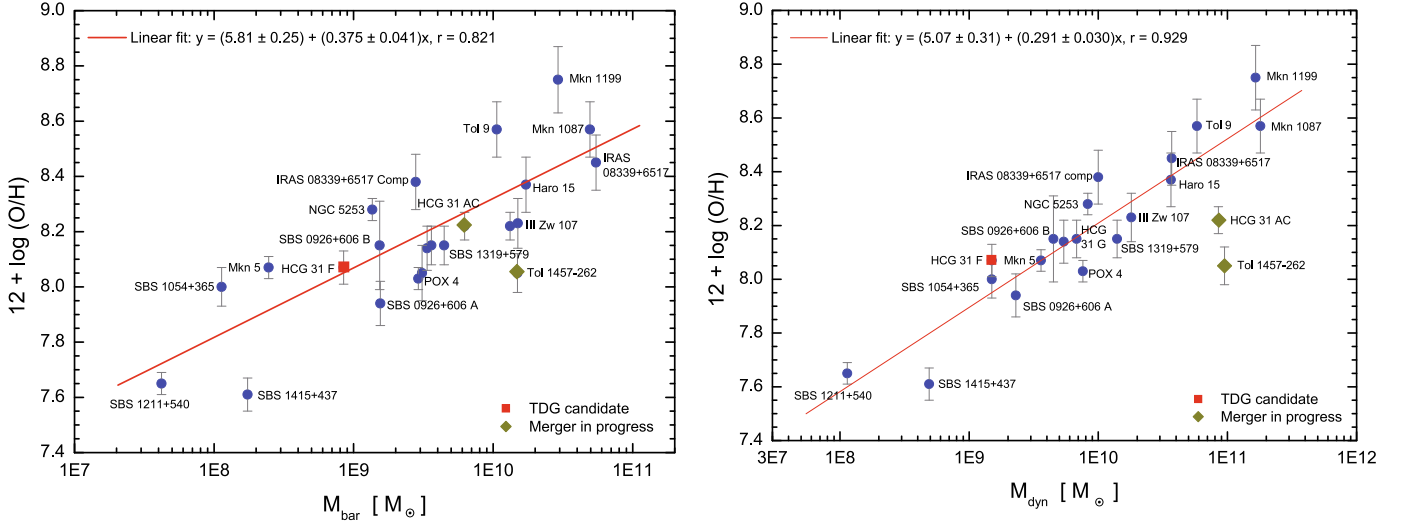


Fig. 14. Relation between M_{bar} (*left panel*) and M_{dyn} (*right panel*) with the oxygen abundance for our galaxy sample. The TDG candidate HCG 31 F is plotted with a red square, while HCG 31 AC and Tol 1457-262, which are galaxies in the process of merging, are shown with a yellow diamond. A linear fit to the data without considering these problematic objects is shown with a continuous red line in both diagrams.

its expected metallicity. Probably that indicates the strength and youth of the star-formation phenomena in this BCG. We should expect that the position of this object in the $M_{\text{stars}}-\text{O}/\text{H}$ diagram will move to higher masses and lower metallicities if the star-formation processes continue and if the fresh new material is expelled far from the galaxy via the effect of galactic winds.

The linear fits to the $M_{\text{bar}}-Z$ and $M_{\text{dyn}}-Z$ relations, which do not consider TDG candidates and mergers in progress, are

$$x = (5.81 \pm 0.25) + (0.375 \pm 0.041) \log M_{\text{bar}}, \quad (32)$$

$$x = (5.07 \pm 0.31) + (0.291 \pm 0.030) \log M_{\text{dyn}}, \quad (33)$$

where $x=12+\log(\text{O}/\text{H})$. The correlation coefficients are $r = 0.821$ and $r = 0.929$ for the $M_{\text{bar}}-Z$ and $M_{\text{dyn}}-Z$ relations, respectively. The slopes of all the $M-Z$ relations agree relatively closely. We note the tightness of the $M_{\text{dyn}}-Z$ relation: except for the mergers in progress (HCG 31 AC and Tol 1457-262), all galaxies are found relatively close to the relation. This indicates that the dark matter content of the galaxies also increases with the metallicity, in agreement with the predictions of the evolutionary galaxy models.

In summary, the scatter observed in the luminosity-metallicity and in the mass-metallicity relationships of star-forming galaxies are a consequence of both the nature and the star-formation histories experienced by these objects. Only a detailed analysis of each system can give the clues needed to understand the evolution of the global properties in star-forming galaxies and their comparison between dwarf, normal, and massive galaxies.

7. Schmidt-Kennicutt relation

We now investigate whether the studied galaxies obey the Schmidt-Kennicutt scaling laws of star-formation. It is well known that a tight correlation exists between the average SFR per unit area and the mean surface density of the cold gas on galactic scales. Such a correlation is usually parameterized via a power-law relation (Schmidt 1959, 1963; Kennicutt 1998; Kennicutt et al. 2007) that has proven to be very useful as an input scaling law for analytical and numerical models of galaxy evolution (e.g., Kay et al. 2002).

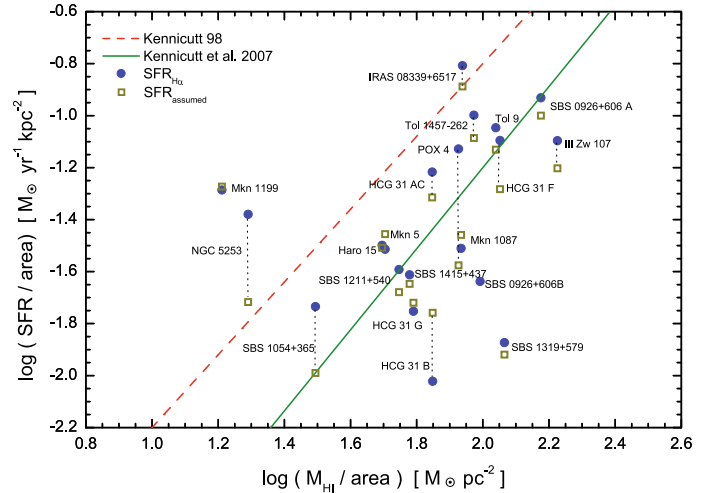


Fig. 15. Relation between the SFR/area and the HI gas density for our galaxy sample. We show two values per galaxy, one assuming the $\text{H}\alpha$ -based SFR following the Kennicutt (1998) calibration (blue circles) and the other considering the SFR assumed by combining all multi-wavelength data. The solid green line is the best fit to the M 51 data (Kennicutt et al. 2007); the dashed red line is the relation for integrated values of star-forming galaxies derived by Kennicutt (1998).

Figure 15 shows, on a logarithm scale, the SFR per unit area versus the surface density of the HI gas ($M_{\text{HI}}/\text{area}$) for all the galaxies for which we have HI measurements. We plot two values for each galaxy, one assuming the $\text{H}\alpha$ -based SFR using Kennicutt (1998) calibration and other considering the SFR assumed combining all multiwavelength data (last column in Table 5). Almost both values are quite similar in all galaxies except in some objects, especially POX 4 and NGC 5253. The majority of the galaxies are located close to the relation given by Kennicutt et al. (2007), which is the best fit to the data of star-forming regions within the nearby Sbc galaxy M 51. These authors also include the molecular gas to get this relation, but we have not considered it in our galaxy sample. The assumption that neglecting the molecular gas is valid in low-mass,

Table 8. Mass-to-light ratios of all mass estimations compiled in Table 7.

| Galaxy | $\frac{M_{\text{HI}}}{L_B}$ | $\frac{M_{\text{HII}}}{L_B}$ | $\frac{M_{\text{dust}}}{L_B}$ | $\frac{M_{\star}}{L_B}$ | $\frac{M_{\text{Kep}}}{L_B}$ | $\frac{M_{\text{dyn}}}{L_B}$ | $\frac{M_{\text{stars}}}{L_B}$ | $\frac{M_{\text{bar}}}{L_B}$ | $\frac{M_{\text{bar}}}{M_{\text{dyn}}}$ | $\frac{M_{\text{stars}}}{M_{\text{bar}}}$ | $\frac{M_{\text{gas}}}{M_{\text{bar}}}$ | $\frac{M_{\text{gas}}}{M_{\text{stars}}}$ | $\frac{M_{\text{dust}}}{M_{\text{gas}}}$ |
|--------------------|--------------------------------------------|-------------------------------------------------|-------------------------------------------------|-------------------------------------------------|--------------------------------------------|--------------------------------------------|--------------------------------------------|--------------------------------------------|-----------------------------------------|-------------------------------------------|-----------------------------------------|-------------------------------------------|------------------------------------------|
| | $\left[\frac{M_{\odot}}{L_{\odot}}\right]$ | $\left[10^4 \frac{M_{\odot}}{L_{\odot}}\right]$ | $\left[10^4 \frac{M_{\odot}}{L_{\odot}}\right]$ | $\left[10^4 \frac{M_{\odot}}{L_{\odot}}\right]$ | $\left[\frac{M_{\odot}}{L_{\odot}}\right]$ | $\left[\frac{M_{\odot}}{L_{\odot}}\right]$ | $\left[\frac{M_{\odot}}{L_{\odot}}\right]$ | $\left[\frac{M_{\odot}}{L_{\odot}}\right]$ | | | | | $[10^4]$ |
| HCG 31 | 0.369 | 3.86 | 1.27 | 18.7 | ... | ... | 0.167 | 0.655 | ... | 0.255 | 0.744 | 2.91 | 2.60 |
| " AC | 0.395 | 5.86 | ... | 19.8 | 3.7 | 9.23 | 0.156 | 0.678 | 0.073 | 0.231 | 0.769 | 3.34 | ... |
| " B | 0.409 | 0.96 | ... | 17.3 | 0.55 | 1.14 | 0.169 | 0.709 | 0.622 | 0.238 | 0.762 | 3.20 | ... |
| " E | ... | 7.09 | ... | 83.7 | ... | 4.15 ^a | 0.150 | ... | ... | ... | ... | ... | ... |
| " F | 1.53 | 13.7 | ... | 28.6 | 0.75 | 3.73 | 0.097 | 2.11 | 0.565 | 0.046 | 0.954 | 20.8 | ... |
| " G | 0.350 | 1.72 | ... | 12.6 | 0.38 | 1.23 | 0.189 | 0.651 | 0.531 | 0.290 | 0.710 | 2.44 | ... |
| Mkn 1087 | 0.138 | 0.92 | 0.69 | 11.4 | 0.50 | 1.60 | 0.256 | 0.438 | 0.274 | 0.583 | 0.417 | 0.715 | 3.78 |
| " N | ... | 1.29 | ... | 12.8 | 0.084 | 2.78 | 0.153 | ... | ... | ... | ... | ... | ... |
| Haro 15 | 0.159 | 1.79 | 0.60 | 22.2 | 0.35 | 1.05 | 0.286 | 0.495 | 0.471 | 0.577 | 0.423 | 0.732 | 2.85 |
| Mkn 1199 | 0.0419 | 2.49 | 1.07 | 48.0 | 0.28 | 5.67 | 0.945 | 1.00 | 0.177 | 0.945 | 0.055 | 0.059 | 19.2 |
| " NE | ... | 0.78 | ... | 10.1 | 0.17 | 4.22 ^a | 1.05 | ... | ... | ... | ... | ... | ... |
| Mkn 5 | 0.273 | 3.08 | 3.76 | 11.4 | 8.0 | 13.7 | 0.575 | 0.936 | 0.068 | 0.614 | 0.386 | 0.628 | 10.4 |
| IRAS 08208+2816 | ... | 4.14 | 1.73 | 32.5 | 0.076 | 1.18 ^a | 0.585 | ... | ... | ... | ... | ... | ... |
| IRAS 08339+6517 | 0.0805 | 2.19 | 0.59 | 34.2 | 0.151 | 0.56 | 0.720 | 0.827 | 1.48 | 0.871 | 0.129 | 0.148 | 5.57 |
| " Comp | 0.234 | 0.87 | ... | 1.37 | ... | 3.34 | 0.623 | 0.932 | 0.279 | 0.669 | 0.331 | 0.496 | ... |
| POX 4 | 0.219 | 11.2 | 0.183 | 19.1 | 0.098 | 1.49 | 0.281 | 0.570 | 0.383 | 0.492 | 0.508 | 1.03 | 0.63 |
| " Comp | ... | 2.30 | ... | 36.4 | ... | ... | 0.406 | ... | ... | ... | ... | ... | ... |
| UM 420 | ... | 6.76 | 4.9 ^b | 13.4 | 0.204 | 1.94 ^a | 0.444 | ... | ... | ... | ... | ... | ... |
| SBS 0926+606 | 0.664 | 6.58 | 1.39 | 31.6 | ... | ... | 0.285 | 1.16 | ... | 0.246 | 0.754 | 3.97 | 1.59 |
| " A | 0.746 | 10.9 | ... | 28.0 | ... | 1.79 | 0.226 | 1.21 | 0.676 | 0.187 | 0.813 | 4.35 | ... |
| " B | 0.587 | 2.54 | ... | 34.5 | ... | 3.26 | 0.340 | 1.11 | 0.342 | 0.305 | 0.695 | 2.28 | ... |
| SBS 0948+532 | ... | 31.7 | ... | 51.4 | 0.57 | 2.46 ^a | 0.345 | ... | ... | ... | ... | ... | ... |
| SBS 1054+365 | 0.929 | 10.2 | 1.83 | 35.1 | 1.19 | 22.9 | 0.505 | 1.73 | 0.076 | 0.292 | 0.798 | 2.43 | 1.50 |
| SBS 1211+540 | 0.762 | 6.61 | ... | 15.8 | 3.57 | 3.61 | 0.321 | 1.33 | 0.368 | 0.242 | 0.758 | 3.13 | ... |
| SBS 1319+579 | 0.408 | 0.88 | 0.75 | 1.94 | 2.14 | 3.48 | 0.669 | 1.11 | 0.318 | 0.514 | 0.486 | 0.946 | 1.40 |
| SBS 1415+437 | 0.964 | 7.35 | ... | 14.0 | 2.50 | 4.90 | 0.465 | 1.74 | 0.355 | 0.268 | 0.732 | 2.74 | ... |
| III Zw 107 | 0.378 | 3.37 | 0.71 | 41.8 | 0.046 | 1.02 | 0.349 | 0.848 | 0.834 | 0.412 | 0.588 | 1.43 | 1.42 |
| Tol 9 ^e | 0.595 | 4.32 | 3.06 | 34.8 | 0.152 | 7.38 | 0.564 | 1.35 | 0.183 | 0.418 | 0.582 | 1.39 | 3.90 |
| Tol 1457-262 | 0.258 | 5.17 | 1.01 | 22.5 | ... | 5.22 | 0.479 | 0.820 | 0.157 | 0.584 | 0.416 | 0.711 | 2.95 |
| " Obj 1 | ... | 5.70 | ... | 19.3 | 0.051 | 2.40 ^a | 0.387 | ... | ... | ... | ... | ... | ... |
| " Obj 2 | ... | 4.25 | ... | 23.9 | ... | 2.49 ^a | 0.601 | ... | ... | ... | ... | ... | ... |
| Arp 252 | ... | 3.01 | 1.45 | 18.9 | ... | ... | 0.775 | ... | ... | ... | ... | ... | ... |
| " ESO 566-8 | ... | 3.57 | ... | 12.9 | 0.21 | 1.54 ^a | 0.716 | ... | ... | ... | ... | ... | ... |
| " ESO 566-7 | ... | 1.09 | ... | 19.6 | 0.047 | 1.75 ^a | 1.03 | ... | ... | ... | ... | ... | ... |
| NGC 5253 | 0.069 | 2.84 | 0.182 | 9.67 | ... | 3.60 | 0.496 | 0.594 | 0.164 | 0.842 | 0.158 | 0.192 | 1.97 |

Notes. ^(a) Using the tentative value of M_{dyn} computed using Eq. (25).

low-metallicity galaxies, because of both the difficulty of detecting CO and the uncertainties of the correspondence between CO and H_2 in low-metallicity objects (i.e., Wilson 1995; Taylor et al. 1998; Braine et al. 2004). However, we should expect some molecular gas contribution in more massive galaxies, such as IRAS 08339+6517, Mkn 1087 and Mkn 1199.

From Fig. 15, it is evident that our data agree much more with the relation given by Kennicutt et al. (2007) than with the relation obtained by Kennicutt (1998) for star-forming galaxies (and not regions within galaxies). Interestingly, a recent study of the star-formation activity within UV-rich regions found in the outskirts of the galaxy pair NGC 1512/1510 (Koribalski & López-Sánchez 2009) yield the same result. We plotted the $\text{H}\alpha$ -based SFR using the Kennicutt (1998) calibration because both Kennicutt (1998) and Kennicutt et al. (2007) relations use this calibration. When using the $\text{H}\alpha$ -based SFR derived from the Calzetti et al. (2007) calibration, the agreement of our data with the Kennicutt et al. (2007) relation will be even closer. Some clear disagreements with the scaling laws of star-formation are Mkn 1199 and NGC 5253 (both seem to be HI deficient; the molecular gas component in Mkn 1199 would not explain its position in the diagram, as it would require that $\sim 40\%$ of the total neutral hydrogen mass is H_2 , but the star-formation has

been probably enhanced in NGC 5253) and III Zw 107 and SBS 1319+579 (that show lower SFR than predicted by their HI gas amount). We then conclude that some external factors are indeed affecting the *normal* star-formation activity in these three galaxies.

8. Analysis of the mass-to-light ratios

Table 8 compiles all the mass-to- B luminosity ratios derived in this work. Some interesting relations are plotted in Figure 16, which compares some mass-to-light ratios with the stellar mass derived from the H -band luminosity.

The HI mass-to-light ratio of a galaxy is a distance-independent quantity that compares the HI mass with the luminosity in the B -band. This property correlates with many galaxy parameters, such as the galaxy type, galaxy color, or galaxy mass (Roberts & Haynes 1994). Indeed, the comparison of the M_{HI}/L_B ratio with the stellar mass in our sample galaxy clearly indicates that less massive galaxies have a higher mass fraction of neutral gas. The majority of the galaxies have a HI-mass-to-light ratio between 0.1 and 1.0, in agreement with previous estimations in star-forming dwarf galaxies (Salzer et al. 2002; Huchtmeier et al. 2005). We note some peculiar

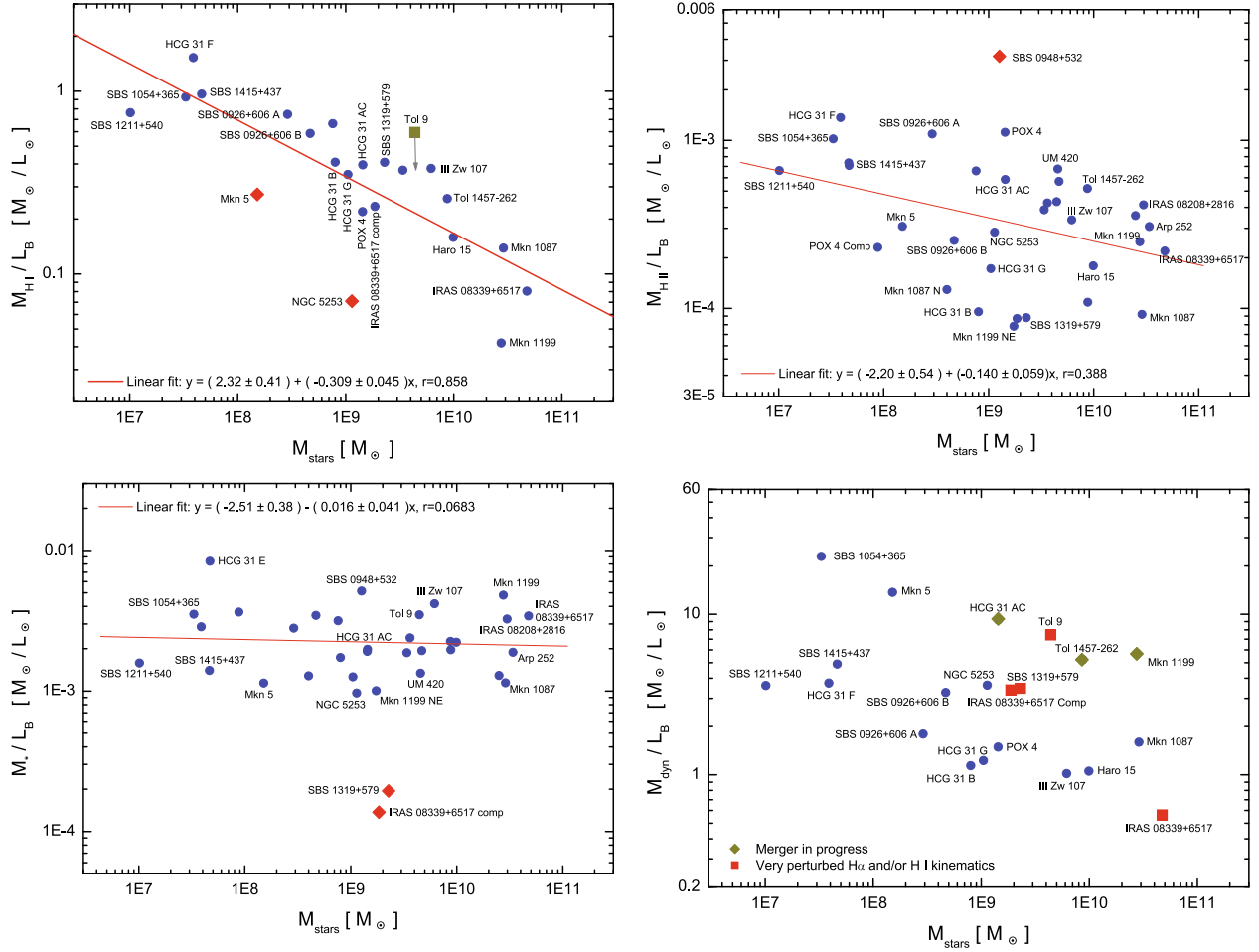


Fig. 16. Comparison between the stellar mass and some mass-to-light ratios for our sample galaxies.

objects in this diagram. The HI-mass of Tol 9 has been overestimated because the HI cloud in which it is embedded includes several dwarf galaxies (López-Sánchez et al. 2008b, 2010b). On the other hand, two galaxies (Mkn 5 and NGC 5253) are very HI-deficient. In particular, NGC 5253 is very far from the typical position of the galaxies, showing an M_{HI}/L_B of $\sim 0.07 M_{\odot}/L_B$. This ratio for Mkn 1199 is also slightly low, even for a massive galaxy. As already suggested (Sect. 3.4.3 of Paper II), Mkn 1199 may have lost part of its neutral gas in the interaction process with its NE companion. Neglecting the contribution of Tol 9, Mkn 5, and NGC 5253, a linear fit provides the empirical relation

$$\log \frac{M_{\text{HI}}}{L_B} = (2.32 \pm 0.41) - (0.309 \pm 0.045) \log M_{\text{stars}}, \quad (34)$$

which has a correlation coefficient of $r = 0.858$.

We do not find any high M_{HI}/L_B ratio ($>1 M_{\odot}/L_B$) in our sample galaxy, except in the case of the TDG candidate HCG 31 F, which has $1.53 M_{\odot}/L_B$. High HI mass-to-light ratios have been reported in a few galaxies. The detailed analysis of the gas-rich low surface brightness dwarf irregular galaxy ESO 215-G009 performed by Warren et al. (2004) confirms an extremely high M_{HI}/L_B of $22 \pm 4 M_{\odot}/L_B$ in this galaxy, for which the HI disk extends 6.4 ± 0.4 times the Holmberg radius. They conclude that ESO 215-G009, which is very isolated (no neighbors identified out to 1 Mpc), has a low SFR that probably remained unchanged throughout the galaxy's existence. In a subsequent paper (Warren et al. 2006) these authors suggest that high M_{HI}/L_B galaxies do not lack the baryons needed to create

stars, but are underluminous since they lack either the internal or external stimulation for more extensive star-formation.

Warren et al. (2007) have derived an empirical upper envelope for M_{HI}/L_B as a function of the absolute B -magnitude, which accounts for the maximum amount of atomic hydrogen gas a galaxy of a particular luminosity can retain in the Universe today. All our sample galaxies satisfy this empirical relation.

The derived M_{HII}/L_B ratios for our galaxy sample lie in the range $10^{-3} - 10^{-4} M_{\odot}/L_B$. Although the scatter of our data is high (a tentative linear fit gives a very low correlation coefficient), they indicate that the M_{HII}/L_B ratio slightly decreases with increasing stellar mass, suggesting that the ionized gas to stars ratio is higher in dwarf galaxies. SBS 0948+532 is far away from the rest of the objects because of its very high H α flux (see Sect. 3.11 in Paper I). On the other hand, the ionizing star cluster mass-to-light ratio, M_{\star}/L_B , seems to be constant with the stellar mass, showing an average value of $\sim 0.0022 M_{\odot}/L_B$. Two galaxies, SBS 1319+579 and the companion object of IRAS 08339+6517 lie apart from this tendency, as we also saw in Fig. 9.

The M_{dyn}/L_B ratio seems to decrease slightly with the stellar mass. However, the analysis of this diagram is difficult, because interactions noticeably modify the estimation of the dynamical mass. Usually, perturbed kinematics yield to higher M_{dyn} (HCG 31 AC, Mkn 1199, Tol 1457-262, Tol 9), but sometimes the existence of tidal tails with a rather constant velocity give a lower M_{dyn} than the real one (IRAS 08339+6517). SBS 1319+579 (a probable merging of two dwarf objects), and

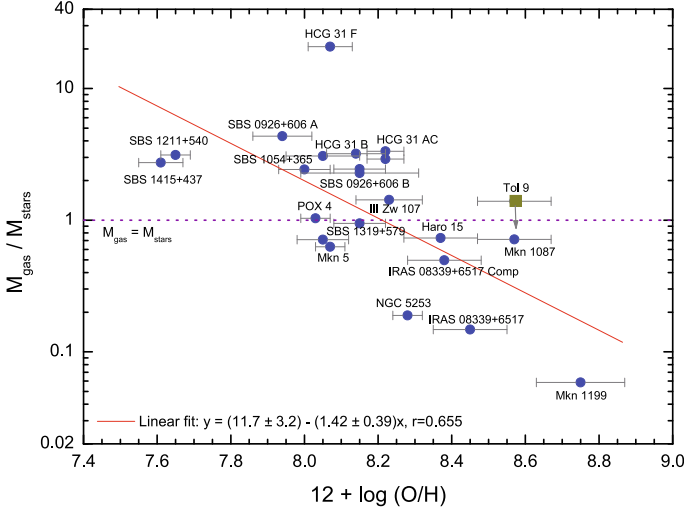


Fig. 17. Comparison of the $M_{\text{gas}}/M_{\text{stars}}$ ratio with the oxygen abundance for our sample galaxies. The dotted horizontal pink line indicates the position of $M_{\text{gas}} = M_{\text{stars}}$. The red continuous line is a linear fit to the data, neglecting Tol 9, for which the neutral gas mass corresponds to this object and some dwarf surrounding galaxies (see text and LS08).

IRAS 08339+6517 Comp (in interaction with the main galaxy of the system) also shows somewhat high M_{dyn}/L_B ratios. We suggest that galaxies Mkn 5 and SBS 1054+365, which lie far from the rest of the objects, have perturbed kinematics, with M_{dyn} overestimated in both cases.

Figure 17 compares the ratio between the gas and the stellar masses with the oxygen abundance. Clearly, $M_{\text{gas}}/M_{\text{stars}}$ decreases with increasing metallicity, indicating that the importance of the stellar component to the total mass is higher in more massive galaxies. We should expect this result, which is qualitatively the inverse behavior of the M_{HI}/L_B ratio with the stellar mass. A tentative linear fit to the data (excluding Tol 9) is plotted in Fig. 17) and provides

$$\log \frac{M_{\text{gas}}}{M_{\text{stars}}} = (11.7 \pm 3.2) - (1.42 \pm 0.39)x, \quad (35)$$

where $x = 12 + \log(\text{O}/\text{H})$, and it has a correlation coefficient of $r = 0.655$. Following this analysis, we should expect that galaxies with $12 + \log(\text{O}/\text{H}) \sim 8.2\text{--}8.3$ have relatively equal gas and stellar masses. HCG 31 F is the galaxy with highest $M_{\text{gas}}/M_{\text{stars}}$ ratio (and lowest M_{stars}/L_B ratio), indicating its low content of evolved stars. This result agrees with our suggestion (López-Sánchez et al. 2004a) that this TDG has created stars mainly using the neutral gas from the long arm-like H I structure (Verdes-Montenegro et al. 2005) found between members AC and G of the HCG 31 galaxy system.

Finally, we compare some mass-to-light ratios with the colors of the galaxies. Amorín et al. (2009) report that the underlying component (host) of blue compact galaxies is redder with decreasing M_{HI}/L_B . We do not find any correlation between the M_{HI}/L_B ratio and the optical colors of the underlying component, but we did not perform a detailed analysis of the structural parameters of the host underlying the starburst as Amorín et al. (2009) did. The comparison of the global $B\text{--}R$ color and the neutral gas mass-to-light ratio is shown in the left panel of Fig. 18, and has a huge scatter. We should call that Mkn 1199, Mkn 5 and NGC 5253 seem to be H I deficient and that IRAS 08339+6517 is a luminous blue compact galaxy (López-Sánchez et al. 2006), so their real positions in this diagram are uncertain. Although a tentative fit to the data suggests that galaxies with redder

$B - V$ colors have lower M_{HI}/L_B ratios, the huge scatter does not allow us to confirm such tendency.

However, we do observe a clear relation between the stellar-to-light ratio and the global $B - R$ color of the galaxies (right panel of Fig. 18). This tendency seems to also be a consequence of the building of the galaxies, since more massive galaxies have experienced more star-formation events than less massive objects, so they tend to show redder stellar populations than dwarf galaxies. This result also agrees quite well with the observed tendencies that M_{HI}/L_B ratio decreases with the stellar mass and that $M_{\text{gas}}/M_{\text{stars}}$ ratio decreases with increasing metallicity.

9. Dust properties in star-forming galaxies

Our data set allows us to investigate the properties and effects of the dust content in low-metallicity star-forming galaxies. Figure 19 plots the reddening coefficient, $c(\text{H}\beta)$ –obtained using our optical spectra– as a function of the warm dust mass, M_{dust} , derived from FIR data–. Neglecting the data for UM 420 (M_{dust} is overestimated because of the FIR contribution by the foreground galaxy UGC 01809), we see a clear correlation between both quantities: galaxies with higher amounts of warm dust (and hence, following Fig. 9, higher luminosity) show higher extinction. This conclusion agrees with other results in this work, such as the correlation between $c(\text{H}\beta)$ and the oxygen abundance discussed in Paper IV. More important, this result indicates that most of the dust is inside the galaxy and not in the line of sight. Detailed analysis of the dust distribution within nearby galaxies (i.e. Muñoz-Mateos et al. 2009) have found clear relationships between the dust content and general properties of nearby spiral galaxies, such as galaxy type, luminosity, and metallicity. As the extinction was derived from our optical spectra (see Paper II), we here independently confirm that the dust content and therefore the extinction in dwarf galaxies depend on their metallicities and luminosities, and very probably also on their star-formation histories. A proper estimation of the amount of dust within such objects is needed to perform appropriate statistical analysis involving larger galaxy samples.

We now investigate the dust-to-gas ratio, $M_{\text{dust}}/M_{\text{gas}}$, of our sample galaxies, a very important quantity when studying the chemical enrichment of the ISM, as it accounts for the amount of metals locked up into dust grains through the stellar yields. The correlation between the $M_{\text{dust}}/M_{\text{gas}}$ and the oxygen abundance has been reported in many studies (i.e., Lisensfeld & Ferrara 1998; James et al. 2002; Draine et al. 2007; Muñoz-Mateos et al. 2009). Figure 20 shows the dust-to-gas ratio as a function of the oxygen abundance. The gas mass was computed assuming only the H I and the He I gas, but not the contribution of the molecular gas, which is not important in dwarf low-metallicity objects. The derived dust-to-gas ratio of each galaxy for which we have both H I and FIR data are compiled in the last column of Table 8. From Fig. 20, it is evident that objects with higher metallicities tend to have higher $M_{\text{dust}}/M_{\text{gas}}$ ratios, such as the amount of dust increases and the neutral gas is consumed while galaxies are experiencing new star-formation phenomena. The linear fit to our data provides this tentative relation

$$\log(M_{\text{dust}}/M_{\text{gas}}) = (-12.0 \pm 2.9) + (1.02 \pm 0.36)x, \quad (36)$$

with $x = 12 + \log(\text{O}/\text{H})$ and correlation coefficient of $r = 0.637$. Mkn 5 lies away from the majority of the points, but this object seems to be very deficient in H I, so we did not include this point in the fit. Although with higher uncertainties, we observe that more massive objects also tend to have higher $M_{\text{dust}}/M_{\text{gas}}$ ratios.

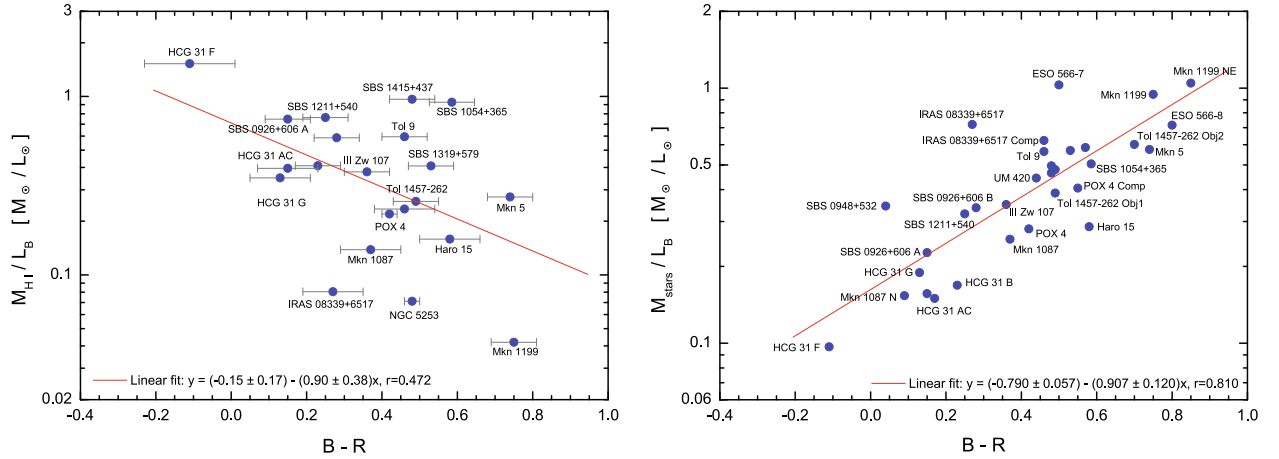


Fig. 18. Relation between the M_{HI}/L_B ratio (left panel) and the M_{stars}/L_B ratio (right panel) with the $B - R$ color for our sample galaxies. Linear fits are plotted with a continuous red line. Some objects are labeled.

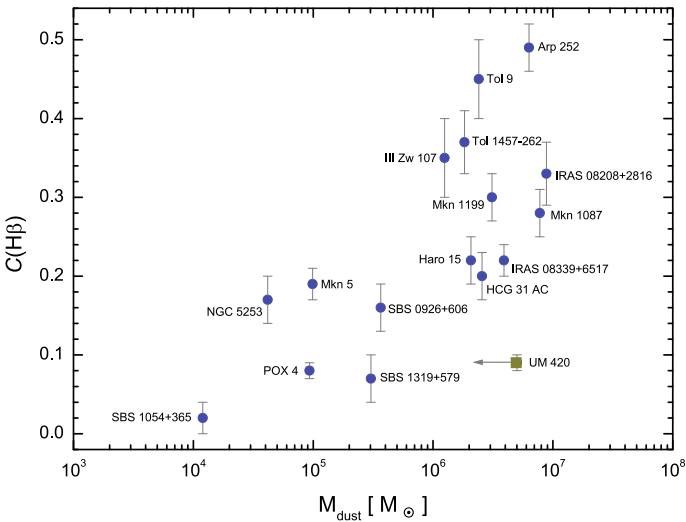


Fig. 19. Reddening coefficient, $c(\text{H}\beta)$, vs. warm dust mass, M_{dust} .

Draine et al. (2007) provide a relation between $M_{\text{dust}}/M_{\text{gas}}$ and the oxygen abundance – computed following the Pilyugin & Thuan (2005) calibration – in a sample of spiral and irregular galaxies, which we may rewrite as

$$\log(M_{\text{dust}}/M_{\text{gas}}) = 6.48 + x, \quad (37)$$

where $x = 12 + \log(\text{O}/\text{H})$ (Fig. 20). The factor 6.48 was derived from $\log[(M_{\text{dust}}/M_{\text{gas}})_{\text{MW}}/1.32] + x_{\text{MW}}$ when assuming $(M_{\text{dust}}/M_{\text{gas}})_{\text{MW}} = 0.010$ and $x_{\text{MW}} = 8.6$ for the Milky Way. As we see, this relation lies away from our data, although the slope is the same in both cases. Draine et al. (2007) also found that the global dust-to-gas ratio of all their galaxies with $12 + \log(\text{O}/\text{H}) < 8.1$ falls below this equation, sometimes by a factor greater than 10, so Fig. 20 also plots the Draine et al. (2007) relation divided by this factor. As we can see, this relation agrees better with our data. Draine et al. (2007) also pointed out that many of the low-metallicity galaxies have large H I envelopes mainly composed by unenriched material. However, the metallicity is derived from the brightest H II regions, which usually show the highest metallicities (most recent star-formation) within the system. Consequently, the derived $M_{\text{dust}}/M_{\text{gas}}$ ratio should correspond to lower oxygen abundances.

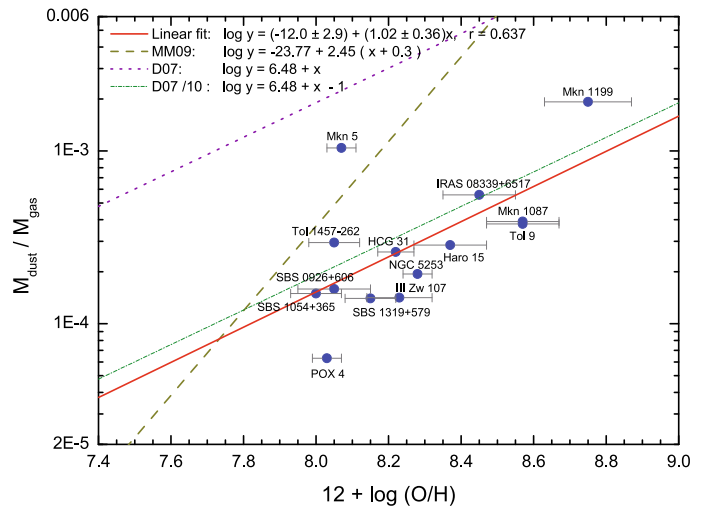


Fig. 20. Dust-to-gas ratio, $M_{\text{dust}}/M_{\text{gas}}$, vs. the oxygen abundance for our sample galaxies. The red continuous line is a fit to our data (neglecting Mkn 5). The dashed yellow line indicates the relation found by Muñoz-Mateos et al. (2009) when analyzing the radial dust-to-gas profiles for a larger sample of spiral galaxies. This relation has been corrected by 0.3 dex because it was derived by assuming the Kobulnicky & Kewley (2004) calibration to compute the oxygen abundances, which overestimates in 0.2–0.4 dex the oxygen abundance provided by the direct T_e method. The dotted pink line is the relation provided by Draine et al. (2007) in their analysis of a sample of spiral and irregular galaxies. The dashed-dotted green line indicates the Draine et al. (2007) relation divided by a factor 10.

Recently, Muñoz-Mateos et al. (2009) have analyzed the radial dust-to-gas profiles for a larger sample of spiral galaxies and find a steeper relation between $M_{\text{dust}}/M_{\text{gas}}$ and the metallicity, which they explain because the outskirts of spiral galaxies seem to have a much lower $M_{\text{dust}}/M_{\text{gas}}$ than the central regions (see their Fig. 16). These authors suggest a link with the behavior found in dwarf galaxies, because in the external regions of the spiral galaxies the neutral gas has not yet undergone star-formation. However, this trend could also be a consequence of the radial decrease in the star-formation efficiency found in nearby spirals (i.e., Thilker et al. 2007; Leroy et al. 2008).

We may check these hypotheses by comparing our data with the relation provided by Muñoz-Mateos et al. (2009). However,

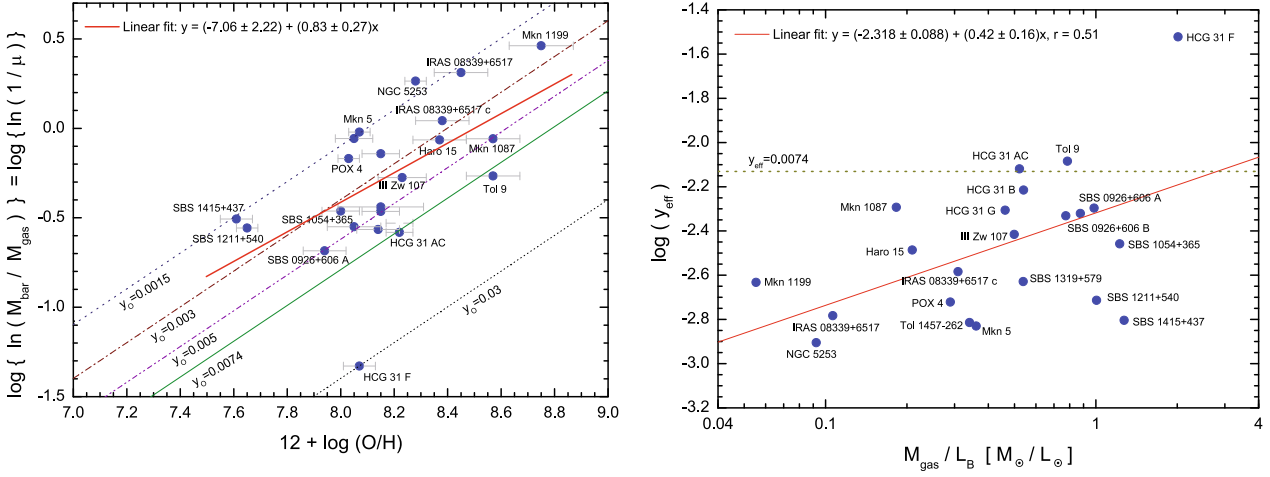


Fig. 21. (Left panel) Comparison of the observed oxygen abundance and the one predicted by simple closed-box chemical evolution models with instantaneous recycling and constant SFRs. The continuous green line indicates the expected trend if the galaxies are closed boxes with an oxygen yield $y_0 = 0.0074$ (Meynet & Maeder 2002; van Zee & Haynes 2006). Closed-box models with $y_0 = 0.0015, 0.003, 0.005,$ and 0.03 are also plotted. A linear fit to our data is shown with a continuous red line, to indicate an oxygen yield of $y_0 = 0.003\text{--}0.005$. (Right panel) Effective yield plotted as a function of the M_{gas}/L_B ratio. The closed-box yield is plotted by a dotted yellow line. A linear fit to the data is shown with a continuous red line.

we should slightly modify their equation, because these authors used the Kobulnicky & Kewley (2004) method to derive the metallicities, and this calibration overestimates the oxygen abundances provided by the direct T_e method in $0.2\text{--}0.4$ dex (see Paper IV). The modified relation that is plotted with a dashed yellow line in Fig. 20 is

$$\log(M_{\text{dust}}/M_{\text{gas}}) = -23.77 + 2.45(x + 0.3), \quad (38)$$

where $x = 12 + \log(\text{O}/\text{H})$. We see that, except for Mkn 5, all our data have lower $M_{\text{dust}}/M_{\text{gas}}$ ratios than those predicted following this relation. We therefore suggest that the low $M_{\text{dust}}/M_{\text{gas}}$ ratios found in dwarf low-metallicity galaxies is a consequence of the large reserves of unenriched neutral gas in these systems, while the low $M_{\text{dust}}/M_{\text{gas}}$ ratios reported by Muñoz-Mateos et al. (2009) in the external regions of spiral galaxies stem from the decrease in the star-formation efficiency in those areas. Indeed, the outskirts of spiral galaxies seem to show lower HI surface densities – $\log(M_{\text{H}}/\text{area}) \sim 0.4\text{--}0.8 M_{\odot} \text{pc}^{-2}$ for external regions of M 51 (Kennicutt et al. 2007) and NGC 1512 (Koribalski & López-Sánchez 2009) – than the neutral gas envelopes of dwarf galaxies – $\log(M_{\text{H}}/\text{area}) \sim 1.4\text{--}2.0 M_{\odot} \text{pc}^{-2}$ following Fig. 15 – which translates into a decreasing of the star-formation activity following the Schmidt-Kennicutt law. However, more high-quality data and a detailed analysis of both the dust and the neutral gas distribution in nearby dwarf galaxies should be performed to answer all these questions.

10. Comparison with the closed-box model

To study the environment effects of the gas content and the chemical enrichment in galaxies, it is common to compare them with the so-called *closed-box chemical evolution* model (Schmidt 1963; Searle & Sargent 1972; Edmunds 1990). According to this model, a galaxy initially consists of gas with no stars and no metals. The stellar IMF is assumed to be constant in time. Stars that end their lives as supernovae are assumed to enrich the ISM with metals immediately. Throughout its life, the galaxy experiences instantaneous recycling, and the products of stellar nucleosynthesis are neither diluted by infalling pristine

gas nor lost via outflow of enriched gas. As results, the metallicity at any given time is only determined by the fraction of baryons that remain in gaseous form. The model can be written as

$$Z_{\text{O}} = y_0 \ln(1/\mu), \quad (39)$$

where Z_{O} is the oxygen mass fraction, y_0 is the yield by mass, and μ is the ratio of the gas mass to the baryonic mass, $\mu = M_{\text{gas}}/M_{\text{bar}}$. The gas mass corresponds to the hydrogen atomic gas with a correction for neutral helium, but it does not include molecular gas ($M_{\text{gas}} = 1.32 M_{\text{HI}}$) that can be neglected in low-metallicity galaxies.

The left panel of Fig. 21 compares the observed oxygen abundances to those predicted by closed-box models, which are plotted with lines with different y_0 . The green continuous line indicates the model with $y_0 = 0.0074$, which is the theoretical yield of oxygen expected for stars with rotation following Meynet & Maeder (2002) models (van Zee & Haynes 2006). As we can see, the majority of the galaxies show oxygen abundances lower than the expected by the closed-box models. The yield of oxygen that best fits our data (the *effective yield*) is $y_0 = 0.003\text{--}0.005$, in agreement with previous results found in the literature (i.e., Lee et al. 2003; van Zee & Haynes 2006; Lee et al. 2007). The sample galaxies are generally not well reproduced by the simple closed box model, and therefore inflow of pristine gas or outflow of enriched gas have played an important role in their chemical evolution.

Interestingly, there is a galaxy that hardly follows the predictions given by the theoretical closed box model, but take the opposite direction from the rest of the galaxies. Indeed, HCG 31 F shows a much *higher* oxygen abundance than expected following the closed box model. The explanation of this behavior is that this object is a TDG that was very probably formed from the material stripped from HCG 31 AC during the fly-by encounter between member G and the A+C complex (López-Sánchez et al. 2004a). The TDG has accreted a large fraction of the pre-enriched HI gas available in the arm-like structure and now hosts very intense star-formation.

Finally, the comparison of the effective yield derived in each object with some global galaxy parameters (dynamical and

baryonic mass, absolute magnitude, gas mass-to-luminosity ratio, and surface SFR) does not show any clear trend. This result is almost the same as observed by van Zee & Haynes (2006) in the analysis of a sample of isolated, dwarf, irregular galaxies. The difference is that these authors reported a strong correlation with the gas mass-to-luminosity ratio, which they explain as gas-rich galaxies that are more likely to be closed boxes. But, as we see in the right panel of Fig. 21, such a tight correlation is not satisfied by our data, although we do observe the trend that galaxies with higher M_{gas}/L_B ratios have lower effective yields. Therefore, for intense star-forming and gas-rich galaxies, the closed box model is also not valid. We then conclude that environment effects are playing a crucial role in the evolution of these galaxies.

11. Quantification of the interaction features

Throughout this paper series we have compiled new evidence of the interaction-induced star-formation activity in starburst galaxies, in particular in dwarf galaxies. Alternative mechanisms, such as the stochastic self-propagating star-formation (Gerola et al. 1980) model (which assumes statistical fluctuations of SFR) or the ideas of the cyclic gas reprocessing of the ISM (Davé & Oppenheimer 1988) or gas compression by shocks due to the mass lost by galactic winds followed by the cooling of the ISM (Thuan 1991; Hirashita 2000), fail to explain some observational characteristics and the triggering mechanism of dwarf starburst galaxies (i.e., García-Lorenzo et al. 2008; Cairós et al. 2009). In the previous section, we demonstrated that the closed-box model is not valid for explaining the chemical evolution experienced by our sample of galaxies, emphasizing the idea that environment effects are needed to understand their observed properties. Indeed, the interaction/merger scenario naturally explains the starburst activity in these objects as just a consequence of the evolution of the galaxies throughout the cosmic time following hierarchical formation models (Kauffmann & White 1993; Kauffmann et al. 1997; Springel et al. 2005). These models predict that most galaxies have formed by merging small clouds of protogalactic gas and that galaxy interactions between dwarf objects are very common at high redshifts.

However, the interaction features in dwarf objects are, in many cases, not evident because of the lack of deep and high-resolution images and spectra (Méndez & Esteban 2000) and detailed multiwavelength analyses. It is well known that interactions in dwarf galaxies are usual not with nearby giant galaxies (Campos-Aguilar et al. 1993; Telles & Terlevich 1995; Telles & Maddox 2000) but with low surface brightness galaxies (Wilcots et al. 1996; Noeske et al. 2001; Pustilnik et al. 2001), or HI clouds (e.g., Taylor et al. 1993, 1995, 1996; Thuan et al. 1999; van Zee et al. 2001; Begum et al. 2006; Ekta et al. 2006; Hutchmeier et al. 2008; López-Sánchez & Esteban 2008). Méndez & Esteban (2000) suggested, for the first time, that interactions with or between dwarf objects could be the main star formation triggering mechanism in dwarf galaxies. Later, Östlin et al. (2001) and Bergvall & Östlin (2002) suggested that a merger between two galaxies with different metallicities or in-fall of intergalactic clouds could very probably explain the starburst activity in the most luminous BCDGs. Since then, studies of individual objects have also shown that interactions do play a decisive role in the evolution of these systems (Johnson et al. 2004; Bravo-Alfaro et al. 2004; 2006; Cumming et al. 2008; García-Lorenzo et al. 2008; James et al. 2009, 2010).

Our exhaustive multiwavelength analysis of starburst galaxies, that combined broad-band optical/NIR and H α photometry, optical spectroscopy, and X-ray, UV, FIR, 21-cm HI line,

and 1.4 GHz radio-continuum data compiled from the literature allowed us to perform a quantitative analysis of the interaction features detected in each object. A summary of the results found in each individual system of our WR galaxy sample is presented in Appendix A. To quantify the interaction features, we compile in Table 9 some interaction indicators classified in several categories, which we describe below.

1. Morphological features, such as the detection of faint plumes or bridges (Haro 15, IRAS 08339+6517, SBS 0926+606 B, SBS 1211+540, III Zw 107, Tol 9, Tol 1457-262, Arp 252), prominent tails (HCG 31, Mkn 1087, IRAS 08208+2816, UM 420, SBS 0948+532, Arp 252), disturbed morphology (HCG 31, POX 4, Tol 1457-262), TDGs candidates (HCG 31, Mkn 1087, SBS 0926+606 B, Arp 252) or mergers.
2. Kinematical features detected in the analysis of the ionized gas (see Paper II) and the neutral gas (only in those systems for which interferometer HI maps are available). The kinematical evidence found in the ionized gas of our sample galaxy includes: presence of objects with velocities decoupled from the main rotation pattern (Mkn 1087, Haro 15), sinusoidal velocity patterns that suggest a merging process (HCG 31 AC, Mkn 1199, IRAS 08208+2816, SBS 0926+606 A, III Zw 107, *Object 1* in Tol 1457-262), reversals in the velocity distribution (Tol 9, Arp 252), indications of tidal streaming (HCG 31, IRAS 08208+2816, SBS 1319+579, Tol 9), or the presence of TDG candidates (HCG 31 F1 and F2, Mkn 1087, IRAS 08339+6517, POX 4, Tol 1457-262).
3. Chemical abundance differences within several star-forming regions within the same system: Mkn 1087, Haro 15, and Mkn 1199 are clearly interacting with dwarf galaxies with lower O/H and N/O ratios. NGC 5253, IRAS 08208+2816, and Tol 1457-262 contain zones of different chemical composition. In the case of NGC 5253, this is produced by localized pollution of massive stars, but in the cases of IRAS 08208+2816 and Tol 1457-262 the different chemical compositions seem to be caused by the regions corresponding to different galaxies in interaction.
4. Furthermore, our multiwavelength analysis has provided us further indications of galaxies that do not follow their expected behavior. The analysis of the mass-to-light ratios indicates very low M_{HI}/L_B in SBS 1319+579 and NGC 5253, high M_{HII}/L_B in SBS 0948+532, low M_{\star}/L_B in SBS 1319+579, and high M_{dyn}/L_B in HCG 31 AC, Mkn 1199, Mkn 5, SBS 1054+365, Tol 9, and Tol 1457-262. Other evidence includes low HI mass content from single-dish data (Mkn 1199, Mkn 5), very extended HI emission embedding several nearby galaxies as HCG 31 (VM03) and Tol 9 (LS08, LS+10b), high M_{Kep} (Mkn 5, IRAS 08339+65 Comp, SBS 1211+540, SBS 1319+579), or strong deviations from the star-formation law (Mkn 1199, SBS 1319+579 and NGC 5253). These features may have been produced by interactions (loss of HI mass, enhancing of the star-formation activity, perturbed dynamics), but they are just indirect evidence that should be confirmed by new deep observations (i.e., HI maps).

A question mark in Table 9 indicates that the available data do not allow us to confirm this indicator. The last column in Table 9 compiles the interaction degree that each system is experiencing after considering all positive interaction indicators. We divided the interaction degree into four classes: low (no clear signs of interactions), probable (there are some interaction indicators,

Table 9. Interaction features in our WR galaxy sample.

| Galaxy | Morphological features | | | | Kinematics feat. | | Differ. in abundances | M/L_B ratios | Other features | INTERACTION DEGREE |
|------------------------------|------------------------|------|--------|------|------------------|---------|-----------------------|----------------|----------------|-----------------------|
| | Plume | Tail | Merger | TDGs | H II gas | H I gas | | | | |
| HCG 31 AC ^a | X | X | X | X | X | X | X | X | X | VERY HIGH |
| Mkn 1087 | – | X | – | X | X | ... | X | – | – | HIGH |
| Haro 15 | ? | – | X | ? | X | ... | X | – | – | VERY HIGH |
| Mkn 1199 ^a | X | – | X | – | X | ... | X | X | X | VERY HIGH |
| Mkn 5 | – | – | – | – | – | ... | ? | X | X | LOW |
| IRAS 08208+2816 | – | X | ? | ? | X | ... | X | – | – | VERY HIGH |
| IRAS 08339+6517 ^a | X | – | – | ? | X | X | – | – | – | HIGH |
| POX 4 | X | – | – | ? | X | X | – | – | X | HIGH |
| UM 420 | – | X | ? | – | ? | ... | – | – | – | VERY HIGH |
| SBS 0926+606 A | X | – | X | – | X | ... | – | – | – | VERY HIGH |
| SBS 0926+606 B | X | X | – | ? | X | ... | – | – | – | HIGH |
| SBS 0948+532 | – | X | – | – | ? | ... | – | X | – | PROBABLE |
| SBS 1054+365 | – | – | – | ? | X | ... | – | X | X | LOW |
| SBS 1211+540 | X | – | ? | – | X | ... | – | – | – | PROBABLE |
| SBS 1319+579 | – | – | ? | – | X | ... | ? | X | X | PROBABLE |
| SBS 1415+437 | – | – | – | – | ? | ... | – | – | – | LOW |
| III Zw 107 | X | – | ? | – | X | ... | ? | X | – | HIGH |
| Tol 9 | X | – | – | – | X | X | – | X | X | HIGH |
| Tol 1457-262 | X | – | X | X | X | ... | X | – | – | VERY HIGH |
| Arp 252 ^a | X | X | – | X | X | ... | X | – | – | VERY HIGH |
| NGC 5253 | – | – | – | – | X | X | X | X | X | PROBABLE ^b |

Notes. ^(a) Some interaction features in this galaxy were previously reported by other authors.

^(b) The chemical differences and the kinematics features can be explained by other reasons. See López-Sánchez et al. (2007, 2010a).

but deeper data are needed to confirm it), high (we found clear evidence of interactions, but we do not see merger features) and very high (in the cases of finding clear merger features).

Evident mergers between independent objects with relatively similar masses (major mergers) have been detected in HCG 31 AC, SBS 0926+606 A, IRAS 08208+2816 and Tol 1457+262. The galaxy pair Arp 252, which is composed of ESO 566-7 and ESO 566-8, also seems to be experiencing the first stages of a major merger. Minor mergers are found in Haro 15 and Mkn 1199. UM 420 seems also to be experiencing a merger, as deep 2D optical spectroscopy (James et al. 2009) suggests. All these galaxies have a very high degree of interaction.

Mkn 1087, IRAS 08339+6517, POX 4, SBS 0926+606 B, III Zw 107, and Tol 9 are clearly interacting with nearby dwarf objects. In the case of POX 4, we still have to investigate (López-Sánchez et al. 2010b) whether its dwarf companion galaxy is a TDG candidate and the interaction was with a nearby diffuse H I cloud, or if this object actually is an independent dwarf galaxy that has crossed the main body of POX 4 (Méndez & Esteban 1997). These six galaxies have a high degree of interaction.

On the other hand, we find probable evidence of interaction in SBS 0948+532 (enhanced star-formation activity, long optical tail, probable disturbed kinematics of the ionized gas), SBS 1211+540 (diffuse optical plumes, minor merger indications), SBS 1319+579 (peculiar $M_{H I}/L_B$, $M_{H II}/L_B$, and M_*/L_B ratios, perturbed kinematics suggesting merging or tidal stream phenomena). The H I data of NGC 5253 shows disturbed morphology and kinematics (López-Sánchez et al. 2008a), suggesting that this BCDG has disrupted or recently accreted a dwarf gas-rich companion (Kobulnicky & Skillman 2008; López-Sánchez et al. 2010a).

Only Mkn 5, SBS 1054+364, and SBS 1415+437 do not show evidences of interaction in our exhaustive multiwavelength study. However, Mkn 5 seems to be H I-deficient and seems to possess a perturbed neutral gas kinematics because of

its relatively high M_{dyn}/L_B ratio. SBS 1054+364 also shows a high M_{dyn}/L_B ratio that may suggest perturbed H I kinematics. Furthermore, the chemical abundance of this galaxy is much higher than expected from its baryonic mass. On the other hand, SBS 1415+437 shows a relatively low oxygen abundance for its baryonic mass.

Considering all indicators, we find that 13 up to 20 systems (68% of our WR galaxy sample) are classified with a high or very high degree of interaction. Four of these objects (HCG 31, Mkn 1199, IRAS 08339+6517 and Arp 252) show well known evidence of interaction, but our analysis reinforces the evidence and improves our knowledge of these systems. Only three galaxies (Mkn 5, SBS 1054+364, and SBS 1415+437) do not show interaction features, but they show considerable divergences from some properties when comparing them with similar objects. It is thus evident that the majority of the analyzed galaxies (17 up to 20) are interacting or merging with or between dwarf objects. Our analysis therefore demonstrates the importance of the low-luminosity galaxies, H I clouds, and dwarf objects in the evolution of the galaxies. Interactions with dwarf galaxies may also initiate star-formation events in normal spiral galaxies, such that it occurs in the external arms of Mkn 1199, in Haro 15, in the surroundings of Mkn 1087, or in the impressive galaxy pair NGC 1512/1510 (Koribalski & López-Sánchez 2009). Definitely, interaction between dwarf galaxies is one of the main triggering mechanisms of the star-formation in starburst galaxies, but these dwarf objects are only detected when deep optical images and spectroscopy and complementary H I observations are obtained.

12. Conclusions

We have presented a comprehensive analysis of a sample of 20 starburst galaxies that show the presence of a substantial population of very young massive stars, most of them classified as WR galaxies. In this paper, the last of the series, we analyzed

the global properties of our galaxy sample using all multiwavelength data, which include X-ray, FUV, FIR, and radio (both HI spectral line at 21 cm and 1.4 GHz radio-continuum) results. Each system was carefully analyzed considering all available data (those specifically obtained for this work and those compiled from literature) with the final aim of understanding its chemical and dynamical evolution, its stellar, dust, gas, and dark matter content, the relative importance of its stellar populations (WR, young, intermediate-age and old stars) and its star-formation properties. We produced the most complete, detailed, and exhaustive data set of this kind of galaxies, so far, involving multiwavelength data and a careful analysis of each individual object following the same procedures and equations. Our main conclusions are the following:

1. We compared the values of the SFR derived from several indicators that consider fluxes at different wavelengths. The results agree well within the experimental errors and with our H α -based values obtained after correcting for reddening and [N II] contribution. However, we consider that the new H α -based calibration provided by Calzetti et al. (2007) should be preferred over the well-known and extensively used Kennicutt (1998) calibration. Additionally, we checked that the FUV-based SFR very often shows similar results to those obtained using the emission of the ionized gas, providing a powerful tool to analyze independently the star-formation activity in both global and local scales.
2. We checked that the SFR/ L_B ratio decreases with increasing metallicity. We derived empirical relationships between the U -band, B -band, and X-ray luminosities and the SFR, which can only be used in starburst galaxies and as a first estimation of the real SFR value.
3. All objects except one in our galaxy sample satisfy the FIR-radio correlation, indicating that they are pure star-forming systems. Only the galaxy ESO 566-8 lies away from the FIR-radio correlation because it seems to host some kind of nuclear activity. The nonthermal-to-thermal ratio seems to increase with increasing luminosity, suggesting that the cosmic-ray confinement is more efficient in massive galaxies than in dwarf objects.
4. We provided empirical relationships between the ionized gas mass, neutral gas mass, dust mass, stellar mass, and dynamical mass with the B -luminosity. Although all mass estimations increase with increasing luminosity, we find important deviations to the general trend in some objects, which seem to be consequence of peculiarities in these galaxies. The comparison between the dynamical mass (derived from the kinematics of the neutral gas) with the Keplerian mass (obtained from the kinematics of the ionized gas) and the stellar mass (from the H -band luminosity) provides further clues about systems in which the dynamics seem to be highly perturbed. We remark the importance of this study, because it is not common to find in the literature a comprehensive and detailed analysis of a sample of galaxies for which the total (dynamical or stellar) mass, the reddening-corrected luminosity in optical and NIR filters, and the T_e -based oxygen abundance, have been derived in a coherent way.
5. We investigated some mass-metallicity relations and compared with previous results found in the literature. As pointed out by Kewley & Ellison (2008), the choice of the metallicity calibration has a strong effect in the derived $M - Z$ relation. The tightness of the $M_{\text{dyn}} - Z$ calibration indicates that the dark matter content also increases with metallicity. The scatter in the $M_{\text{stars}} - Z$ and $M_{\text{bar}} - Z$ relations are

consequence of both the nature (dwarf galaxies, TDG candidates, mergers) and the star-formation histories experienced in each galaxy.

6. We found that our sample galaxies agree well with the Schmidt-Kennicutt scaling law of star-formation derived by Kennicutt et al. (2007), which considers individual star-forming regions within $M 51$. Some important deviation are found in NGC 5253 and Mkn 1199, which are very HI-deficient, and in SBS 1319+579, where the star-formation activity seems to be suppressed.
7. The study of the mass-to-light ratios reinforces some of the results found in our analysis. We found that the neutral-gas-mass-to-luminosity ratio clearly decreases with increasing mass, as it seems to happen with the ionized-gas-mass-to-luminosity ratio. The ionizing-cluster-mass-to-luminosity ratio, however, seems to be constant with metallicity. The fact that we do not find any dwarf galaxy high M_{HI}/L_B ratio indicates that they have not experienced a lonely life. The analysis of the $M_{\text{gas}}/M_{\text{stars}}$ ratio suggests that this kind of galaxies have equal amount of neutral and stellar masses for metallicities $12+\log(\text{O}/\text{H}) \sim 8.2-8.3$. The stellar-mass-to-luminosity ratio clearly increases with the $B - R$ color.
8. We found that the reddening coefficient derived from the Balmer decrement clearly increases the warm dust mass, indicating that the extinction is mainly internal to the galaxy and not in the line-of-sight. We confirmed that the dust-to-gas ratio increases with the metallicity, and suggested that the low $M_{\text{dust}}/M_{\text{gas}}$ ratios in dwarf low-metallicity galaxies is a consequence of the large reserves of unenriched neutral gas. However, the low $M_{\text{dust}}/M_{\text{gas}}$ ratios observed at the outskirts of spiral galaxies seem to be a result of the decreasing star-formation efficiency in these regions.
9. The comparison of our data with the closed-box model clearly indicates that environment effects have played an important role in the evolution of the analyzed galaxies. The main effective yield we derived for our data agrees quite well with results found in the literature, in particular with results found in other starburst or irregular dwarf galaxies.

Considering all available data, we quantified how many galaxies are experiencing interaction or merger processes. We found that 17 up to 20 objects are clearly interacting or merging with low-luminosity dwarf objects or HI clouds, and all the remnant three galaxies (Mkn 5, SBS 1054+364, and SBS 1415+437) show considerable divergences of some properties when compared with similar objects. However, the interacting/merging features are only detected when deep optical spectroscopy and a detailed multiwavelength analysis (which includes a study of the kinematics and distribution of the neutral gas) are obtained. We therefore conclude that interactions do play a fundamental role in the triggering mechanism of the strong star-formation activity observed in dwarf starburst galaxies. This observational result completely agrees with the hierarchical model of galaxy formation that considers that large galactic structures were built up from the accretion of dwarf galaxies.

Acknowledgements. Based on observations made with NOT (Nordic Optical Telescope), INT (Isaac Newton Telescope), and WHT (William Herschel Telescope) operated on the island of La Palma jointly by Denmark, Finland, Iceland, Norway, and Sweden (NOT) or the Isaac Newton Group (INT, WHT) in the Spanish Observatorio del Roque de Los Muchachos of the Instituto de Astrofísica de Canarias. Based on observations made at the Centro Astronómico Hispano Alemán (CAHA) at Calar Alto, operated by the Max-Planck Institut für Astronomie and the Instituto de Astrofísica de Andalucía (CSIC). Based on

observations made with the ATCA (Australia Telescope Compact Array), which is funded by the Commonwealth of Australia for operation as a National Facility managed by CSIRO. Á.R. L-S thanks César Esteban (his formal Ph.D. supervisor) for all the help and very valuable explanations, talks, and discussions over these years. He also acknowledges Jorge García-Rojas, Sergio Simón-Díaz and José Caballero for their help and friendship during his Ph.D. studies, extending this acknowledgement to everyone at the Instituto de Astrofísica de Canarias (Spain). The author is indebted to the people at the CSIRO Astronomy and Space Science/Australia Telescope National Facility (ATNF), especially Bärbel Koribalski, for their support and friendship while translating his Ph.D. The author also thanks Bärbel Koribalski for her help analyzing HIPASS data and all the talks and discussions about radio-astronomy. The author is very grateful to A&A language editor, Joli Adams, for her kindly revision of the manuscript. Á.R. L.-S. deeply thanks the Universidad de La Laguna (Tenerife, Spain) for forcing him to translate his Ph.D. Thesis from English to Spanish; he had to translate it from Spanish to English for this publication. This was the main reason of the delay of the publication of this research, because the main results shown here were already included in the Ph.D. dissertation (in Spanish) which the author finished in 2006 (López-Sánchez 2006). This work was partially funded by the Spanish Ministerio de Ciencia y Tecnología (MCyT) under projects AYA2004-07466 and AYA2007-63030. This research made use of the NASA/IPAC Extragalactic Database (NED), which is operated by the Jet Propulsion Laboratory, California Institute of Technology, under contract with the National Aeronautics and Space Administration. The Galaxy Evolution Explorer (GALEX) is a NASA Small Explorer, launched in April 2003. We gratefully acknowledge NASA's support for construction, operation, and science analysis for the GALEX mission. The Infrared Astronomical Satellite (IRAS) mission was a collaborative effort by the United States (NASA), the Netherlands (NIVR), and the United Kingdom (SERC). This research has made extensive use of the SAO/NASA Astrophysics Data System Bibliographic Services (ADS).

Appendix A: Final summary of individual galaxies

In this Appendix we compile the main results found in our multiwavelength analysis of each individual system within our sample of WR galaxies. In Papers I we described the optical/*NIR* broad-band and $H\alpha$ photometry and in Paper II the intermediate-resolution optical spectroscopy analysis, of 16 up to 20 galaxies studied in this work. The analysis of the additional 4 systems were presented in previous papers: NGC 1741 (member AC within the HCG 31 group) in López-Sánchez et al. (2004a), Mkn 1087 and their surrounding galaxies in López-Sánchez et al. (2004b), the luminous blue compact galaxy IRAS 08339+6517 in López-Sánchez et al. (2006), and NGC 5253 in López-Sánchez et al. (2007). Paper III compiled the localization of the WR-rich star clusters within the galaxies and the analysis of their massive stellar populations. Paper IV compiles the global analysis of colors, and the physical properties and chemical abundances of the ionized gas. This paper, the last in the series, completes our multiwavelength analysis involving X-ray, UV, FIR, and radio data in both the 21-cm H I line and the 1.4 GHz radio-continuum.

- **NGC 1741** hosts a very strong star-formation event, which is very probably a consequence of the merging of two spiral galaxies. NGC 1741 is the main member (AC) of the galaxy group HCG 31, and it is interacting with other galaxies in the group, including Mkn 1090 (HCG 31 G). We detect both the blue and red WR bumps in its brightest region, as well as the nebular He II $\lambda 4686$ line. HCG 31 AC seems to have a slightly higher N/O ratio. Some dwarf objects (members E, F1, F2, and H) are tidal dwarf galaxy (TDG) candidates. See López-Sánchez et al. (2004a) for details.
- **Mkn 1087** is a LCBG in interaction with the nearby galaxy KPG 103a and with a dwarf surrounding galaxy (N companion). Deep optical images show long stellar tails connecting the main body of the galaxy with diffuse objects, some of

them hosting star-formation activity, and several TDG candidates. Although WR features were previously reported by other authors, we do not detect any. See López-Sánchez et al. (2004b) for details.

- **Haro 15** probably is a medium-size Sc spiral in interaction with two nearby dwarf objects. Knot A shows a very high star-formation activity and WR features; its disturbed kinematics suggests that it is experiencing a minor merger with Haro 15. Knot B is an independent object because of its morphology, decoupled kinematics and chemical abundances.
- **Mkn 1199** is a system composed by an Sb-Sc spiral and a dwarf galaxy, both in clear interaction, as they may be at the first stages of a minor merger. The interaction has triggered the star-formation activity in some areas of the main galaxy. Both the blue and red WR bumps are detected in the central region of Mkn 1199, which has solar metallicity. It seems that a substantial fraction of the H I gas has been expelled to the intergalactic medium because of its low M_{HI}/L_B ratio.
- **Mkn 5** is a BCDG with a strong star-forming burst located in the external part of the galaxy. The blue WR bump is detected in this starbursting region, which also possesses an important underlying old stellar component. We do not find any evidence of interaction, but the amount of H I gas of the galaxy is very low compared with what is expected for a BCDG. Furthermore, its dynamical mass is higher than expected for an dwarf galaxy with similar properties. Both results suggest that Mkn 5 has lost its neutral gas in some moment in its past and still has disturbed H I kinematics.
- **IRAS 08208+2816** is a luminous infrared galaxy (LIRG) showing two long tails with very high star-formation activity. The kinematics of the ionized gas clearly indicate merger features and two long tidal tails with TDG candidates. The chemical abundances of the brightest knots also seem to be different. We detect both the blue and red WR bumps in the central region, which possesses a high N/O ratio.
- **IRAS 08339+6517** is an LIRG and an LCBG in clear interaction with a nearby dwarf galaxy. The majority of the H I gas of the system has been expelled to the intergalactic medium because of this interaction (Cannon et al. 2004). Our deep optical images reveal a faint stellar plume coincident with the H I tail and a disturbed morphology in the outskirts of the galaxy. A particular bright knot may be a TDG candidate of the remnant of a previous minor merger. We detect weak WR features in its central burst and quantified the star-formation history of the galaxy (López-Sánchez et al. 2006).
- **POX 4** is a morphology-disturbed, low-metallicity BCDG showing strong star-forming bursts throughout the galaxy. It seems to be in interaction with a nearby dwarf object that may have passed through the main body of the galaxy, which is the origin of its ring-like morphology (Méndez & Esteban 1997) and kinematics. However, this object may also be a TDG candidate originated by the interaction with a nearby and diffuse H I cloud (López-Sánchez et al. 2010b). The He II $\lambda 4686$ emission line is clearly detected in its brightest region, as well as both the blue and the red WR bumps.
- **UM 420**: is a blue compact galaxy, but not a dwarf object, hosting intense star-formation activity. Besides it is located at 237 Mpc, we observe a central region and two kind of bright $H\alpha$ tails pointing towards different directions. Its kinematics is also perturbed. It has a very low metallicity for an object with its absolute optical/*NIR* luminosities, suggesting that it is a merging of two independent galaxies. We detect the He II $\lambda 4686$ emission line but not the blue WR bump in its brightest region. We found a probable N/O enrichment

- in the central region. Its colors and properties are somewhat contaminated by the spiral disk of the foreground galaxy UGC 1809, located at 97 Mpc.
- **SBS 0926+606**: is a galaxy pair with high star-formation activity. Member A is a BCDG that shows a double nucleus; both its morphology and kinematics strongly suggests that it is a galaxy merger. We do not detect any WR features in this galaxy but only the He II $\lambda 4686$ emission line. On the other hand, member B (another BCDG) hosts less star-formation activity, but it also shows hints of interactions, in particular a long diffuse optical tail that shows a TDG candidate. SBS 0926+606 B has a huge emission in *UV*; the SFR derived from the *FUV* luminosity is more than one order of magnitude higher than the H α -based SFR. The system still hosts a huge amount of neutral gas.
 - **SBS 0948+532**: is a very compact and blue object that hosts very high star-formation activity. Its M_{HII}/L_B ratio is very high in comparison with objects with similar properties. Although usually classified as BCDGs, its total *B*-luminosity indicates that it is not a dwarf object. We detect a faint optical tail mainly composed of old stars and with slightly disturbed kinematics. We observed the nebular and broad He II $\lambda 4686$ lines.
 - **SBS 1054+365**: is a very nearby BCDG showing several star-forming regions embedded in a elliptical envelope composed of old stars. The kinematics of the ionized gas seem to be slightly disturbed. The main starbursting region shows the nebular and broad He II $\lambda 4686$ lines. Although we do not detect any clear interaction feature, its dynamical mass is too high in comparison with that observed in similar objects, and its metallicity is too high for a dwarf object. Further studies are needed to clarify its nature.
 - **SBS 1211+540**: is a very low-metallicity BCDG. It is composed of two bright H α regions surrounded by a relatively old stellar component. This BCDG seems to show a higher metallicity than expected for a dwarf object with the same properties. The detection of two faint optical tails and its disturbed kinematics suggest that this galaxy is experiencing its first stages of a merger process. Although reported previously, we do not detect any WR features.
 - **SBS 1319+579**: is a cometary-like BCDG showing two chains of intense star-forming regions over an underlying low-luminosity component dominated by old stars. We detect a very faint blue WR feature in the brightest knot. The analysis of the kinematics of the ionized gas strongly suggests that it is composed of two objects in interaction, which it is happening edge-on. Although there is plenty of neutral gas, the star-formation is not very efficient, showing very low M_{HII}/L_B and M_{\star}/L_B ratios in comparison with similar objects. Furthermore, it does not satisfy the Schmidt-Kennicutt law of star-formation and the HI dynamics seem to be perturbed. We consider that the neutral gas has been expelled from the galaxy, but interferometric observations are needed to probe it.
 - **SBS 1415+437**: is a very low-metallicity BCDG that hosts a very strong star-forming region in which the nebular He II $\lambda 4686$ emission line is observed. It possesses a large old stellar population underlying the starburst. We do not detect any optical nearby companions, and it does not show any evidence of interactions.
 - **III Zw 107**: is a BCDG showing two strong star-forming bursts embedded in an irregular envelope. A diffuse prominent tail is detected in this object. The broad He II $\lambda 4686$ line is found in the brightest knot, which shows a slightly higher N/O ratio. The neutral gas may have been expelled and/or dispersed. This galaxy is likely composed of two dwarf objects in process of interaction or merging.
 - **Tol 9**: is a BCG that belongs to the Klemola 13 galaxy group. It is an elliptical-shaped galaxy with intense nebular emission and chemically evolved. We detected morphological and kinematical patterns that suggest interaction features. Our deep H α image reveals an extended filamentary structure with two main features that are located almost perpendicular to the main optical axis of the galaxy. The probable origin of this structure is a galactic wind. We detected both the blue and red WR bumps in the central region. The HI morphology and kinematics are quite intriguing, because this galaxy and two surrounding dwarf objects are embedded in the same HI cloud (López-Sánchez et al. 2008b, 2010b).
 - **Tol 1457-262**: is a system composed of two bright objects and two dwarf galaxies, all showing nebular emission. We detect the nebular He II line in the brightest knots of the main object. The regions within this system show chemical differences and peculiar kinematics. The neutral gas content seems to be very high, and its dynamics highly perturbed, although detailed HI map should be required to quantify this. We consider that this system is a galaxy group in which its members interact.
 - **Arp 252**: is a galaxy pair composed by two spiral galaxies, ESO 566-8 (A) and ESO 566-7 (B), in the first stages of a major merger. This object shows two long tails mainly composed by old stars but hosting some star-forming regions and TDG candidates. ESO 566-8 shows the broad and nebular He II $\lambda 4686$ emission line and the red WR bump. Its N/O is quite high for a galaxy with its oxygen abundance. ESO 566-8 has a strong star-formation and may host some kind of nuclear activity, because the FIR/radio relation is not satisfied in it. Although it was previously observed by other authors, we do not observe any WR feature in ESO 566-7.
 - **NGC 5253**: is a very nearby BCDG showing many peculiarities with respect to objects of similar characteristics. We detect clear broad WR features in the central regions, indicating the presence of both WNL and WCE stars. We confirmed a localized N enrichment in certain zones in the center of the galaxy and suggested a possible slight He overabundance in the same areas. We demonstrated that the enrichment pattern agrees with that expected for the pollution by the ejecta of WR stars. The amount of enriched material needed to produce the observed overabundance is consistent with the mass lost by the number of WR stars estimated in the starbursts (see López-Sánchez et al. 2007, for details). Although the kinematics of the ionized gas is somewhat peculiar, stellar kinematics seem to be the consequence of rotation. Our optical study has not revealed any disturbed feature of a recent interaction process. However, its HI morphology is disturbed and its kinematics are quite intriguing, because it does not show any sign of regular rotation. The origin of this anomaly is most likely the disruption/accretion of a dwarf gas-rich companion or the interaction with another galaxy in the M 83 subgroup (Kobulnicky & Skillman 2008; López-Sánchez et al. 2008a, 2010a). Furthermore, its M_{HI}/L_B and M_{dust}/L_B ratios are very low and it does not satisfy the Schmidt-Kennicutt law of star-formation.

References

- Allouin, D., Collin-Souffrin, S., Joly, M., & Vigroux, L. 1979, A&A, 78, 200
 Amorín, R. O., Muñoz-Tuñón, C., Aguerri, J. A. L., Cairós, L. M., & Caon, N. 2007, A&A, 467, 541

- Amorín, R., Aguerri, J. A. L., Muñoz-Tuñón, C., & Cairós, L. M. 2009, *A&A*, 501, 75
- Arp, H. C. 1966, *ApJS*, 14, 1
- Arribas, S., Bushouse, H., Lucas, R. A., Colina, L., & Borne, K. D. 2004, *AJ*, 127, 2522
- Barnes, D. G., Staveley-Smith, L., de Blok, W. J. G., et al. 2001, *MNRAS*, 322, 486
- Barone, L. T., Heithausen, A., Hüttemeister, S., Fritz, T., & Klein, U. 2002, *MNRAS*, 317, 649
- Barton, E. J., Geller, M. J., & Kenyon, S. J. 2000, *ApJ*, 530, 660
- Basu-Zych, A. R., Gonçalves, T. S., Overzier, R., et al. 2009, *ApJ*, 699, 118
- Begum, A., Chengalur, J. N., Karachentsev, I. D., Kaisin, S. S., & Sharina, M. E. 2006, *MNRAS*, 365, 1220
- Begum, A., Chengalur, J. N., Karachentsev, I. D., Sharina, M. E., & Kaisin, S. S. 2008, *MNRAS*, 386, 1667
- Bekki, K. 2008, *MNRAS*, 388, 10
- Bell, E. F. 2003, *ApJ*, 586, 794
- Bell, E. F., & de Jong, R. S. 2000, *MNRAS*, 312, 497
- Bergvall, N., & Östlin, G. 2002, *A&A*, 390, 891
- Bessell, M. S., Castelli, F., & Plez, B. 1998, *A&A*, 333, 231
- Bomans, D. J. 2005, proceedings of The Evolution of the Starburst: The 331st Wilhelm and Else Heraeus Seminar, AIPC, 783, 98
- Bomans, D. J., van Eymeren, J., Dettmar, R.-J., Weis, K., & Hopp, U. 2007, *NewAR*, 51, 141
- Boselli, A., Gavazzi, G., Donas, J., & Scodreggio, M. 2001, *AJ*, 121, 753
- Bothun, G. D., Romanishin, W., Strom, S. E., & Strom, K. M. 1984, *AJ*, 89, 1300
- Braine, J., Lisenfeld, U., Due, P.-A., & Leon, S. 2000, *Nature*, 403, 867
- Braine, J., Duc, P.-A., Lisenfeld, U., et al. 2001, *A&A*, 378, 51
- Braine, J., Duc, P.-A., Lisenfeld, U., et al. 2004, in *Recycling Intergalactic and Interstellar Matter*, ed. P. A. Duc, J. Braine, & E. Brinks, IAU Symp., 217, 518
- Bravo-Alfaro, H., Brinks, E., Baker, A. J., Walter, F., & Kunth, D. 2004, *AJ*, 127, 264
- Bravo-Alfaro, H., Coziol, R., & Brinks, E. 2006, *RevMexAA*, 42, 261
- Brinchmann, J., Kunth, D., & Durret, F. 2008, *A&A*, 485, 657
- Broeils, A. H., & van Woerden, H. 1994, *A&AS*, 107, 129
- Bruzual, G., & Charlot, S. 2003, *MNRAS*, 344, 1000, BC03
- Cairós, L. M., Vílchez, J. M., González Pérez, J. N., Iglesias-Páramo, J., & Caon, N. 2001a, *ApJS*, 133, 321
- Cairós, L. M., Caon, N., Vílchez, J. M., González-Pérez, J. N. & Muñoz-Tuñón, C. 2001b, *ApJS*, 136, 393
- Cairós, L. M., Caon, N., Zurita, C., et al. 2009, *A&A*, 507, 1291
- Calura, F., Matteucci, F. & Menci, N. 2004, *MNRAS*, 353, 500
- Calzetti, D. 2001, *PASP*, 113, 1149
- Calzetti, D., Kennicutt, R. C., Engelbracht, C. W., et al. 2007, *ApJ*, 666, 870
- Campos-Aguilar, A., Moles, M., & Masegosa, J. 1993, *AJ*, 106, 1784
- Cannon, J. M., Skillman, E. D., Kunth, D., et al. 2004, *ApJ*, 608, 768
- Cardamone, C., Schawinski, K., Sarzi, M., et al. 2009, *MNRAS*, 399, 1191
- Cardelli, J. A., Clayton, G. C., & Mathis, J. S. 1989, *ApJ*, 345, 245
- Casasola, V., Bettoni, D., & Galletta, G. 2004, *A&A*, 422, 941
- Clayton, D. D., & Pantelaki, I. 1993, *PhR*, 227, 293
- Colina, L., Bohlin, R. C., & Castelli, F. 1996, *AJ*, 112, 307
- Colina, L., Arribas, S., & Monreal-Ibero, A. 2005, *ApJ*, 621, 725
- Condon, J. J. 1992, *ARA&A*, 30, 575
- Condon, J. J., Helou, G., Sanders, D. B., & Soifer, B. T. 1990, *ApJS*, 73, 359
- Condon, J. J., Anderson, M. L., & Helou, G. 1991, *ApJ*, 376, 95
- Condon, J. J., Cotton, W. D., Greisen, E. W., et al. 1998, *AJ*, 115, 1693
- Condon, J. J., Cotton, W. D., & Broderick, J. J. 2002, *AJ*, 124, 675
- Crowther, P. A. 2007, *ARA&A*, 45, 177
- Crowther, P. A., & Hadfield, L. J. 2006, *A&A*, 449, 711
- Cumming, R. J., Fathi, K., Östlin, G., et al. 2008, *A&A*, 479, 725
- Davé, R., & Oppenheimer, B. D. 2007, *MNRAS*, 374, 427
- Davies, J. I., & Phillipps, S. 1988, *MNRAS*, 233, 553
- Davoust, E., & Contini, T. 2004, *A&A*, 416, 515
- de Blok, W. J. G., Walter, F., Brinks, E., et al. 2008, *AJ*, 136, 2648
- de Jong, R. S. 1996, *A&A*, 313, 377
- De Lucia, G., Kauffmann, G., & White, S. D. M. 2004, *MNRAS*, 374, 323
- Denicoló, G., Terlevich, R., & Terlevich, E. 2002, *MNRAS*, 330, 69
- de Naray, R. K., McGaugh, S. S., & de Blok, W. J. G. 2004, *MNRAS*, 355, 887
- De Rossi, M. E., Tissera, P. B., & Scannapieco, C. 2006, *MNRAS*, 374, 323
- Díaz, A. I., & Pérez-Montero, E. 2000, *MNRAS*, 312, 130
- Dopita, M. A., & Evans, I. N. 1986, *ApJ*, 307, 431
- Dopita, M. A., Kewley, L. J., Heisler, C. A., & Sutherland, R. S. 2000, *ApJ*, 542, 224
- Dopita, M. A., Pereira, M., Kewley, L. J., & Capaccioli, M. 2002, *ApJS*, 143, 47
- Draine, B. T., Dale, D. A., Bendo, G., et al. 2007, *ApJ*, 663, 866
- Dubois, Y., & Teyssier, R. 2007, *EAS*, 24, 95
- Duc, P.-A., & Mirabel, I. F. 1998, *A&A*, 338, 813
- Duc, P. A., Brinks, E., Springel, V., et al. 2000, *AJ*, 120, 1238
- Edmunds, M. G. 1990, *MNRAS*, 246, 678
- Edmunds, M. G., & Pagel, B. E. J. 1978, *MNRAS*, 185, 77
- Edmunds, M. G., & Pagel, B. E. J. 1984, *MNRAS*, 211, 507
- Ekta, C. J. N., & Pustilnik, S. A. 2006, *MNRAS*, 372, 853
- Ekta, C. J. N., & Pustilnik, S. A. 2008, *MNRAS*, 391, 881
- Emonts, B. H. C., Morganti, R., Oosterloo, T. A., et al. 2006, *AN*, 327, 139
- English, J., Koribalski, B. S., Bland-Hawthorn, J., Freeman, K. C., & McCain, C. F. 2010, *AJ*, 139, 102
- Erb, D. K., Shapley, A. E., Steidel, C. C., et al. 2003, *ApJ*, 591, 101
- Erb, D. K., Shapley, A. E., Pettini, M., et al. 2006, *ApJ*, 644, 813
- Esteban, C., & Peimbert, M. 1995, *A&A*, 300, 78
- Esteban, C., Bresolin, F., Peimbert, M., et al. 2009, *ApJ*, 700, 654
- Fabbiano, G., Feigelson, E., & Zamorani, G. 1982, *ApJ*, 256, 397
- Ferland, G. J., Korista, K. T., Verner, D. A., et al. 1998, *PASP*, 110, 761
- Fioc, M., & Rocca-Volmerange, B. 1997, *A&A*, 326, 950
- Gallagher, J. S. III, Hunter, D. A., & Tutukov, A. V. 1984, *ApJ*, 284, 544
- García-Lorenzo, B., Cairós, L. M., Caon, N., Monreal-Ibero, A., & Kehrig, C. 2008, *ApJ*, 677, 201
- García-Rojas, J., & Esteban, C. 2007, *ApJ*, 670, 457
- Garnett, D. R. 1992, *AJ*, 103, 1330
- Garnett, D. R. 2002, *ApJ*, 581, 1019
- Genzel, R., Lutz, D., Sturm, E., et al. 1998, *ApJ*, 498, 579
- Gerola, H., Seiden, P. E., & Schulman, L. S. 1980, *ApJ*, 242, 517
- Giovanelli, R., Haynes, M. P., Kent, B. R., et al. 2005, *AJ*, 130, 2598
- Gil de Paz, A., Madore, B. F., & Pevunova, O. 2003, *ApJS*, 147, 29
- Gil de Paz, A., Madore, B. F., Boissier, S., et al. 2005, *ApJ*, 627, 29
- Gil de Paz, A., Madore, B. F., Boissier, S., et al. 2007, *ApJ*, 661, 115
- Gordon, D., & Gottesman, S. T. 1981, *AJ*, 86, 161
- Guzman, R., Gallego, J., Koo, D. C., et al. 1997, *ApJ*, 489, 559
- Hägele, G. F., Díez, Á. I., Terlevich, E., et al. 2008, *MNRAS*, 383, 209
- Heckam, T. M. 1999, *Ap&SS*, 266, 3
- Henry, R. B. C., Edmunds, M. G., & Köppen, J. 2000, *ApJ*, 541, 660
- Hidalgo-Gómez, A. M., & Olofsson, K. 1998, *A&A*, 334, 45
- Hibbard, J. E., & van Gorkom, J. H. 1996, *AJ*, 111, 655
- Hibbard, J. E., van Gorkom, J. H., Rupen, M. P., & Schiminovich, D. 2001b, *An HI Rogues Gallery, Gas and Galaxy Evolution, ASP Conf. Ser.*, 240, 657
- Hirashita, H. 2000, *PASJ*, 52, 107
- Hirashita, H., Inoue, A. K., Kamaya, H., & Shibai, H. 2001, *A&A*, 366, 83
- Hopkins, A. M., Schulte-Ladbeck, R. E., & Drozdovsky, I. O. 2002, *AJ*, 124, 862
- Huchtmeier, W. K., Sage, L. J., & Henkel, C. 1995, *A&A*, 300, 675
- Huchtmeier, W. K., Krishna, G., & Petrosian, A. 2005, *A&A*, 434, 887
- Huchtmeier, W. K., Petrosian, A., Krishna, G., & Kunth, D. 2007, *A&A*, 462, 919
- Huchtmeier, W. K., Petrosian, A., Krishna, G., McLean, B., & Kunth, D. 2008, *A&A*, 492, 367
- Izotov, Y. I., & Thuan, T. X. 1998, *ApJ*, 500, 188
- Izotov, Y. I., & Thuan, T. X. 1999, *ApJ*, 511, 639
- Izotov, Y. I., & Thuan, T. X. 2004, *ApJ*, 616, 768
- Izotov, Y. I., Papaderos, P., Guseva, N. G., Fricke, K. J., & Thuan, T. X. 2004, *A&A*, 421, 539
- Izotov, Y. I., Stasińska, G., Meynet, G., Guseva, N. G., & Thuan, T. X. 2006, *A&A*, 448, 955
- James, A., Dunne, L., Eales, S., & Edmunds, M. G. 2002, *MNRAS*, 335, 753
- James, P. A., Shane, N. S., Knapen, J. H., Etherton, J., & Percival, S. M. 2005, *A&A*, 429, 851
- James, B. L., Tsamis, Y. G., Barlow, M. J., et al. 2009, *MNRAS*, 398, 2
- James, B. L., Tsamis, Y. G., & Barlow, M. J. 2010, *MNRAS*, 401, 759
- Jansen, R. A., Franx, M., Fabricant, D., & Caldwell, N. 2000, *ApJS*, 126, 271
- Jensen, E. B., Strom, K. M., & Strom, S. E. 1976, *ApJ*, 209, 748
- Johnson, K. E., & Kobulnicky, H. A. 2003, *ApJ*, 597, 923
- Johnson, K. E., Indebetouw, R., Watson, C., & Kobulnicky, H. A. 2004, *AJ*, 128, 610
- Joseph, R. D., & Wright, G. S. 1985, *MNRAS*, 214, 87
- Karachentsev, I. D., Karachentseva, V. E., Huchtmeier, W. K., & Makarov, D. I. 2004, *AJ*, 127, 2031
- Kauffmann, G., & White, S. D. M. 1993, *MNRAS*, 261, 921
- Kaufman, M., Brinks, E., Elmegreen, D. M., et al. 1997, *AJ*, 114, 2323
- Kauffmann, G., Heckman, T. M., Tremonti, C., et al. 2003, *MNRAS*, 346, 1055
- Kay, S. T., Pearce, F. R., Frenk, C. S., & Jenkins, A. 2002, *MNRAS*, 330, 113
- Kennicutt, R. C. Jr. 1998, *ApJ*, 498, 541
- Kennicutt, R. C. Jr., Bresolin, F., & Garnett, D. R. 2003, *ApJ*, 591, 801
- Kennicutt, R. C. Jr., Calzetti, D., Walter, F., et al. 2007, *ApJ*, 671, 333
- Kewley, L. J., & Dopita, M. A. 2002, *ApJS*, 142, 35
- Kewley, L. J., & Ellison, S. E. 2008, *ApJ*, 681, 1183
- Kewley, L. J., Dopita, M. A., Sutherland, R. S., Heisler, C. A., & Trevena, J. 2001, *ApJS*, 556, 121

- Kinman, T. D., & Davidson, K. 1981, *ApJ*, 243, 127
- Kirby, E. M., Jerjen, H., Ryder, S. D., & Driver, S. P. 2008, *AJ*, 136, 1866
- Kobulnicky, H. A., & Skillman, E. D. 1998, *ApJ*, 497, 601
- Kobulnicky, H. A., & Johnson, K. E. 1999, *ApJ*, 627, 154
- Kobulnicky, H. A., & Kewley, L. J. 2004, *ApJ*, 617, 240
- Kobulnicky, H. A., & Skillman, E. D. 2008, *AJ*, 135, 527
- Kobulnicky, H. A., Skillman, E. D., Roy, J.-R., Walsh, J. R., & Rosa, M. R. 1997, *ApJ*, 277, 679
- Kobulnicky, H. A., Kennicutt, R. C. Jr., & Pizagno, J. L. 1999, *ApJ*, 514, 544
- Kobulnicky, H. A., Willmer, C. N. A., Phillips, A. C., et al. 2003, *ApJ*, 599, 1006
- Koribalski, B. 1996, *ASPC*, 106, 238
- Koribalski, B., & Dickey, J. M. 2004, *MNRAS*, 348, 1255
- Koribalski, B., & Manthey, E. 2005, *MNRAS*, 358, 202
- Koribalski, B. S., & López-Sánchez, Á. R. 2009, *MNRAS*, 400, 1749
- Koribalski, B., Gordon, S., & Jones, K. 2003, *MNRAS*, 339, 1203
- Koribalski, B. S., Staveley-Smith, L., Kilborn, V. A., et al. 2004, *AJ*, 128, 16
- Lambas, D. G., Tissera, P. B., Alonso, M. S., & Coldwell, G. 2003, *MNRAS*, 346, 1189
- Larson, R. B., & Tinsley, B. M. 1978, *ApJ*, 219, 46
- Lee, H., McCall, M. L., Kingsburgh, R. L., Ross, R., & Stevenson, C. C. 2003, *AJ*, 125, 146
- Lee, J. C., Salzer, J. J., & Melbourne, J. 2004, *ApJ*, 616, 752L
- Lee, H., Zucker, D. B., & Grebel, E. K. 2007, *MNRAS*, 376, 820
- Lee, J. C., Gil de Paz, A., Tremonti, C., et al. 2009, *ApJ*, 706, 599
- Leitherer, C., Schaerer, D., Goldader, J. D., et al. 1999, *ApJS*, 123, 3, STARBURST 99
- Lequeux, J., Peimbert, M., Rayo, J. F., Serrano, A., & Torres-Peimbert, S. 1979, *A&A*, 80, 155
- Leroy, A. K., Walter, F., Brinks, E., et al. 2008, *AJ*, 136, 2782
- Liang, Y. C., Yin, S. Y., Hammer, F., et al. 2006, *ApJ*, 652, 257
- Lilly, S. J., Carollo, C. M., & Stockton, A. N. 2003, *ApJ*, 597, 730
- Lisenfeld, U., & Ferrara, A. 1998, *ApJ*, 496, 145
- Lonsdale, C. J., Persson, S. E., & Matthews, K. 1984, *ApJ*, 287, 95
- López-Sánchez, Á. R. 2006, Ph.D. Thesis, Universidad de la Laguna, Tenerife, Spain
- López-Sánchez, Á. R., & Esteban, C. 2008, *A&A*, 491, 131, Paper I
- López-Sánchez, Á. R., & Esteban, C. 2009, *A&A*, 508, 615, Paper II
- López-Sánchez, Á. R., & Esteban, C. 2010a, *A&A*, 516, 104, Paper III
- López-Sánchez, Á. R., & Esteban, C. 2010b, *A&A*, 517, A85, Paper IV
- López-Sánchez, Á. R., Esteban, C., & Rodríguez, M. 2004a, *ApJS*, 153, 243
- López-Sánchez, Á. R., Esteban, C., & Rodríguez, M. 2004b, *A&A*, 428, 445
- López-Sánchez, Á. R., Esteban, C., & García-Rojas, J. 2006, *A&A*, 449, 997
- López-Sánchez, Á. R., Esteban, C., García-Rojas, J., Peimbert, M., & Rodríguez, M. 2007, *ApJ*, 656, 168
- López-Sánchez, Á. R., Koribalski, B., & Esteban, C. 2008a, *proc. of Galaxies in the Local Volume* (Springer), 53
- López-Sánchez, Á. R., Koribalski, B., Esteban, C., & Hibbard, J. 2008b, *proc. of Galaxies in the Local Volume* (Springer), 301
- López-Sánchez, Á. R., Koribalski, B. S., van Eymeren, J., et al. 2010a, *MNRAS*, in prep., NGC 5253
- López-Sánchez, Á. R., Koribalski, B. S., Esteban, C., et al. 2010b, *MNRAS*, in prep., Tol 9
- Lou, Y.-Q., & Bian, F.-Y. 2005, *MNRAS*, 358, 1231
- Mac Low, M.-M., & Ferrara, A. 1999, *ApJ*, 513, 142
- Marlowe, A. T., Heckman, T. M., Wyse, R. F. G., & Schommer, R. 1995, *ApJ*, 438, 563
- Mathewson, D. S., Ford, V. L., & Buchhorn, M. 1992, *ApJS*, 81, 413
- McCall, M. L., Rybski, P. M., & Shields, G. A. 1985, *ApJS*, 57, 1
- McGaugh, S. S. 1991, *ApJ*, 380, 140
- McGaugh, S. S. 1994, *ApJ*, 426, 135
- McGaugh, S. S., & de Blok, W. J. G. 1997, *ApJ*, 481, 689
- Mendes de Oliveira, C. L., Temporin, S., Cypriano, E. S., et al. 2006, *AJ*, 132, 570
- Méndez, D. I., & Esteban, C. 1997, *ApJ*, 488, 652
- Méndez, D. I., & Esteban, C. 1999, *AJ*, 118, 2733
- Méndez, D. I., & Esteban, C. 2000, *A&A*, 359, 493
- Meyer, M. J., Zwaan, M. A., Webster, R. L., et al. 2004, *MNRAS*, 350, 1195
- Meynet, G., & Maeder, A. 2002, *A&A*, 390, 561
- Meynet G., & Maeder A. 2005, *A&A*, 429, 581
- Morrissey, P., & GALEX Science Team 2005, *BAAS*, 37, 1454
- Muñoz-Mateos, J. C., Gil de Paz, A., Zamorano, J., et al. 2009, *ApJ*, 703, 1569
- Nagao, T., Maiolino, R., & Marconi, A. 2006, *A&A*, 459, 85
- Niklas, S., Klein, U., & Wielebinski, R. 1997, *A&A*, 322, 19
- Nikolic, B., Cullen, H., & Alexander, P. 2004, *MNRAS*, 355, 874
- Noeske, K. G., Iglesias-Páramo, J., Vílchez, J. M., Papaderos, P., & Fricke, K. J. 2001, *A&A*, 371, 806
- Noeske, K. G., Papaderos, P., Cairós, L. M., & Fricke, K. J. 2003, *A&A*, 410, 481
- Noeske, K. G., Papaderos, P., Cairós, L. M., & Fricke, K. J. 2005, *A&A*, 429, 115
- Oey, M. S., & Shields, J. C. 2000, *ApJ*, 539, 687
- Östlin, G., Amram, P., Bergvall, N., et al. 2001, *A&A*, 374, 800
- Östlin, G., Cumming, R. J., Amram, P., et al. 2004, *A&A*, 419, 43
- Overzier, R. A., Abbott, R., Adhikari, R., et al. 2009, *ApJ*, 706, 203
- Pagel, B. E. J., Edmunds, M. G., Blackwell, D. E., Chun, M. S., & Smith, G. 1979, *MNRAS*, 189, 95
- Papaderos, P., Guseva, N. G., Izotov, Y. I., et al. 2006, *A&A*, 457, 45
- Paturel, G., Theureau, G., Bottinelli, L., et al. 2003, *A&A*, 412, 57
- Peimbert, M. 1967, *ApJ*, 150, 825
- Peimbert, M., Peimbert, A., Esteban, C., et al. 2007, *RMxAC*, 29, 72
- Peña, M., & Ayala, S. 1993, *RevMexAA*, 27, 171
- Pérez-Montero, E., & Díaz, A. I. 2005, *MNRAS*, 361, 1063
- Pettini, M., & Pagel, B. E. J. 2004, *MNRAS*, 348, 59
- Pettini, M., Shapley, A. E., Steidel, C. C., et al. 2001, *ApJ*, 554, 981
- Pflamm-Altenburg, J., Weidner, C., & Kroupa, P. 2009, *MNRAS*, 395, 394
- Pilyugin, L. S. 2000, *A&A*, 362, 325
- Pilyugin, L. S. 2001a, *A&A*, 369, 594
- Pilyugin, L. S. 2001b, *A&A*, 374, 412
- Pilyugin, L. S., & Thuan, T. X. 2005, *ApJ*, 631, 231
- Pilyugin, L. S., Thuan, T. X., & Vílchez, J. M. 2003, *A&A*, 397, 487
- Pilyugin, L. S., Vílchez, J. M., & Contini, T. 2004, *A&A*, 425, 849
- Piovan, L., Tantaló, R., & Chiosi, C. 2006, *MNRAS*, 366, 923
- Pustilnik, S. A., Kniazev, A. Y., Lipovetsky, V. A., & Ugrumov, A. V. 2001, *A&A*, 373, 24
- Pustilnik, S. A., Martin, J.-M., Huchtmeier, W. K., et al. 2002, *A&A*, 389, 405
- Pustilnik, S., Kniazev, A., Pramskij, A., et al. 2004, *A&A*, 419, 469
- Putman, M. E., Staveley-Smith, L., Freeman, K. C., Gibson, B. K., & Barnes, D. G. 2003, *ApJ*, 586, 170
- Ranalli, P., Comastri, A., & Setti, G. 2003, *A&A*, 399, 39
- Richer, M. G., & McCall, M. L. 1995, *ApJ*, 445, 642
- Robert, M. S. 1975, in *Galaxies and the Universe*, with an index prepared by Gustav A. Tammann, Published by the University of Chicago Press, ed. A. Sandage, M. Sandage, & J. Kristian (Chicago: IL USA), Stars and Stellar Systems, 9, 309
- Roberts, M. S., & Haynes, M. P. 1994, *ARA&A*, 32, 115
- Roussel, H., Sauvage, M., Vigroux, L., & Bosma, A. 2001, *A&A*, 372, 427
- Rubin, V. C., Ford, W. K., Jr., & Whitmore, B. C. 1984, *ApJ*, 281, L21
- Salim, S., Rich, R. M., Charlot, S., et al. 2007, *ApJS*, 173, 267
- Salpeter, E. E., & Hoffman, G. L. 1996, *ApJ*, 465, 595
- Salzer, J. J., Rosenberg, J. L., Weisstein, E. W., Mazzarella, J. M., & Bothun, G. D. 2002, *AJ*, 124, 191
- Salzer, J. J., Lee, J. C., Melbourne, J., et al. 2005, *ApJ*, 624, 661
- Sanders, D. B. 1997, *RMxAC*, 6, 42
- Sanders, D. B., & Mirabel, I. F. 1996, *ARA&A*, 34, 749
- Sargent, W. L. W., & Searle, L. 1970, *ApJ*, 162, L155
- Schaerer, D., & Vacca, W. D. 1998, *ApJ*, 497, 618 (SV98)
- Schaerer, D., Contini, T., & Pindao, M. 1999, *A&AS*, 136, 35
- Schmidt, M. 1959, *ApJ*, 129, 243
- Schmidt, M. 1963, *ApJ*, 137, 758
- Searle, L., & Sargent, W. L. W. 1972, *ApJ*, 173, 25
- Silich, S. A., & Tenorio-Tagle, G. 1998, *MNRAS*, 299, 249
- Skillman, E. D., Kennicutt, R. C., & Hodge, P. W. 1989, *ApJ*, 347, 875
- Skillman, E. D., Côté, S., & Miller, B. W. 2003, *AJ*, 125, 593
- Solomon, P. M., & Sage, L. J. 1988, *ApJ*, 334, 613
- Somerville, R. S., & Primack, J. R. 1999, *MNRAS*, 310, 1087
- Schneider, S. E. 1989, *ApJ*, 343, 94
- Springel, V., & Hernquist, L. 2003, *MNRAS*, 339, 312
- Springel, V., White, S. D. M., Jenkins, A., et al. 2005, *Nature*, 435, 629
- Stasińska, G. 2002, *RMxAC*, 12, 62
- Stasińska, G. 2005, *A&A*, 434, 507
- Stasińska, G. 2006, *A&A*, 454, 127
- Stasińska, G. 2009, *Stellar Populations - planning for the next decade*, ed. Bruzual & Charlot, *proc. IAU symp.*, 262 [arXiv:astro-ph/0910.0175]
- Stasińska, G., Schaerer, D., & Leitherer, C. 2001, *A&A*, 370, 1
- Steidel, C. C., Shapley, A. E., Pettini, M., et al. 2004, *ApJ*, 604, 534
- Stevens, I. R., & Strickland, D. K. 1998a, *MNRAS*, 294, 523
- Stevens, I. R., & Strickland, D. K. 1998b, *MNRAS*, 301, 215
- Storchi-Bergmann, T., Calzetti, D., & Kinney, A. L. 1994, *ApJ*, 429, 572
- Sutherland, R. S., & Dopita, M. A. 1993, *ApJS*, 88, 253
- Taylor, C. L., Brinks, E., & Skillman, E. D. 1993, *AJ*, 105, 128
- Taylor, C., Brinks, E., Grashuis, R. M., & Skillman, E. D. 1995, *ApJS*, 99, 427
- Taylor, C., Thomas, D., Brinks, E., & Skillman, E. D. 1996, *ApJS*, 107, 143
- Taylor, C. L., Kobulnicky, H. A., & Skillman, E. D. 1998, *AJ*, 116, 2746
- Telles, E., & Terlevich, R. J. 1995, *MNRAS*, 275, 1
- Telles, E., & Maddox, S. 2000, *MNRAS*, 311, 307

- Temporin, S., Weinberg, R., Galaz, G., & Kerber, F. 2003, *ApJ*, 587, 660
- Temporin, S., Staveley-Smith, L., & Florian, K. 2005, *MNRAS*, 356, 343
- Tenorio-Tagle, G., Muñoz-Tuñón, C., Pérez, E., Silich, S., & Telles, E. 2006, *ApJ*, 643, 186
- Teplitz, H. I., Malkan, M. A., Steidel, C. C., et al. 2000, *ApJ*, 542, 18
- Thilker, D. A., Bianchi, L., Boissier, S., et al. 2005, *ApJ*, 619, L79
- Thilker, D. A., Bianchi, L., Meurer, G., et al. 2007, *ApJS*, 173, 538
- Thuan, T. X. 1991, in *Massive stars in starbursts*, ed. C. Leitherer, N. R. Walborn, T. M. Heckman, & C. A. Norman (Cambridge: Cambridge University Press), 183
- Thuan, T. X., Lipovetski, V. A., Martin, J.-M., & Pustilnik, S. A. 1999, *A&ASS*, 139, 1
- Tissera, P. B., De Rossi, M. E., & Scannapieco, C. 2005, *MNRAS*, 364, L38
- Torres-Peimbert, S., Peimbert, M., & Fierro, J. 1989, *ApJ*, 345, 186
- Tremonti, C. A., Heckman, T. M., Kauffmann, G., et al. 2004, *ApJ*, 613, 898
- van Eymeren, J., Bomans, D. J., Weis, K., & Dettmar, R.-J. 2007, *A&A*, 474, 67
- van Eymeren, J., Marcelin, M., Koribalski, B. S., et al. 2009, *A&A*, 505, 105
- van Eymeren, J., Koribalski, B. S., López-Sánchez, Á. R., Dettmar, R.-J. & Bomans, D. J. 2010, *A&A*, submitted
- van Zee, L., & Haynes, M. P. 2006, *ApJ*, 636, 214
- van Zee, L., Salzer, J. J., & Haynes, M. P. 1998, *ApJ*, 497, 1
- van Zee, L., Salzer, J. J., & Skillman, E. D. 2001, *AJ*, 122, 121
- Vázquez, G. A., & Leitherer, C. 2005, *ApJ*, 621, 695
- Verma, A., Lutz, D., Sturm, E., et al. 2003, *A&A*, 403, 829
- Verdes-Montenegro, L., Yun, M. S., Williams, B. A., et al. 2001, *A&A*, 377, 812
- Verdes-Montenegro, L., del Olmo, A., Iglesias-Páramo, J. I., et al. 2002, *A&A*, 396, 815
- Verdes-Montenegro, L., del Olmo, A., Yun, M. S., & Perea, J. 2005, *A&A*, 430, 443
- Vila-Costas, M. B., & Edmunds, M. G. 1993, *MNRAS*, 259, 121
- Vila-Costas, M. B., & Edmunds, M. G. 1993, *MNRAS*, 265, 199
- Vílchez, J. M., & Esteban, C. 1996, *MNRAS*, 280, 720
- Walter, F., Brinks, E., de Blok, W. J. G., et al. 2008, *AJ*, 136, 2563
- Warren, B. E., Jerjen, H., & Koribalski, B. S. 2004, *AJ*, 128, 1152
- Warren, B. E., Jerjen, H., & Koribalski, B. S. 2006, *AJ*, 131, 2056
- Warren, B. E., Jerjen, H., & Koribalski, B. S. 2007, *AJ*, 134, 1849
- Weilbacher, P. M., Duc, P. A., & Fritze-von Alvensleben, U. 2003, *A&A*, 397, 545
- Werk, J. K., Jangren, A., & Salzer, J. J. 2004, *ApJ*, 617, 1004
- Westmeier, T., Braun, R., & Koribalski, B. S. 2010, *MNRAS*, accepted, [1009.0317]
- White, S. D. M., & Frenk, C. S. 1991, *ApJ*, 379, 52
- Wilcots, E. M., Lehman, C., & Miller, B. 1996, *AJ*, 111, 1575
- Wilson, C. D. 1995, *ApJ*, 448, 97
- Woosley, S. E., & Weaver, T. A. 1995, *ApJS*, 101, 181
- Wyse, R. F. G., & Silk, J. 1985, *ApJ*, 296, L1
- Yin, S. Y., Liang, Y. C., Hammer, F., et al. 2007, *A&A*, 462, 535
- Yun, M. S., Ho, P. T. P., & Lo, K. Y. 1994, *Nature*, 372, 530
- Yun, M. S., Reddy, N. A., & Condon, J. J. 2001, *ApJ*, 554, 803
- York, D. G., Adelman, J., Anderson, J. E., Jr., et al. 2000, *AJ*, 120, 1579
- Zaritsky, D., Kennicutt, R. C. Jr., & Huchra, J. P. 1994, *ApJ*, 420, 87
- Zasov, A. V., Kniazev, A. Y., Pustilnik, S. A., et al. 2000, *A&AS*, 144, 429